PEOPLE'S DEMOCRATIC REPUBLIC OF ALGERIA

MINISTRY OF HIGHER EDUCATION AND SCIENTIFIC RESEARCH

UNIVERSITY OF IBN-KHALDOUN TIARET

FACULTY OF APPLIED SCIENCES

ELECTRICAL ENGINEERING DEPARTMENT

Thesis

To obtain the degree of doctor

Domain: Science and Technology

Field: Electrical Engineering

Specialty: Electrical network

THEME

Investigation of the impact of various parameters on the morphology of thin films produced by the sputtering process

Presented by:

Refas Salah Eddine Chouaib

Board of Examiners:

Full name	Grade	Quality	domiciliation
SMAILI Attalah	Professor	President	U-Tiaret
YANNALAH Khelifa	Professor	Reviewer	U-Tiaret
SAHLI Belkacem	Professor	Reviewer	U-Tiaret
BOUDIAF mohamed	MCA	Reviewer	U-Djelfa
MERZOUK Imad	MCA	Reviewer	U-Djelfa
BOUAZZA Abdelkader	MCA	Supervisor	U-Tiaret

Academic Year: 2022/2023

ACKNOWLEDGEMENTS

I would like to express my deepest appreciation to my supervisor Mr. BOUAZZA AbdelKader who made every attempt to mentor and inspire me to perform at my best during my research.

Additionally, I want to express my gratitude to Professor SMAILI Attalah for granting me the privilege of accepting the jury's presidency.

My appreciation also extends to Professors YANNALAH Khelifa, SAHLI Belgacem, BOUDIAF Mohamed, and MERZOUK Imad for the attention they have shown towards my modest work that they agreed to evaluate.

Finally, I want to express my gratitude to everyone who contributed to making this work possible.

Dedication

This thesis is fully dedicated to: Allah, our Creator and Master.

To my beloved parents and brothers, who have inspired me, and assisted me in achieving my current position. They also continuously offer their moral, spiritual, emotional, and financial support.

To my teachers, and classmates who offered words of wisdom and motivation to complete this study.

Table of contents

Table of contents 1
List of Figures 4
List of Tables 8
Abbreviation list 9
General introduction 12

Chapter 1: Thin film deposition techniques

1.1 Introduction 16
1.2 General methods of thin film deposition 16
1.3 Chemical vapor deposition (CVD) 17
1.4 Physical Vapor Deposition (PVD) 18
1.4.1 The evaporation process 18
1.4.2 Laser ablation 19
1.4.3 Molecular beam epitaxy (MBE) 21
1.4.4 The Sputtering process 22
1.4.4.1 History 22
1.4.4.2 General principle 22
1.4.4.3 Experimental device for the sputtering process 23
1.5 Sputtering Methods 23
1.5.1 Diode sputtering in direct current 23
1.5.2 Glow discharge 24
1.5.3 Geometry of electrodes 26
1.5.4 The limits of the "diode" device 26
1.5.5 High frequency sputtering 26
1.5.6 Triode sputtering 27
1.5.7 Magnetron sputtering 29
1.5.8 Reactive sputtering 30
1.6 Growth of a thin layer 30
1.7 Conclusion 33

Chapter 2: Plasma and magnetron sputtering

2.1 Introduction 35
2.2 Plasma properties 35
2.2.1 Plasma 35
2.2.2 Cold Plasma 35
2.3 Characteristics 36
2.3.1 Density 36
2.3.2 Temperature 37
2.3.3 Ionization 37

2.3.4 Collisions 37
2.3.5 The free path 38
2.4 The collisional process 38
2.5 Emission of secondary electrons 39
2.6 Sheath 40
2.7 The magnetron sputtering 44
2.8 Reactive magnetron sputtering 45
2.9 High Power Impulse Magnetron Sputtering 47
2.9.1 Advantages of HiPIMS 50
2.9.2 Disadvantages of HiPIMS 50
2.10 The sputtering practical steps 51

Chapter 3: Numerical simulations of the sputtering process

3.1 Introduction 54
3.2 Numerical simulations of magnetron sputtering 54
3.2.1 Monte Carlo simulation Method 54
3.2.1.1 Understanding the Monte Carlo Simulation 55
3.2.1.2 Benefits and Drawbacks of Monte Carlo Simulations 55
3.2.2 The magnetron sputtering discharge 56
3.2.3 Magnetic field 56
3.2.4 The Particle-In-Cell/Monte Carlo Collision (PIC/MCC) 57
3.2.5 Kinetic approach 58
3.2.6 The fluid model 59
3.2.7 The hybrid model 60
3.3 The Sputtering Phenomena 61
3.3.1 Binary collision approximation 62
3.3.2 The molecular dynamics 64
3.3.3 The sputtering yield 64
3.3.4 Sigmund formula 65
3.3.5 Bohdansky formula 66
3.3.6 Yamamura formula 66
3.3.7 Eckstein formula 68
3.3.8 Sputtering interactions 69
3.4 Conclusion 72

Chapter 4: Results and discussions

4.1 Introduction: 73
4.2 **Part 1 Introducing the model SRIM for sputtering simulations** 73
4.2.1 SRIM on sputtering calculations 73
4.2.2 Sputtering yield depending on the energy of bombardment and fixed angles of incidence 77

4.2.3 Sputtering yield depending on incidence angles and fixed energies of bombardment ..78
4.2.4 Comparison between the two semiconductors CZTS and Silicon 79
4.2.5 The atoms ejected from each element of the compounds CZTS and CIGS 81
4.2.6 Comparison between the two compounds CZTS and CIGS 83
4.3 **Part 2: the transport of the atoms sputtered toward the substrate** 84
4.3.1 Simulation method 85
4.3.2 Influence of temperature and high pressure on the sputtered atoms arriving on the substrate using Argon and xenon gas 86
4.3.2.1 Variation of temperature with a fixed pressure for Argon ions: 86
4.3.2.2 Variation of pressure with a fixed temperature for Argon ions: 89
4.3.2.3 Variation of temperature with a fixed pressure for Xenon ions: 91
4.3.2.4 Variation of pressure with a fixed temperature for Xenon ions: 94
4.3.3 Comparison between materials 96
4.3.4 Analysis of the thin layer created by the deposition of the atoms ejected 99
General conclusion 105
References 108
Annex 116

List of Figures

Chapter 1

Figure 1.1	Thin film deposition techniques	16
Figure 1.2	Schematic diagram of a chemical vapor deposition	17
Figure 1.3	Schematic of vacuum evaporation process with E-beam heating	19
Figure 1.4	A simple ablation laser system	20
Figure 1.5	Principle process of molecular beam epitaxy	21
Figure 1.6	Typical sputtering deposition	23
Figure 1.7	The "diode" sputtering system	24
Figure 1.8	The voltage-current curve between the two electrodes during a glow discharge in a diode sputtering device	25
Figure 1.9	Principle of the triode-sputtering system	28
Figure 1.10	Magnetron sputtering schematic	29
Figure 1.11	Schematic diagram of a chemical vapor deposition (CVD)	32

Chapter 2

Figure 2.1	Elastic collision	37
Figure 2.2	Inelastic collision	38
Figure 2.3	Representation of the plasma's voltage profile and glow discharge	40
Figure 2.4	Evolution of the ionic and electronic densities of plasma in contact with a surface.	42
Figure 2.5	Child sheath thickness as a function of plasma density parameterized by sheath voltage and electron temperature	43
Figure 2.6	Schematic diagram of the working principle of magnetron sputtering	44
Figure 2.7	Diagram of interactions after a collision of argon ions on the target surface	45
Figure 2.8	Three reaction mechanisms between the reactive gas and the target atoms during sputtering deposition under reactive condition (O2 is an example of a reactive gas, and M symbolizes the metal atom from the target.)	46
Figure 2.9	An illustration of a medium frequency pulsed DC generator signal	47
Figure 2.10	Simple LC circuit constituting the artificial network for creating HiPIMS pulses	48

Figure 2.11	Characteristics of voltage and current for a typical HiPIMS discharge	49
Figure 2.12	Treatment steps to follow in a classic sputtering	51

Chapter 3

Figure 3.1	Three regimes of sputtering induced by elastic collisions.	62
Figure 3.2	Angular distributions of sputtered atoms from Ni by normally incident Hg+ ions	67

Chapter 4

Figure 4.1	Monte Carlo simulation flowchart	75
Figure 4.2	Sputtering yield as a function of the energy of the bombardment ions (Ar) on three incidence angles θ= [40°, 60°, 85°] calculated by MC method for (Cu2ZnSnS4)	76
Figure 4.3	Sputtering yield as a function of the energy of the bombardment ions (Ar) on three incidence angles θ= [40°, 60°, 85°] calculated by MC method for (Si)	77
Figure 4.4	Sputtering yield as a function of incidence angles on three energies E= [10(kev), 100(kev), 1(Mev)] calculated by MC method for (Cu2ZnSnS4).	78
Figure 4.5	Sputtering yield as a function of incidence angles on three energies E= [10(kev), 100(kev), 1(Mev)] calculated by MC method for (Si).	79
Figure 4.6	Comparison of Sputtering yield as a function of the energy of the bombardment ions (Ar) on three incidence angles θ= [40°, 60°, 85°] calculated by MC method between (Cu2ZnSnS4) and (Si)	80
Figure 4.7	Comparison of Sputtering yield as a function of incidence angles on three energies E= [10(kev), 100(kev), 1(Mev)] calculated by MC method between (Cu2ZnSnS4) and (Si)	80
Figure 4.8	Atoms ejected as a function of the energy of the bombardment ions (Ar) on the incidence angles θ= [85°] calculated by MC method for each element of the compound (Cu2ZnSnS4)	81
Figure 4.9	Atoms ejected as a function of the energy of the bombardment ions (Ar) on the incidence angles θ= [85°] calculated by MC method for each element of the compound (CuIn0.5Ga0.5Se2)	82
Figure 4.10	Comparison of Atoms ejected as a function of the energy of the bombardment ions (Ar) on the incidence angles θ= [85°] calculated by MC method between the semiconducting compounds (CZTS) and (CIGS)	84

Figure 4.11	Model used in the simulation	86
Figure 4.12	Number of arriving Si atoms as a function of the energy distribution using three different temperatures T= [100K, 300K, 600K]	87
Figure 4.13	Number of arriving Ge atoms as a function of the energy distribution using three different temperatures T= [100K, 300K, 600K]	87
Figure 4.14	Number of arriving Cu atoms as a function of the energy distribution using three different temperatures T= [100K, 300K, 400K]	88
Figure 4.15	Number of arriving Si atoms as a function of the energy distribution using three different pressures P= [0.5Pa, 2Pa, 5Pa]	89
Figure 4.16	Number of arriving Ge atoms as a function of the energy distribution using three different pressures P= [0.5Pa, 2Pa, 5Pa]	90
Figure 4.17	Number of arriving Cu atoms as a function of the energy distribution using three different pressures P= [0.5Pa, 2Pa, 5Pa]	90
Figure 4.18	Number of arriving Si atoms as a function of the energy distribution using three different temperatures T= [100K, 300K, 600K] with Xenon gas	92
Figure 4.19	Number of arriving Ge atoms as a function of the energy distribution using three different temperatures T= [100K, 300K, 600K] with Xenon gas	92
Figure 4.20	Number of arriving Cu atoms as a function of the energy distribution using three different temperatures T= [100K, 300K, 600K] with Xenon gas	93
Figure 4.21	Number of arriving Si atoms as a function of the energy distribution using three different pressures P= [0.5Pa, 2Pa, 5Pa] with Xenon gas	94
Figure 4.22	Number of arriving Ge atoms as a function of the energy distribution using three different pressures P= [0.5Pa, 2Pa, 5Pa] with Xenon gas	95
Figure 4.23	Number of arriving Cu atoms as a function of the energy distribution using three different pressures P= [0.5Pa, 2Pa, 5Pa] with Xenon gas	95

Figure 4.24	Comparison between arriving Si, Ge and Cu atoms as a function of the energy distribution for 0.5 Pa and 100K for a) Argon b) xenon	97
Figure 4.25	Comparison between arriving Si, Ge and Cu atoms as a function of the energy distribution for 0.5 Pa and 300K for a) Argon b) xenon	97
Figure 4.26	Comparison between arriving Si, Ge and Cu atoms as a function of the energy distribution for 0.5 Pa and 600K for a) Argon b) xenon	98
Figure 4.27	Comparison between arriving Si, Ge and Cu atoms as a function of the energy distribution for 2Pa and 300K for a) Argon b) xenon	98
Figure 4.28	Comparison between arriving Si, Ge and Cu atoms as a function of the energy distribution for 5Pa and 300K for a) Argon b) xenon	99
Figure 4.29	Deposition of the atoms ejected on the substrate for the semiconductors (Si and Ge) using 14cm distance	100
Figure 4.30	Deposition of the atoms ejected on the substrate for the metals (Cu and Ag) using 14cm distance	100
Figure 4.31	Deposition of the atoms ejected on the substrate for the semiconductors (Si and Ge) using 8cm distance	101
Figure 4.32	Deposition of the atoms ejected on the substrate for the metals (Cu and Ag) using 8cm distance	101
Figure 4.33	Deposition of the atoms ejected on the substrate for the semiconductors (Si and Ge) using 5cm distance	102
Figure 4.34	Deposition of the atoms ejected on the substrate for the metals (Cu and Ag) using 5cm distance	102

List of Tables

Chapter 4

Table 4.1	The percentage of atoms ejected on an argon bombardment energy of 100Kev for each material	83
Table 4.2	The total number of metals atoms arrived at the substrate depending on temperatures with argon gas ions bombardment	88
Table 4.3	The total number of metals atoms arrived at the substrate depending on pressures with argon gas ions bombardment	91
Table 4.4	The total number of metals atoms arrived at the substrate depending on temperatures with Xenon gas ions bombardment	94
Table 4.5	The total number of metals atoms arrived at the substrate depending on pressures with Xenon gas ions bombardment	96
Table 4.6	Total number of atoms deposited on the substrate on each material	103

Abbreviation list

PVD	physical vapor deposition
CVD	Chemical vapor deposition
LPCVD	Low-Pressure Chemical Vapor Deposition
kev	kiloelectron volts
MBE	Molecular beam epitaxy
Ar+	Argon ions
e^-	Electrons
Ar	Argon gas
DC	Direct current
TCOs	Transparent conducting oxides
ZnO	Zinc oxide
Rf	Radio frequency
HiPIMS	High Power Impulse Magnetron Sputtering
PECVD	plasma-enhanced chemical vapor deposition
Pa	Pascal unit
W	Watt
O_2	Dioxygen
N_2	Dinitrogen
H_2S	Hydrogen sulfide
Khz	Kilohertz
OES	optical emission spectroscopy
Ti	Titanium
µs	Microsecond
bar	Pressure unit
3D	three-dimensional
MC	Monte Carlo
∇	Del, or nabla
PIC/MCC	The Particle-In-Cell/Monte

Δ	Delta Symbol: Change in the value of a variable
(CFD)	Computational Fluid Dynamics
1D	One Direction
BCA	numerical models of the Binary Collision Approximation
MD	Molecular Dynamics
ACAT	Atomic Collisions in Amorphous Targets
TRIM	Transport of Ions in Matter
ACAT	Atomic Collisions in Amorphous Targets
ACOCT	the Atomic Collisions in a Crystalline Target
DYACAT	is the Dynamical simulation of Atomic Collisions in a Crystalline Target
TRIDYN	dynamic adaptation of TRIM
Y	The sputtering yield
ZBL	Ziegler-Biersack-Littmark
SRIM	Stopping and Range of Ions in the Matter
CZTS	Copper zinc tin sulfide
Si	silicon
CIGS	copper indium gallium selenide
θ	The angle of incidence
E	The energy of the bombarding ions
K	kelvin
Ge	germanium
Cu	Copper
SIMTRA	Simulation of Metal Transport
Ag	Silver
Xe	Xenon

General introduction

General introduction

The various effects produced by applying electricity to gas have been researched since the 19th century. To describe ionized gas in an electrical discharge, Langmuir and Tonk first used the term "plasma" in physics in 1928. Indeed, plasmas are made up of various particles including electrons, free radicals, positive and negative ions, photons, free atoms, and molecules in neutral and excited states, which can be compared to the complexity of blood.

Artificial plasmas are used both in industrial settings and in laboratories. They are also mainly known as electrical or gas discharges. These electrical discharges work by supplying a neutral gas with enough energy to ionize atoms by removing one or more of their electrons. The plasma is particularly intriguing due to the charged particles it contains and their interactions, which also enable a wide range of applications in fields including biomedicine, the environment, and agriculture. Surface treatments using plasma have also been developed in industries.

Plasma physical vapor deposition (PVD) has taken an important place in the research. One of the PVD processes is to deposit the species on thin films by sputtering from a target through ion bombardment. Sputter deposition is an adaptable and efficient coating method. In addition, thin films have several advantages, require little material, and make objects more resistant or give them unique properties. They are used for various applications, such as the semiconductor devices like thin film solar panels, aerospace, optics, watches, etc. Thus, it is necessary to understand the thin film deposition processes, therefore, understanding the flux and energy that the sputtered particles (neutral and ionized) deposit on the substrate is crucial to comprehending the mechanics of thin film formation. These particles exchange energy and have a big impact on the processes of elementary growth. Thus, they can ascertain the characteristics of deposits (grain size, crystallinity, etc.)

There are numerous sputtering sources, including diode, triode, magnetron, and ion beam sources. Magnetron sputtering, however, offers many benefits for deposition, it is a technique based on creating a localized plasma by using permanent magnets, which helps to trap the electrons in the vicinity of the cathode target and extend their lifetime. It is interesting to look into magnetron discharges because this process is the primary technology used by businesses to deposit thin films.

Many factors can impact the deposition of thin films during the magnetron sputtering, like the bombarding energy and angle of the ions, temperature, pressure, and the target-substrate distance, which lead to a bad coating and thickness of the thin film produced, so it is really

important to understand the influence of this factors on the atoms deposition to resolve the problems that you will face during this process and obtain a high-quality result.

Theoretical models were created to better understand discharge phenomena. Numerical simulations based on experimental results have improved due to computers' performance. Additionally, numerical simulations enable the prediction of system behavior and the discovery of the ideal operating conditions for industrial processes. Therefore, using numerical simulations offers the opportunity to lower the cost of experimental testing and design.

One of the most used programs to simulate the sputtering process is SRIM which is based on Monte-Carlo simulations, during the simulation, the ion moves in a series of discrete steps, each of which collides with an atom of the target in a random mode that reproduces the statistical properties of the shutdown processes. The evolution of the composition of binary thin layers has been studied experimentally and with a Monte Carlo models-based TRIM (transport ions in the matter) code, another Monte Carlo code SIMTRA was developed by Van Aeken for the simulation of trajectories of gas-phase particles in a definable 3D configuration where the interatomic collision modeling, the potentials and thermal motion of the background atoms are included in the code.

This work presented here aims to study the parameters that effect the magnetron sputtering and give some solutions to achieve better deposition of the atoms, to accomplish that, first will we make a simulation with SIMTRA model which allows us to calculate the sputtering yield in the discharge by varying the energies and the angles of incidence with the use of metals and semiconductors as a target. At the end of the simulation, we can deduce the maximum energy and incidence angle which represented the highest number of sputtered particles. Then, the transport of these species toward the substrate is handled by the SIMTRA code with a temperature variation (100, 300, and 600K) and pressure (0.5, 2, and 5Pa), finally, we will analyze the deposition of the atoms ejected by a target-substrate distance variation, the ultimate goal is to find out the effect of those parameters on the deposition of thin films and to deduce the finest adjustment for the magnetron sputtering that we should apply to acquire a maximum number of atoms arrived on the substrate.

Our objective is to participate in the resolution of problems bound to thin film technology development and to provide all the necessary information to help in the application of this method in advanced technologies as in electronics and photovoltaic cells.

Due to this, we separated our work into four chapters:

In chapter 1, we'll provide an introduction to thin film deposition. The discussion of the deposition processes that are most commonly employed in industry, such as physical vapor deposition and chemical vapor deposition, will be our primary focus. The many characterization techniques used to produce thin films will be described, more particularly the principle of the sputtering process by underlining the advantages and the difficulties encountered in its implementation. We'll focus on presenting different deposit approaches so that readers may recognize their value and comprehend the procedures involved.

Chapter 2 will cover plasma properties by understanding all the theories behind this phenomenon, then we will explain deeply the magnetron sputtering process by introducing the High-Power Impulse Magnetron Sputtering, which will give you an idea about the recent technologies concerning this process.

Chapter 3 is concerned with understanding all numerical simulation techniques related to sputtering.

Finally, the last chapter will be divided into two sections: the first part introduces the software used to simulate this phenomenon and provides results about the sputtering yield found by using the SRIM model, and the second and final part deals with the transport of the atoms sputtered towards the substrate by implementing all the factor which can impact the deposition calculated by SIMTRA model.

Chapter 1

Thin film deposition techniques

1.1 Introduction

The modern era of technology is greatly impacted by thin films. Thin films are considered the backbone for advanced applications in various fields such as optical devices, environmental applications, telecommunications devices, energy storage devices, and so on. Thin film morphology and stability are key factors that affect all applications. Deposition methods have a significant impact on the thin film's shape, chemical and physical methods can both be used to deposit thin films [1-5]. In this chapter, the basics and certain advanced thin-film deposition techniques are covered. Then we will describe more particularly the principle of sputtering by underlining the advantages and the difficulties encountered in its implementation. Finally, we will explain all the steps during the growth of a thin layer.

1.2 General methods of thin film deposition

The term "thin film" only applies to films that are micron- or submicron-thick. Chemical vapor deposition (CVD) and physical vapor deposition (PVD) [6, 7] are the primary techniques used to produce thin films under a vacuum. The classification of the methods is presented in the diagram of figure I 1 [8, 9].

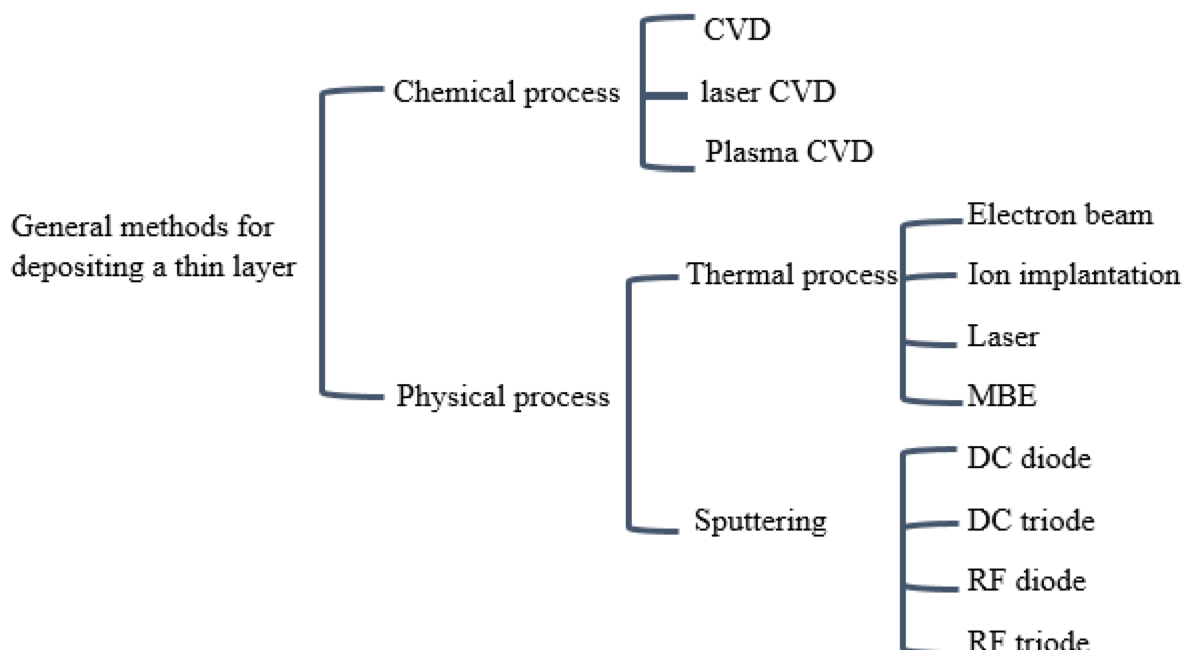

Figure 1.1. Thin film deposition techniques

1.3 Chemical vapor deposition (CVD)

Through a process called chemical vapor deposition (CVD), components of a gas phase interact to create a solid layer that is then placed on a substrate. A solid film is deposited on a substrate as a result of a reaction between gas phase elements. The volatile compounds of the material to be deposited are eventually diluted in a carrier gas and introduced into a chamber where the substrates are placed. The film is obtained by a chemical reaction between the vapor phase and the heated substrate. In some cases, a temperature increase is necessary to maintain the chemical reaction. CVD is an interdisciplinary field, it includes a set of chemical reactions, a thermodynamic and kinetic process, and a transport phenomenon [10]. The chemical reaction, which determines the nature, type, and species present, is at the center of these fields. The hot wall reactor and the cold wall reactor are two different types of reactors. The hot-wall reactor operates at a lower pressure of around $75\ mtorr$ since the latter is heated directly. As a result, deposits form on the substrates as well as the walls (LPCVD technique: Low-Pressure Chemical Vapor Deposition [11]). Since just the substrate is heated in the cold wall reactor, the reaction only affects the heated substrate and occurs at air pressure. The principle of this deposition method is presented in (figure 1.2).

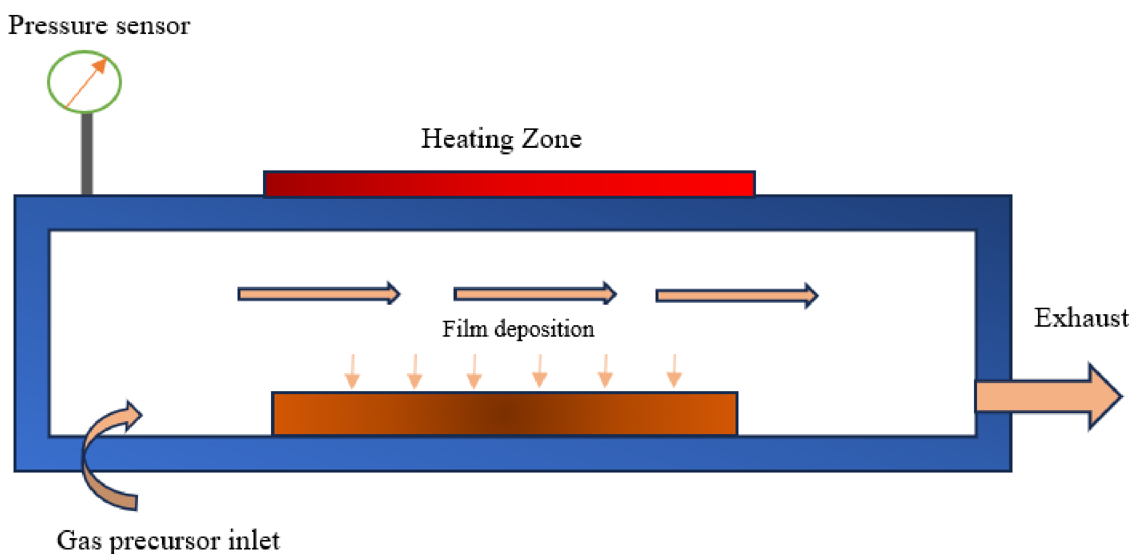

Figure 1.2. Schematic diagram of a chemical vapor deposition (CVD)

These techniques have made significant advancements recently, particularly in the creation of thin metal layers. This method has the following benefits: it makes it simple to obtain a sizable quantity of components or chemical compounds. It is possible to obtain superb layer quality, outstanding step coverage, and good adaptability in a production line. In addition, it offers the

possibility of selective deposition [12, 13], which eliminates an etching and planarization step of the surface. The disadvantages are the following: the films are not very dense, they are often contaminated by very reactive gases from the chemical reaction (hydrogen, fluorine, chlorine...), not every material can be deposited via CVD, and the system requires a substantial amount of installation. This is the reason why we did not choose this kind of procedure to create our thin film.

1.4 Physical Vapor Deposition (PVD)

In comparison to chemical vapor deposition, physical vapor deposition (PVD) has many benefits, including dense films, ease of control, and the absence of pollutants.

1.4.1 The evaporation processes

This method simply consists of evaporating or sublimating the material to be deposited in a vacuum crucible by heating it to a high temperature. A layer is created on the substrate when the evaporated material is condensed and deposited on it. The material can be heated using a laser, a powerful electron beam with an energy level of generally $5\ to\ 10\ ev$ [14], or a refractory filament through the Joule effect. The first is employed for the evaporation of materials that are simple to melt, while the second is employed for the evaporation of refractory materials. The deposition speed depends on the temperature of the source, the distance between the crucible and the substrate, and also on the sticking coefficient of the evaporated species on the substrate. It varies classically from 1 nanometer per minute to 10 micrometers per minute. The schematic diagram is presented in figure (1.3).

The easiest technique is evaporation because it doesn't require injecting gas to produce plasma, whereas other PVD techniques do. Nevertheless, several issues are unique to evaporation, such as the difficulty of depositing particularly refractory or low vapor pressure materials. Due to the distillation impact of the most volatile component, this process does not make it simple to manage the chemical composition of an alloy. The layers can also be contaminated by reaction with the crucible, with the filament, and especially by the degassing of the walls induced by heating or electron bombardment. In the case of electron beam evaporation, the soft X-rays emitted can cause crystal defects [15].

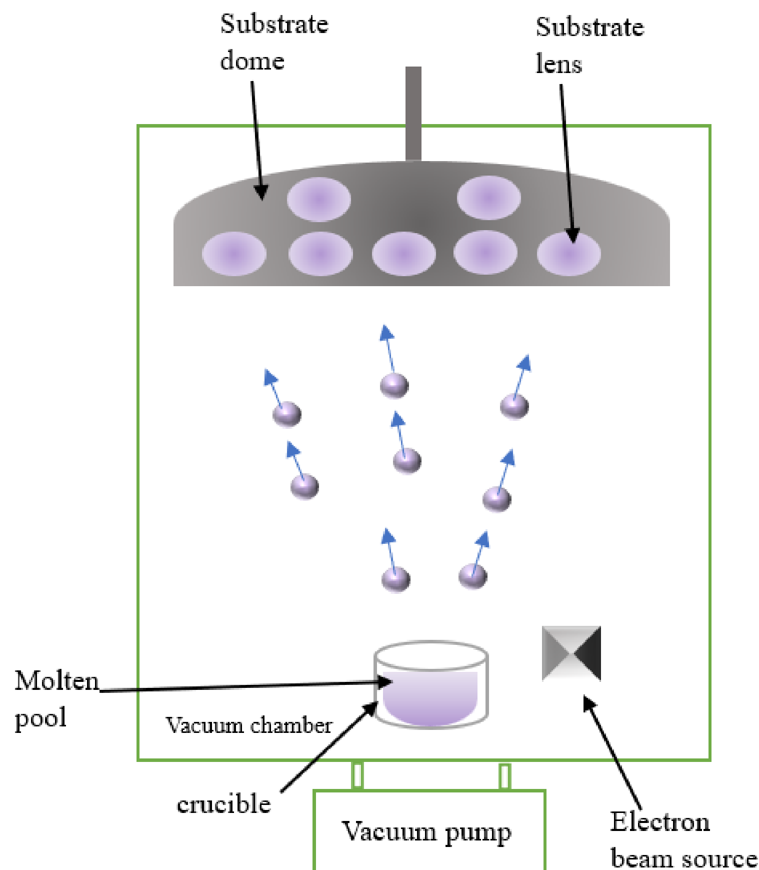

Figure 1.3. Schematic of vacuum evaporation process with E-beam heating

1.4.2 Laser ablation

This technique was proposed by the Bell Core team [16] and quickly applied by other groups. It is still vacuum evaporation, the energy being provided by the impact of a high-power laser beam, typically an excimer or YAG laser.

Laser ablation is one of the deposition techniques that have emerged in the last decade. It offers many advantages over traditional techniques such as the elaboration of a wide variety of materials especially oxides for applications in electronics and optoelectronics. This technique also allows for obtaining materials with unique macroscopic properties.

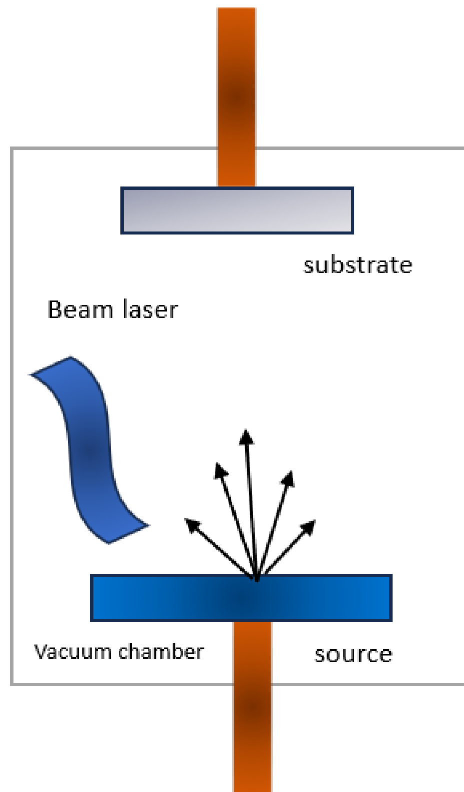

Figure 1.4. A simple ablation laser system

The principle of laser ablation (figure (1.4)) consists in focusing and irradiating a target [17], placed in an ablation chamber (under vacuum or gas atmosphere), and by an intense pulsed laser beam, these wavelengths span the infrared $(10m)$ through the ultraviolet$(193nm)$. A plasma with a very high particle density and high temperature will develop when the ablation threshold is exceeded. The target material determines the amount of laser fluence (energy per unit area) needed to create the plasma. In an atmosphere of neutral or reactive gas that may have an impact on the species of the feather or the surface of the growing film, the species will be ejected from the target as the layer grows pulse by pulse. To provide the adsorbed atoms and particles more energy and facilitate the thin film's crystallization, the substrate employed can also be heated.

Laser ablation advantages:

- The composition of the target material in the thin film under optimal growth conditions
- Possibilities of depositing several types of materials
- Simplicity of the technique and ease of implementation
- The possibility of obtaining films with fewer defects in the structures

On the other hand, this technique also presents a set of limitations among which a small deposition surface limited to a few cm^2 and the difficulty to control the defects of the crystalline structure of the layers that can be caused by the bombardment of the most energetic species of the plasma.

1.4.3 Molecular beam epitaxy (MBE)

The development of microelectronics and optoelectronics of compound semiconductors is based on the thin layer growth technique known as molecular beam epitaxy (MBE), which involves transmitting one or more jets of molecules of the material to be deposited as illustrated in figure (1.5). The jet is created through the evaporation process after being heated by the Joule effect, by radiation, or by an electronic bombardment [18].

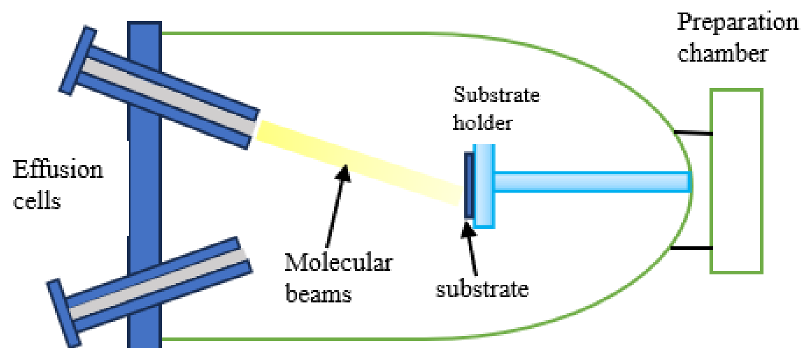

Figure 1.5. Principle process of molecular beam epitaxy

The deposition is performed under vacuum($< 10 - 6\ mbar$), the flow of molecules arriving on the substrate is controlled by the evaporation temperature of the material, and the nanostructure of the desired film depends on the exposure time of the substrate to the flow of molecules as well as to the alternation of the emitted atoms.

The MBE technique has several advantages citing the precise control of the growth parameters, the possibility to monitor in real-time the growth mode of the epitaxial layers, and to perform several in situ diagnostics [19].

The first works were performed in 1996 by M. A. L. Johnson. Recently the technique has been widely developed by introducing other techniques such as electron cyclotron resonance (ECR-MBE), MO-MBE (metal-organic molecular-beam epitaxy) using a metal-organic material as a precursor [20, 21].

1.4.4 The Sputtering process

1.4.4.1 History

The phenomenon of sputtering was first used in 1852 by Grove and in 1858 by Plucker. When an electrical discharge is applied between two electrodes in the presence of neutral gas, generally argon, under reduced pressure, the ions of the inert gas will bombard the target of the material on the cathode, and the particles ejected from the target will deposit on the substrate and form a thin layer. In 1972, the magnetron cathode appeared [22]. Magnetron sputtering is based on the principle of sputtering where a magnetron device is integrated.

1.4.4.2 General principle

The deposition process can be defined as the ejection of surface atoms from a target by ionized atoms created from a neutral gas and the transfer of these ejected atoms onto a substrate. The deposition takes place in a vacuum chamber where the target and the substrate are placed (figure (1.6)).

Three steps are involved in the creation of thin films via sputtering:

- The creation of a metallic vapor from a solid target.
- The movement of the ejected particles which form a vapor towards a substrate.
- Condensation and growth of the material particles on the substrate to form a thin film.

The creation of cold plasma is done by applying a sufficient potential difference between the cathode (target) and the anode within a rarefied atmosphere (generally argon). The plasma is composed of electrons(e^-) and positive ions(Ar^+). Under the effect of the electric field, the argon ions are attracted by the cathode and collide with the target causing the ejection of atoms in the form of species that condense on the substrate. The formation of the film is carried out progressively.

-In addition to the particles ejected from the target, other species come from the target; the secondary electrons, which then collide with argon atoms close to the target and form the ions (Ar^+).

In fact, the secondary electrons in the gas that are ejected from the target during the bombardment secure the discharge because, during inelastic collisions, they convert some of their kinetic energy into potential energy that the argon atoms can use to ionize.

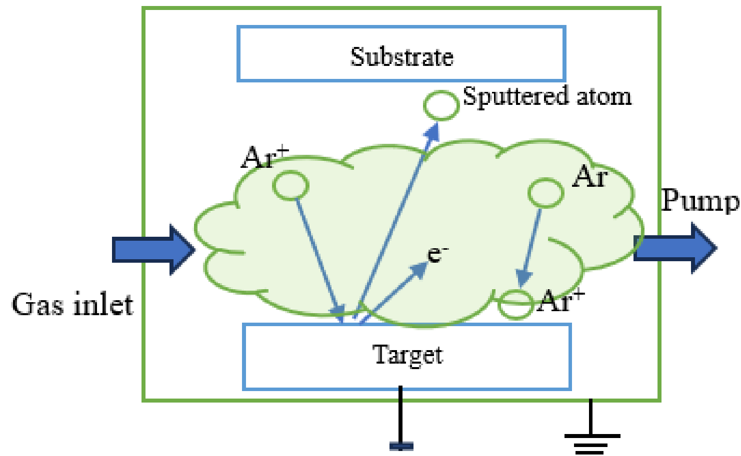

Figure 1.6. Typical sputtering deposition

1.4.4.3 Experimental device for the sputtering process

A sputtering plant consists of:

- A pumping system: composed of several primary pumps which allow reaching a vacuum between $10^{-2}mbar$ and $10^{-3}mbar$, and secondary pumps (high vacuum) to reach a vacuum between $10^{-5}mbar$ and $10^{-7}mbar$. The system is also composed of gauges.
- Magnetrons where the targets are placed [23].
- Power supplies that produce direct current (DC), pulsed current or radio frequency (RF).
- A cooling system (cold water) and hot water adapted to the different stages of the process.

1.5 Sputtering Methods

1.5.1 Diode sputtering in direct current

A diode-sputtering device is described in figure (1.7). This device is composed of a vacuum chamber with a residual pressure lower than $10^{-3}torr$, in which two flat electrodes, cathode, and anode, are placed a few centimeters apart. The cold cathode, on which the material is to be sputtered is fixed and connected to the negative pole of a voltage generator of a few kilovolts. The anode, on which the substrate is located, is connected to the ground [24].

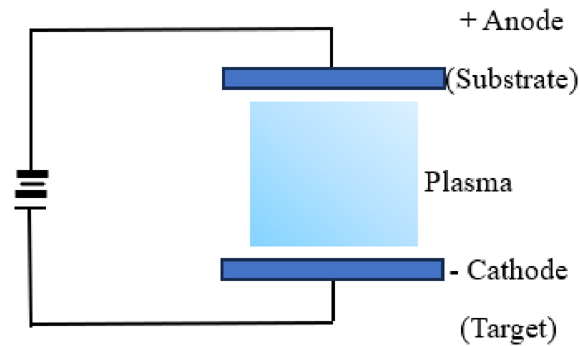

Figure 1.7. The "diode" sputtering system

1.5.2 Glow discharge

The gas discharge term is revealed by the electric current passing through a gaseous medium. For the current to flow, some of the gas molecules and atoms must be ionized, and it must then be propelled by an electric field. Because the discharge is powered by this discharge current, it must run continuously for the whole duration of the discharge.

The majority of the ionization takes place in the area in front of the cathode known as the cathode glow, therefore energy is crucial. Outside of this area, the discharge current is carried by electrons and ions in opposite directions, toward the anode and cathode.

In the case of a dc discharge, electron emission is essential to maintain the discharge [25]. In the cathode sheath region, the electric fields accelerate the secondary electrons, thus the ionization occurs and this discharge is controlled. For a dc discharge, the interactions between the electrode surfaces and the charged particles are essential to define the current. Between the two electrodes, the discharge is created and it depends on the nature of the working gas, its pressure, the applied voltage, and the geometry of the discharge [26]. In the beginning, the voltage is applied and the discharge current is low. Then, it remains nearly constant with increased voltage because this latter becomes large enough to collect the charged particles.

Figure (1.8) indicates that by increasing the voltage, the charged particles achieve enough energy so they can more produce charged particles by bombarding the electrodes, which is leading to the generation of secondary electrons or through collisions with the working gas atoms. The current increases when more charged particles are created, therefore the voltage is limited by the output impedance of the power supply and remains roughly constant [27]. This region is commonly referred to as the Townsend discharge.

The discharge current increases along with the voltage when it is raised further. The discharge then rearranges the vacuum potential structure to create a cathode sheath due to the high plasma density. As a result, ionization is more effective and the current is larger at a given voltage. It also quickly increases by several orders of magnitude and becomes independent of the external seed.

After that, a breakdown occurs, so the discharge becomes self-sustaining and takes the form of a glow, and the gas becomes luminous. The secondary electrons are emitted because of the bombardment of the electrode. The latter influences and ionizes the atoms of the working gas.

As a result, there are more ions available to bombard the cathode and produce further secondary electrons. At this instant, the voltage decreases, and the discharge current abruptly rises. By maintaining the distinctive glow through collisions, radiation is then released to de-excite the system. The term "dc glow discharge" or "normal glow" refers to this regime.

The cathode target surface is subject to greater ion bombardment as the current continues to rise and the discharge current establishes an ideal current density. The power supplied rises until a nearly uniform density is reached, covering the entire cathode region. The power rises and causes a discharge with a current density at the cathode when the entire cathode is bombarded by ions. As a result, greater currents and higher voltages are obtained over the cathode sheath, increasing both current and voltage. This operating procedure, often known as the abnormal glow, is employed for sputtering.

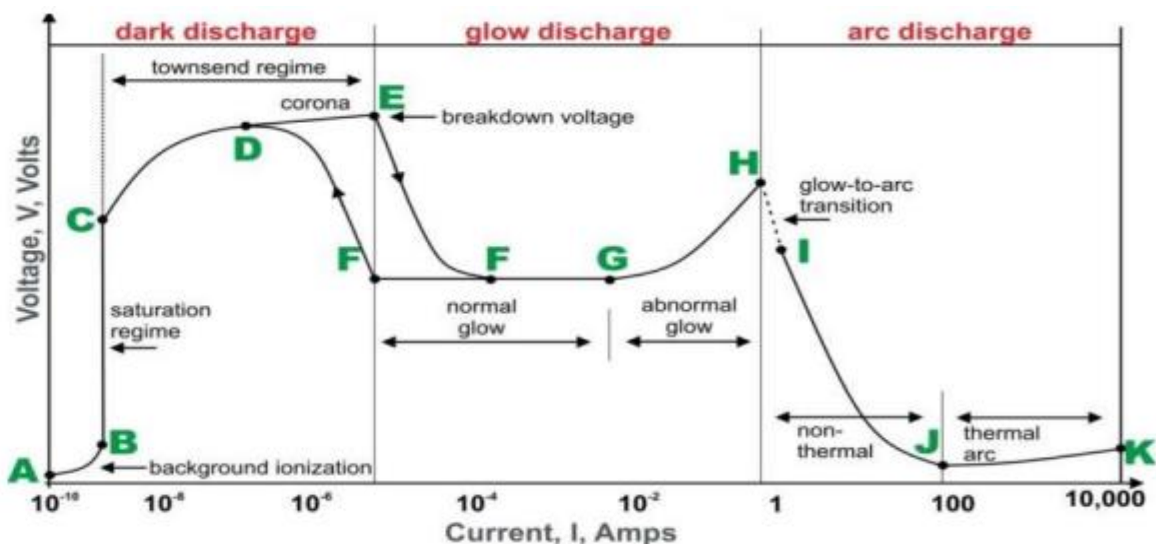

Figure 1.8. The voltage-current curve between the two electrodes during a glow discharge in a diode sputtering device [27].

1.5.3 Geometry of electrodes

Optimizing the spacing between the electrodes is necessary. In fact, if the distance is too great, the discharge is focused in the middle of these two electrodes, which results in the cathode's center being exclusively bombarded. When the distance is too close, the discharge disperses, leading to a selective bombardment of the cathode edge; in both of these scenarios, the film homogeneity is poor. This separation must typically range from a few millimeters to a few tens of centimeters. The cathode must always be cooled since the energy dissipation brought on by the ions' impact can lead it to melt.

The enclosure can be placed in a magnetic field. This field then tends to localize the plasma due to the action of the Lorentz force on the charged particles. The density of the plasma in the target can be increased, which increases the efficiency of the device. This is how sputtering is used for the creation of thin films. As we will see later, it is this property that we tried to use to study the distribution of the deposition rate in our sputtering device.

1.5.4 The limits of the "diode" device

The DC diode sputtering system has the advantage of being very simple to implement. Its major disadvantage is related to the need to use a high value of pressure $(10^{-1}\ or\ 10^{-2} torr)$ to maintain a stable discharge [28]. In fact, at high pressures, we observe in the deposited films the presence of non-negligible quantities of impurities, coming from:

- Bombardment gas, for example, argon occluded in the layers,

- residual atmosphere; for example, water vapor, oxygen, or organic molecules, which cannot be totally eliminated because of the low pumping dynamics in the considered pressure range

The presence of impurities in the enclosure is more noticeable at the level of the layers, due to the phenomenon of backscattering of the pulverized particles, the deposition speeds are relatively low: always lower than a few micrometers per hour. This old process is therefore not very efficient.

1.5.5 High frequency sputtering

The high-frequency device has the same basic design as a DC diode sputtering device, but instead of a DC electric field, it uses a high-frequency, alternating electric field that oscillates at megahertz frequencies ($1kv$peak-to-peak). This makes it possible to maintain the discharge

at pressures as low as $10^{-3} torr$. The high frequency electric field can be combined with a DC magnetic field to sustain a steady discharge up to about $10^{-4} torr$.

The majority of the atoms that the target ejects won't come into contact with the molecules of the leftover gas. Because in DC systems the electric charges of the ions attacking the target build on its surface, the method's fundamental benefit is that it permits the sputtering of any material, whether conductive or insulating [29]. As a result, the ions in the plasma are repelled by an electric field, significantly decreasing the sputtering efficiency. We decide to employ a high frequency plasma to prevent this. Regarding the triode system, a high frequency voltage is applied to the target. In this way, the charges that tend to accumulate are eliminated from one alternation to the next.

Consider, for illustration, a sapphire plate positioned on a conductor that has been exposed to a high frequency potential. When this conductor is made to have a negative potential concerning the plasma, it draws ions that cause the sapphire to sputter until the positive charges brought about by this creates a potential that is equal to and opposite to the conductor's potential. When the potential of the charges on the sapphire's surface equalizes the attraction of the ions, the sputtering ends. The plasma's electrons will be drawn to the conductor if its polarity is now reversed. By collecting on the target, these electrons will neutralize the positive charge, allowing the ions to attract once more during the subsequent alternation.

One of the most frequent applications of this method is the realization of multilayer insulating-conductive films with machines equipped with several high frequency targets. These machines are used to produce thin film capacitors. The deposition rates obtained with this process are directly proportional to the power applied to the target; the ionic current is also directly proportional to the power dissipated in the target. These processes require the use of high frequency power generators, target impedance matching devices, and all the technology specific to high frequency waves.

1.5.6 Triode sputtering

In DC diode or high frequency processes, the plasma is produced by a cold cathode discharge. This ion production process requires the use of relatively high voltages which is a disadvantage in some cases. In addition, there are not enough electrons to ionize the plasma. In the DC triode sputtering system, shown in figure (1.9), the discharge is produced by electrons filament from a hot cathode and accelerated in an electric field created by an anode which is a cylinder with

a potential of about $+150\ volts$ [30]. These electrons cause the ionization of a small fraction of the particles of the gas, one in ten thousand, being between these two electrodes

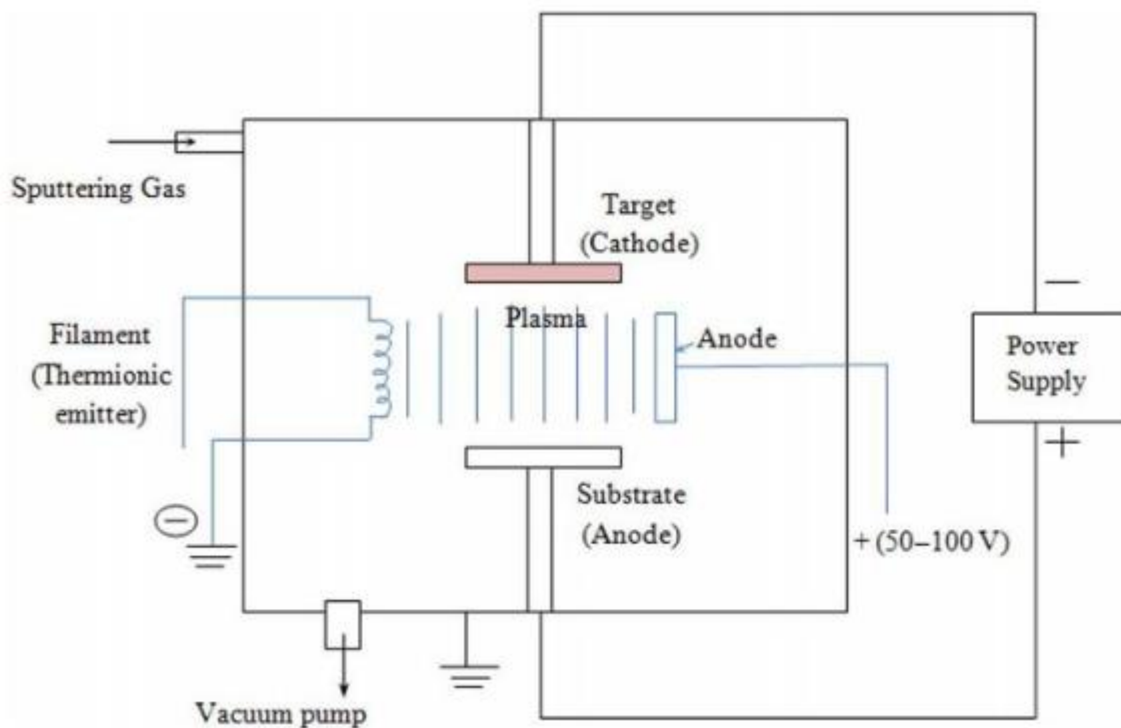

Figure 1.9. Principle of the triode-sputtering system [31]

A magnetic field superimposed on the electric field makes it possible to lengthen the electron trajectories to increase their probability of ionization by shock. This magnetic field also has the effect of concentrating the plasma in the central zone of the chamber. The filament, the anode, and the coil generating the magnetic field are plasma-generating devices independent of the target and the substrate. As the target potential does not influence the maintenance of the discharge, low voltages (500 to 1500 volts or less) can be used, which cancels out the risks of breakdown. This independence of the target from the plasma means that the target can be moved above the anode or given any shape. The substrate can also be moved at will and be given any shape.

In the triode system, the discharge can be maintained at a lower pressure of the order of $10^{-3} to\ 10^{-4} torr$, which is an advantage from the point of view of the contamination of the layers by the gas used to form the plasma. Moreover, this system presents very great flexibility of use: the target, independent of the plasma, is bombarded at low energies, which is not the case in the diode system.

1.5.7 Magnetron sputtering

In traditional sputtering, some electrons are propelled toward the wall chamber, causing heating and radiation (not all electrons contribute to working gas ionization). The magnetron sputtering technology was created to enhance the deposition procedure and prevent potential issues. This method involves applying a magnetic field perpendicular to the target's applied voltage. The secondary electrons released will be contained in an area near the target due to the intersection of these fields (the magnetic and electric fields). The likelihood of an electron colliding with an atom in the gas will significantly rise as a result of these electron accumulations. As a result, the plasma will become denser and ionization will rise. Figure (1.10) depicts the process schematic. The lowering of gas pressure is possible while using this technique. Since there are fewer collisions when the pressure is lower, the sputtering becomes more directed.

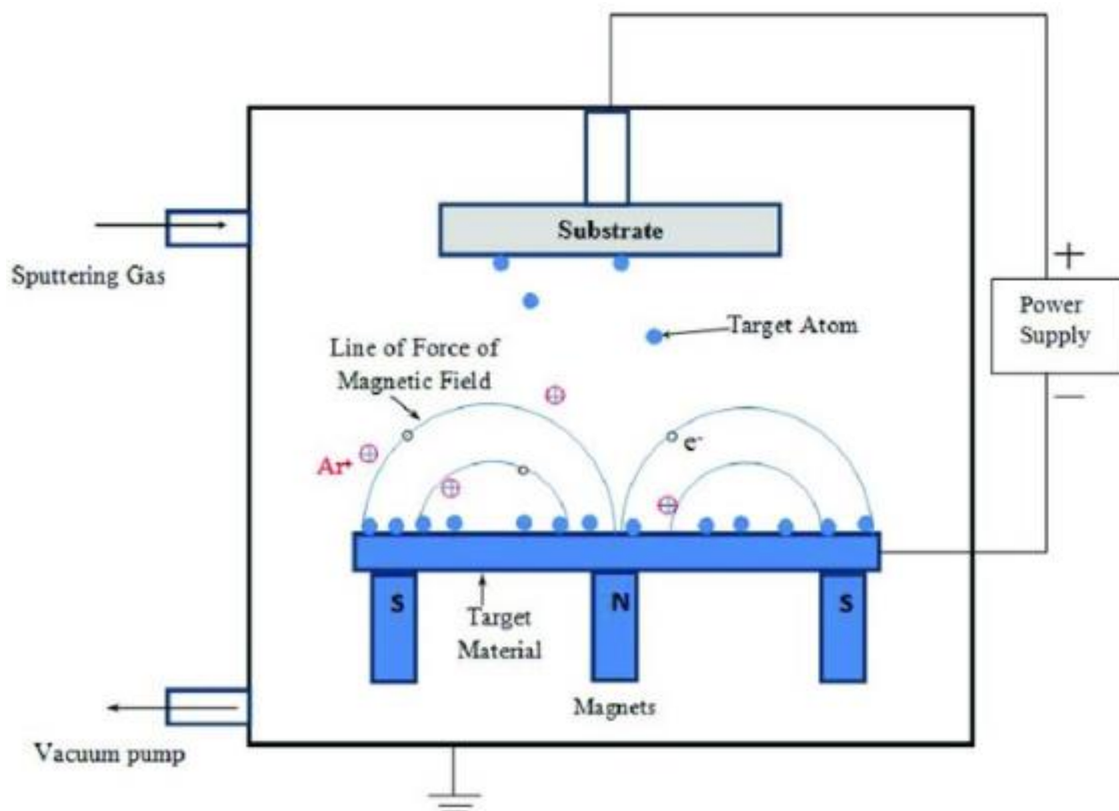

Figure 1.10. Magnetron sputtering schematic [31]

Magnetic fields that are perpendicular to the electric field are used to confine the plasma close to the target surface [32]. The magnetic field is created by magnets positioned beneath the target. The secondary electrons (emitted by the target during the bombardment) do not raise the substrate temperature because they are retained in helical routes around the target and do not bombard the substrate as a result [33, 34]. This enables the use of delicate substrates (like semiconductor oxide metal) and sensitive surfaces (like plastic), which results in minimal flaws.

1.5.8 Reactive sputtering

There is also another sputtering method, where the deposition is carried out in a reactive medium. It allows the synthesis of thin ceramic layers (oxides, carbides, nitrides, etc); following two methods:

- The sputtering of the desired ceramic target.
- The sputtering of a metallic target in the presence of reactive gas.

Argon is the most used gas in the case of reactive sputtering, because of its chemical inertia, the reactive gases used to manufacture nitrides are nitrogen (N_2) and ammonia(NH_3), for oxides; oxygen (O_2) and (H_2O), and for carbides: $(CH_4) and\ (C_2H_2)$.

The advantages of this technique are [35]:

- The increase in the deposition speed.
- Decrease the working pressure.
- The increase in the purity of the thin layers.

Sputtering remains the closest technique to microelectronics. It has received extensive research and use, particularly for metallic deposits. Because it doesn't subject the coatings to a severe heat treatment, which is relevant for the development of sensors where it's important to control the morphology of the material, which depends on the deposition conditions and characteristics like the thermal treatment.

1.6 Growth of a thin layer

Initial stage and intermediate growth are typically two stages that are significant in the evolution of thin film growth. The substrate's physical and chemical characteristics, as well as how it interacts with the incoming particles, are crucial at the early stage. After the initial layers covering the substrate are produced, the intermediate growth phase starts, during which only the interactions between the particles and the film take place. The grain structure and surface morphology are thus determined by the physical surface processes as the films grow and evolve. They are:

- Bombardment on the substrate surface/film;
- Adsorption of the atoms in the collision;
- Diffusion of the atoms on the surface of films.

These processes are related to the absorption energy at the moment of collision and the angle of atoms incidence, physical and chemical interaction between the atoms and the substrate/film surface, and especially the substrate temperature. A model that correlates the grain structure and surface morphology was proposed by Thornton in 1974 [36] and is called the "zonal structure model". This model explains the growth of the grain structure in four different zones: Zone I, Zone T, Zone II, and Zone III, as a function of the argon pressure and the TS/Tm ratio, where TS is the substrate temperature and Tm is the melting temperature of the material to be deposited. Originally, this model was developed to describe the growth of metals deposited via sputtering. However, in the literature, this model is also widely used to describe the film growth of different materials deposited by the same technique.

There are fundamental differences between TCOs and metals, so Kluth et al. [37] suggested modifications of the original Thornton model. First, the ZnO exhibits a high melting temperature (1975°C) when compared to the typical metal temperature. However, the ratio between the substrate temperature TS and melt temperature of the material to be deposited Tm (considered in the Thornton model) becomes very small at typical TS (80- 400°C) intervals during sputtering deposition. In this case, the modified Thornton model is analyzed as a function of substrate temperature and not as a function of TS/Tm ratio.

Figure (1.11) shows the three zones present in the modified model as a function of the working pressure and the substrate temperature (TS). From this, it is noted that due to the high melting point of ZnO (1975 °C) Zone III, which corresponds to the grain recrystallization in the original model, is not present in the range temperature used in this case, since recrystallization appears at elevated substrate temperature. One point of the Thornton model is maintained: the increase in TS and the reduction of working pressure lead to an increase in the compaction and density of the film structure. For a better understanding, the characteristics of each zone are detailed below:

• Zone I: low atom diffusion, narrow conical crystallite structures separated by voids (Figure 1.11a);

• Zone T is the transition region: the diffusion of the atoms is large and there is a filling of voids found in zone I. So, it is difficult to identify outline grains. The structures are dense with "V" -type fiber-like grains and exhibit a relatively smooth surface;

• Zone II: high diffusion and the migration effect on grain boundary become dominant. In this case, the larger grains grow at the expense of smaller grains and follow a preferential

orientation, resulting in a columnar structure of crystals of the same orientation. This zone is shown in Figure (1-11b).

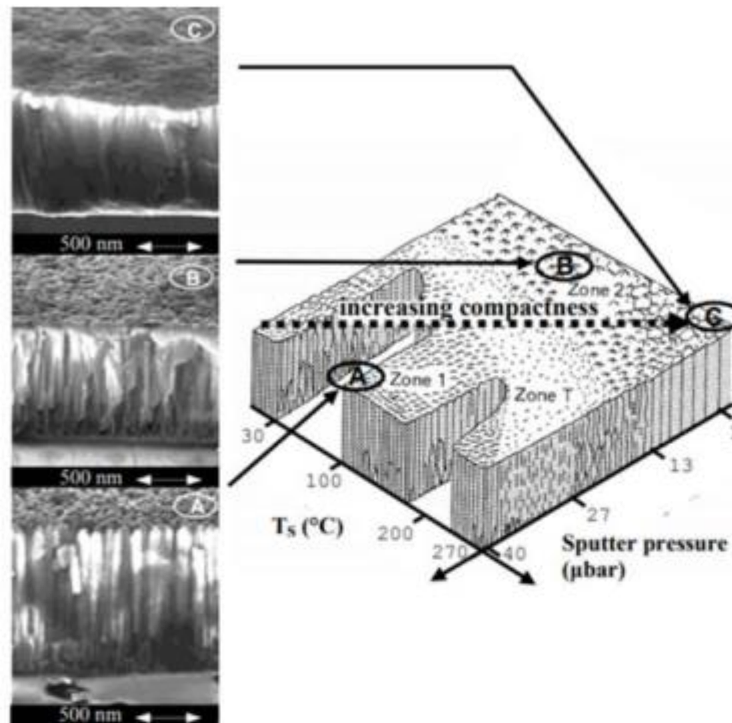

Figure 1.11. Adapted scheme of the modified zone structure model for ZnO: Al films proposed by Kluth et al. The micrographs highlight the growing zone and show the shape of these films [37]

With rising argon pressure, the energy of the particles reaching the substrate or film surface drops due to collisions with the argon atoms, which results in a decrease in energy for the diffusion surface. The adsorbed argon atoms also restrict the mobility of the atoms at high pressures. As a result, as argon pressure increases, so does the temperature transition between Zones I, T, and II. On the other hand, since this transition is governed by internal material diffusion, the temperature between Zones II and III is independent of the argon pressure. Sputter-grown ZnO thin films feature a polycrystalline surface morphology. The crystallographic caxis of each grain is parallel to the support and tightly aligned. During deposition, several surface morphological features develop. For example, in crystalline substrates such as silicon, the growth evolution occurs in structures with small grains. On the other hand, in amorphous substrates such as glass, there is growth in columnar grains that increase in size with film thickness.

1.7 Conclusion

Because thin film technology is constantly evolving, it is crucial to understand and stay current with it. For this reason, we have covered the many methods for producing thin films in this chapter. By understanding these methods, you will be able to contribute to this study.

Chapter 2

Plasma and magnetron sputtering

2.1 Introduction

Many scientists have expressed interest in using the highly ionized plasmas produced by magnetron sputtering. With the help of this new technology, it is feasible to produce an extremely thick plasma with significant particle ionization. In fact, by sputtering the target, the bulk material is broken down into atoms, which then condense on the substrate's surface and can be processed. Due to the invention of HiPIMS, this method is frequently employed to deposit thin films. Since these particles can affect the fundamental development processes and affect the characteristics of deposits, it is crucial to understand the flux and energy that the sputtered particles deposit on the substrate. That is why in this chapter we will first explain the plasma formation, then we will talk about the magnetron sputtering process and its characteristics.

2.2 Plasma properties

2.2.1 Plasma

When he was looking into electric discharges in 1923, Irving Langmuir coined the term "plasma," which is used to describe ionized gases. Fully or partially ionized gases, plasmas are made up of neutral species as well as positively or negatively charged species. Plasma is also referred to as the fourth state of matter. Because a solid material is in thermal equilibrium, it changes from a solid to a liquid when the temperature rises without changing the pressure. The liquid turns into a gas when the temperature is raised. If the temperature kept rising, eventually the atoms would break down into free-moving charged particles, such as electrons and positive ions, and the substance would reach the plasma state [38].

2.2.2 Cold Plasma

Neutral particles that are not in thermodynamic equilibrium and have a gas temperature close to room temperature make up the cold plasma. This plasma can be produced by an electrical discharge started from a power source between two electrodes, cathode, and anode, via a gas at low pressure. The charged particles will be accelerated by the electric field, increasing their energy. The electric field will accelerate electrons more quickly because of their smaller mass. As a result, the electron has a distinct temperature from ions and neutrals. These plasmas can be utilized for etching, physical vapor deposition (PVD), plasma-enhanced chemical vapor deposition (PECVD), and other surface treatment processes in the microelectronics and surface treatment sectors.

2.3 Characteristics

Three qualities, such as density, temperature, and degree of ionization, are primarily what define plasmas.

2.3.1 Density

The number of charged particles per unit of volume is represented by a species' density, which is often given in terms of cm^{-3}. As we've seen, a plasma's average neutrality is maintained and it is made up of neutral atoms, electrons, and ions (positive or negative). That implies:

$$n_{e^-} + n_{i^-} = n_{i^+} \tag{2.1}$$

n_{e^-}: The density of electrons.

n_{i^-} , n_{i^+}: Density of negative and positive ions.

Each of these species moves randomly, and the energy it possesses is based on its mass and the collisions it experiences with the gas around it. The plasma is mostly composed of neutrals, ions, and electrons.

A probability distribution function is used to represent the velocity profiles of these objects. The probability density function is translated into the majority of situations by the Maxwell-Boltzmann type, which causes the amount dN of a species to have energy between E and E + dE:

$$f(E) = \frac{dN}{N} = \frac{1}{n^{\frac{1}{2}}} \frac{1}{(KT_j)^{\frac{3}{2}}} \exp\left(-\frac{E}{KT_j}\right) \sqrt{E} dE \tag{2.2}$$

K : is the Boltzmann constant ($K = 1.38 \times 10^{-23} J.mol^{-1}.K^{-1}$)

T_j : represents the absolute temperature associated to the population j (j= electrons, ions, neutrals).

It approximates the distribution function of the species found in the plasma to some extent. Few species will have extremely high energy, while the majority of species will have relatively low energy.

2.3.2 Temperature

The average energy, denoted by the symbol EC, can be deduced from this distribution function (in the Maxwellian example). The population's temperature is determined from this value. Consequently, it is expressed in electron volts and signifies energy.

$$< E_{C,j} >= \frac{1}{2} M_j < v_j^2 >= \frac{3}{2} q T_j \quad (2.3)$$

q: is the electron charge.

2.3.3 Ionization

The ratio of positively or negatively charged species to the overall density, which is known as the plasma's degree of ionization(α), is defined by:

$$\alpha = \frac{n_i}{n_0 + n_i} \quad (2.4)$$

Where the densities of ions and neutrals, respectively, are n_i and n_0[39].

2.3.4 Collisions

Collisions in cold plasma can halt the movement of both charged and uncharged species. A collision may result in the transfer of energy or an impulse. As a result, distinct mechanisms govern how plasma species interact with one another. There are two collision scenarios to take into account. The first one is referred to be elastic (view figure 2.1) since no energy is lost when two particles contact; only their trajectories are altered.

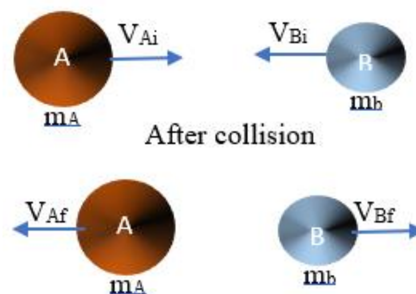

Figure 2.1. Elastic collision

In contrast, in the second scenario, when the collision is inelastic (view figure 2.2), there is an energy exchange or loss that allows for the production of excited or charged particles or even their dissociation. These particles' size and speed will have an impact on how they behave.

Additionally, there are secondary reactions in which the heavier particles contact with one other and primary reactions in which the collisions are caused by electrical impact.

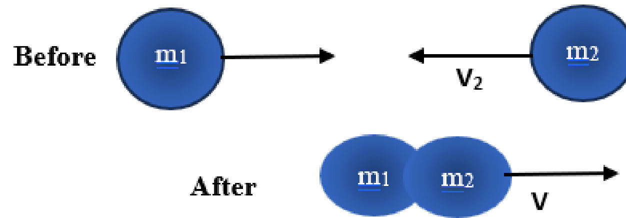

Figure 2.2. Inelastic collision

2.3.5 The free path

The median distance covered by particles between two collisions is known as the mean free path. It is measured in length units and is influenced by the density of the constituent particles and the probability that they interact with each other, it is expressed in the following way:

$$\lambda = \frac{1}{\sigma . n} \tag{2.5}$$

σ : is the collision cross section.

n : is the particle density.

The type of particles that are present and the pressure both affect the mean free path because for a gas P = n K T. The relationship between the pressure and the mean free path is demonstrated by the equation below:

$$\lambda = 8.34 \times 10^{14} p \frac{(\varphi_{a+}\varphi_g)^2}{4} \sqrt{1 + \frac{M_a}{M_g}} \tag{2.6}$$

Where $\varphi_{a,}\varphi_g$, $M_a$and $M_g$are diameters of the material's (or gas') atoms, the atomic masses, respectively, and p is the working pressure. Typically, the working pressure affects how the mean free path of elastic interaction between an electron and an argon atom evolves.

2.4 The collisional process

This process, in terms of particle density or energy, occurs when the plasma enters an inhomogeneous condition. Making all particle directions equally probable after contact is the purpose of the role. Because the environment has different densities in different areas, there is a net movement of particles from the higher density area to the lower density area. Furthermore, the diffusion of charged particles in a plasma can function as an efficient method of particle

eradication due to recombination on the plasma walls. The walls also have a low density of charged particles. A flow of species-specific particles can be used to describe this diffusion.

2.5 Emission of secondary electrons

The emission of secondary electrons is crucial to the discharge. The target, which is attached to the negative high voltage, is bombarded by neutrals or ions, causing this emission to occur. Depending on the type of plasma and the surface's substance, each plasma that comes into touch with the surface may respond differently.

Different reactions are thus possible depending on the kinetic energy of the impacting particle. Two primary processes follow a particle's collision on a surface: sputtering and the emission of secondary electrons. We shall discuss them as well as the electric potentials that are brought on by these charge movements. A so-called secondary electron can be ejected from an ion or an accelerated electron when they are interacting with a surface and are sufficiently energetic.

Two essential discharge mechanisms are the secondary emission phenomena and the coefficient of initial ionization. In order to keep the discharge going, secondary electrons are crucial. Additionally, the secondary emission yield shows how many electrons were ejected for each incident ion. It depends on many factors, including the object being bombarded, the incident species, its kinetic energy, and its surface characteristics.

Furthermore, the surface condition, including its level of oxidation, has an impact on the emission of secondary electrons. The sputter targets are held at high negative potentials, so secondary electrons with initial energy equal to the target potential are propelled away from the target surface. When the electrons ionize the neutral working gas, the discharge can occasionally continue. The target will next be bombarded by these ions, which will release more secondary electrons [40, 41].

The transfer of potential energy from an incoming ion or atom to an electron in the target is what causes electron emission. The energy-dependent component of secondary electron emission yield known as kinetic emission occurs when an electron in the target receives enough kinetic energy from the bombarding particle. The secondary electron emission yield is dependent on the bombarding particle energy when it is close to the threshold energy and on the bombarding velocity when the energy is larger, according to experimental evidence and theoretical calculations [42].

The secondary electron emission in HiPIMS discharges is influenced by the potential energy (ionization potential) of the incoming ion projectile. For the potential emission to take place, the projectile's potential energy must be greater than twice the work function of the target material [43]. The secondary electron emission coefficient γ is defined:

$$\gamma = 0.016(E_i - 2\varphi) \tag{2.7}$$

E_i : The ionization energy.

φ : The electron extraction energy of the target material.

As a result, the secondary electrons can directly ionize the process gas and provide other electrons energy, enabling them to produce ionizing collisions. The discharge is driven by secondary electrons.

2.6 Sheath

In general, the plasma is neutral because it contains an equal number of positive ions, neutral atoms, and electrons (fig. 2.3). However in contact with a surface, plasma sheaths appear.

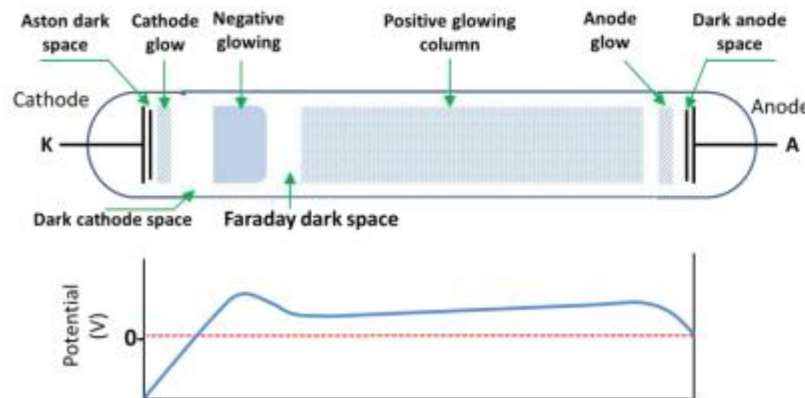

Figure 2.3. Representation of the plasma's voltage profile and glow discharge [44]

The charge neutrality of a plasma discharge is its defining characteristic, except for the regions near the surface when the charge neutrality is broken. "Sheath" is the term for these areas. The sheath development results from the charged species' different degrees of mobility [44]. Indeed, the electrons, which have a mass four orders of magnitude lower than the positive ions, reach the surface elements far more quickly than the ions, causing electron depletion and the generation of the space charge. As a result, an electric field that is directed from the plasma's neutral zone to the surface is created. The sheath is a non-neutral zone that is created to maintain the proper balance of ion-to-electron losses [45].

The positive ions that are crossing the sheath gather energy and are vertically orientated while being affected by the electric field. Anisotropic etching of the patterns is produced in semiconductor manufacturing by making use of this physical feature. Physical vapor deposition (PVD), in which the energetic ion (argon ions) sputters the target atoms, makes use of the acceleration of positive ions through the sheath. After that, the latter is placed on the substrate to create a thin layer.

Two types of sheaths exist in addition to that. The first one is referred to as a cathode sheath, in which neutrality is not observed and the flow of charged particles is managed. When an element is in this zone, it will tend to attract the closest ions and reject the weakest electrons, but as it goes away from the surface, this impact diminishes.

The second type is known as an anode sheath, and it refers to the situation in which the voltage is positive or connected to the ground. Three areas are involved in the sheath's creation [46]. Starting with the plasma, moving on to the pre-sheath, and then eventually reaching the sheath. As we previously stated, plasma is distinguished by its neutrality. The ions are then driven by the space charge field, and because the neutrality is retained in the pre-sheath region, they will gain the energy required to penetrate the interior of the sheath.

When the stationary state is eventually reached, which is when the flux of ions equals the flux of electrons, the surface has a negative electric potential known as floating potential. The electrons leave behind negative charge vacancies as they exit the sheath, which allows the plasma to regain its neutrality and develop a positive potential known as plasma potential.

For a plasma powered by direct current, the plasma potential is minimal, hovering about a few volts. Additionally, because the potential is always negative, it is larger than the floating potential and will confine the electrons within the plasma as a result.

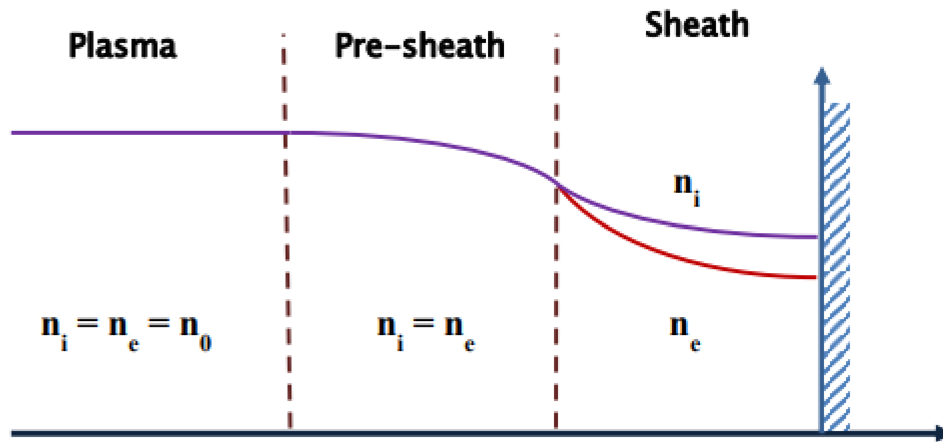

Figure 2.4. Evolution of the ionic and electronic densities of plasma in contact with a surface [45]

The sheath initially expands at the characteristic time of the inverse electron plasma frequency. The sheath grows as the ions are propelled toward the target surface, and the thickness asymptotically approaches the new equilibrium value [47].

Child law is used to measure the thickness of a collisionless sheath:

$$S = \frac{3}{4}\left(\frac{\varepsilon_0^2 V_{\text{sheath}}^3}{e n_0^2 k T_e}\right)^{1/4} \tag{2.7}$$

Whit ε_0 the permittivity of free space, e the elementary charge, k the Boltzmann constant, n_0 the plasma density and T_e the plasma electron temperature.

The sheath thickness is dynamic and is influenced by the sheath voltage, electron temperature, and instantaneous plasma density (see figure 2.5). When a sheath is present, the voltage in a small area drops dramatically, creating a powerful electric field. There is also a voltage drop in the anode sheath, however, it is less significant because the anode is not polarized. The plasma bulk is slightly positively charged to preserve electroneutrality to compensate for the sheath voltage drop.

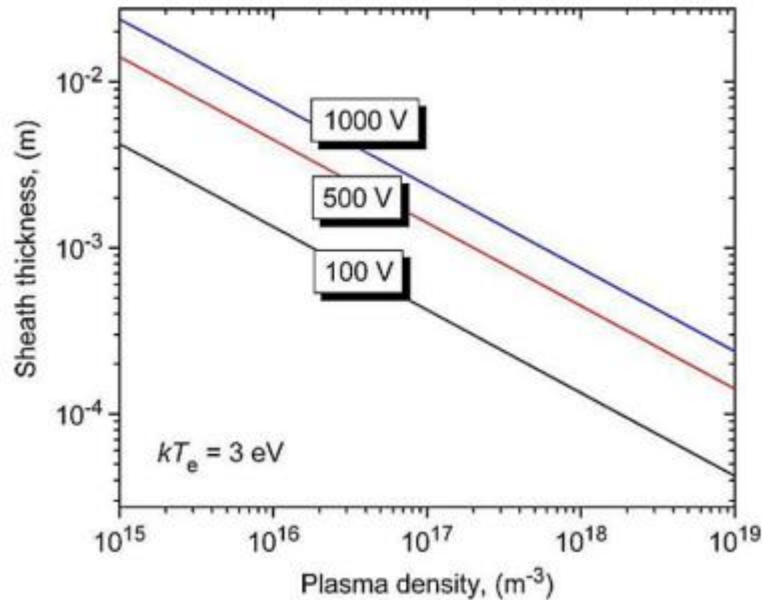

Figure 2.5. Child sheath thickness as a function of plasma density parameterized by sheath voltage and electron temperature [46]

The electric field accelerates charged particles (such as electrons or argon ions) in the cathode sheath. In order to increase their chances of colliding with argon atoms, argon ions are propelled toward the target and surface electrons into the main plasma region. Two different kinds of interactions take place in the bulk plasma region: The first is the elastic interactions (equation (2.8)) that cause electron scattering. Inelastic collisions, which transmit kinetic energy from the electron to the atom, are the second form of interaction. According to equations (2.9) and (2.10), inelastic collisions can cause atom ionization or excitation. Atomic ionization, which take place in the cathode sheath region and contribute to the plasma creation and maintenance, produce the electron-ion pair. Equation (2.10) describes a process that occurs after argon excitation and descends to a low energy level, which is what causes the plasma bulk region to glow.

$$e^- + Ar^0 \rightarrow e^- + Ar^0 \tag{2.8}$$

$$e^- + Ar^0 \rightarrow 2e^- + Ar^+ \tag{2.9}$$

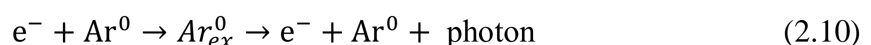

$$e^- + Ar^0 \rightarrow Ar_{ex}^0 \rightarrow e^- + Ar^0 + \text{photon} \tag{2.10}$$

2.7 The magnetron sputtering

The scientist Grove made the first record of the sputtering phenomena in 1852. Today, the sputtering method of thin film deposition has attained a high level of industrial maturity. This technique has applications in the mechanical, optical, electronic, chemical, and aeronautical fields, among others. The industrial development of magnetron sputtering for the synthesis of metallic or ceramic coatings has resulted from technological advancements connected to control devices and generators during the past years.

The basics of magnetron sputtering:
A schematic of the magnetron sputtering device is shown in figure (2.6).

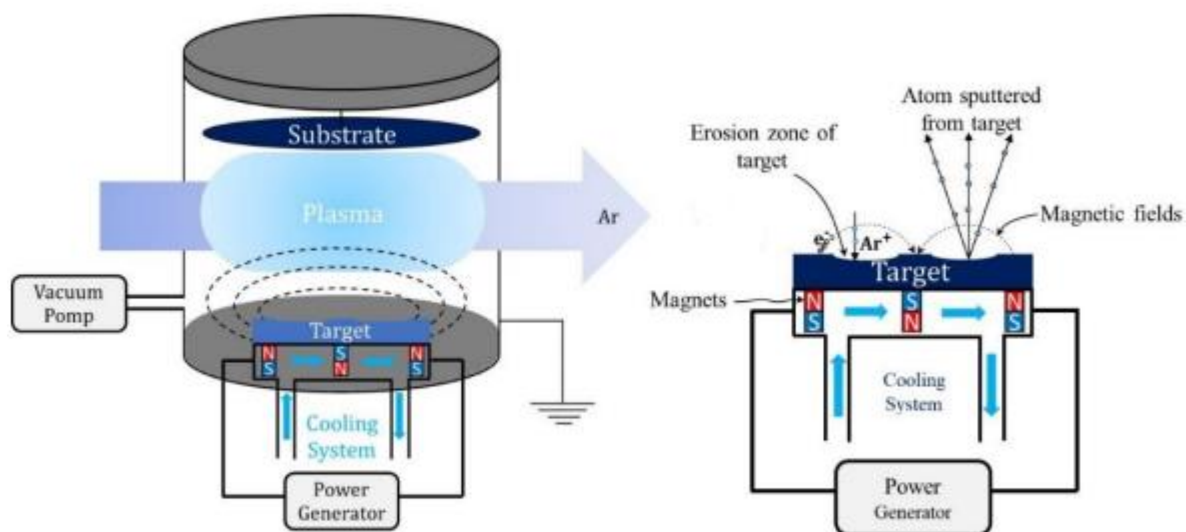

Figure 2.6. Schematic diagram of the working principle of magnetron sputtering

In front of the substrate holder are the targets made of the materials that will be deposited. Using a pumping device, the chamber has previously been pumped to a limited vacuum on the order of 10^{-4} Pa. (a primary pump and a secondary pump). To maintain the operating pressure, an inert gas (usually Ar) is supplied into the chamber at a flow rate managed by mass flow controls. The target is then made potentially different from the reactor walls, which serve as the anode, with the aid of a generator. The cathode (target) attracts the Ar+ ions, which collide with it under the influence of the electric field. When they make contact with the target's surface, they release their energy. This may cause an atom to be ejected by momentum transfer, the incident ion to be implanted, the neutralized ion to be elastically reflected, or electrons to be emitted that will support the discharge. Figure 2.7 illustrates the many steps involved in the bombardment of incident ions.

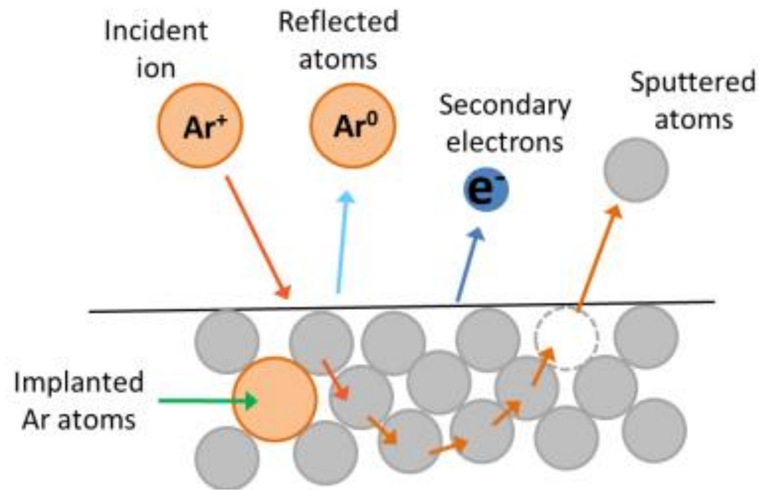

Figure 2.7. Diagram of interactions after a collision of argon ions on the target surface [49]

The target's back is equipped with two concentric magnets with opposing polarity. They produce a magnetic field whose lines are perpendicular to the electric field and parallel to the target surface. Under the combined impact of these two fields, the secondary electrons that the target emits are trapped on a cycloidal trajectory in front of the target surface. This results in a higher argon ionization rate close to the target. As a result, the discharge can be stabilized at lower working pressures (0.1–1 Pa) than in diode sputtering (20 Pa). Additionally, this permits the synthesis of thicker films and an increase in the deposition rate of up to 50 times [48, 49].

2.8 Reactive magnetron sputtering

Breakdowns can occur from bombarding a non-conductive target, which would be detrimental to the coatings' quality (defects). Depositing conductive materials is a good fit for the traditional sputtering process (DC power supply to the target). There are two ways to make dielectric films: by RF (radio frequency) sputtering from a target of a ceramic compound or by sputtering from a target of metal with a metalloid supply through a reactive gas. This process is known as reactive magnetron sputtering.

The target receives a potential modulation from the generator during RF sputtering (usually at 13.56 MHz), which keeps charges from building up on its surface and enables the maintenance of a stable discharge. Therefore, using targets made of non-conductive materials, this approach successfully creates highly insulating dielectric sheets. However, the usage of RF generators is restricted in many industrial production areas due to the price of power sources, reduced deposition rates, and implementation issues. On the other hand, there are numerous benefits to magnetron sputtering from metallic targets in reactive settings. [50]:

-It enables the production of substances with varying stoichiometry and deposition rates appropriate for industrial applications.

- The targets are frequently of higher chemical quality, and the deposited films typically exhibit very little impurity.

- Since the metallic targets are thermally conductive, cooling is effective. As a result, the range of applied power can be increased, for instance, to a value close to $50\ w/cm^2$, without running the risk of melting or shattering the target.

Creating thin films of compounds from metal targets, such as oxides, nitrides, or sulfides, is frequently done using the magnetron sputtering method under reactive circumstances. The carrier gas (Ar) and reactive gases (O_2, N_2, and H_2S) are both introduced into the vacuum chamber at the same time during the sputtering process. According to the three methods depicted in Figure 2.8, the reactive gas can react with metal atoms from the target using oxygen as the reactive gas.

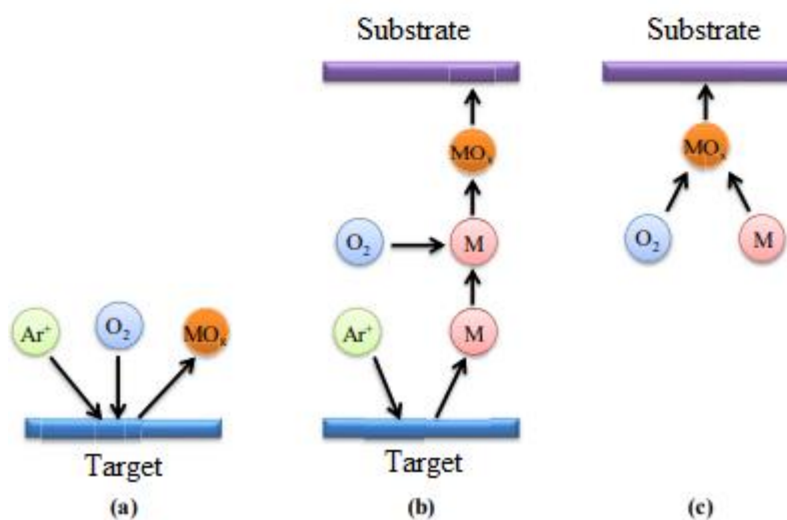

Figure 2.8. Three reaction mechanisms between the reactive gas and the target atoms during a sputtering deposition under reactive conditions (O_2 is an example of a reactive gas, and M symbolizes the metal atom from the target.) [50]

The target's surface becomes contaminated because of the reaction between its atoms and the oxygen, eventually generating an insulating layer that can cause instability issues. Electrical instability is the primary issue that is frequently faced. Positive charges build up on the surface of dielectric films during reactive sputtering up until the breakdown voltage. Thus, micro-arcs form on the target surface in the regions covered by the non-conductive material, which causes

the ejection of particles that may worsen coating quality or, more seriously, may harm the generator irreparably. Using a pulsed medium frequency direct current is a widely used method to prevent electrical instability [51]. Figure 2.9 illustrates the procedure of this idea. Positive charges build up on the surface of the target's contaminated regions during the negative polarization period (ton). The electrons near the target neutralize the positive charges on the surface and in the contaminated areas during the discharge halt (toff). A total of ten microseconds pass until the discharge is complete. This equates to an average frequency of around 50 kHz to prevent electrical instability [52].

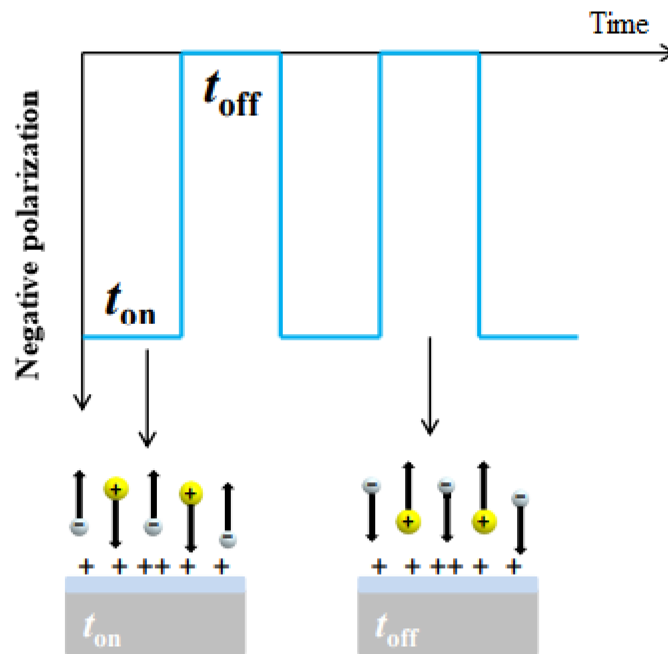

Figure 2.9. An illustration of a medium frequency pulsed DC generator signal [52]

Hysteresis is another issue that has been identified with the reactive sputtering regime. As the reactive gas flow rate rises, the deposition rate falls because the compound's sputtering efficiency is often lower than that of the metal target. A non-linear relationship exists between the rate of deposition and the flow rate of reactive gases, as well as between the composition of the film and the flow rate of reactive gases.

2.9 High Power Impulse Magnetron Sputtering

The material to be sprayed receives the energy of the ions that are affecting the target more or less directly in the form of heat. This explains why the heat dissipation characteristics of conventional sputtering limit the power applied. Each power source, then, affects the plasma.

A negative voltage is often delivered by a continuous source (DC), and it remains constant over time. However, a more recent power supply has been studied and used.

This power supply is unique in that it can instantaneously produce power that is two or even three orders of magnitude greater than that of a standard DC power supply for a very brief period and at a specific frequency (100 Hz to 3 kHz). This technique creates a very high density of electrons and ions while avoiding the cathode's heating. However, the overall power or average power is strictly equivalent to the conventional DC. High Power Impulse Magnetron Sputtering, or HiPIMS, is what it is called.

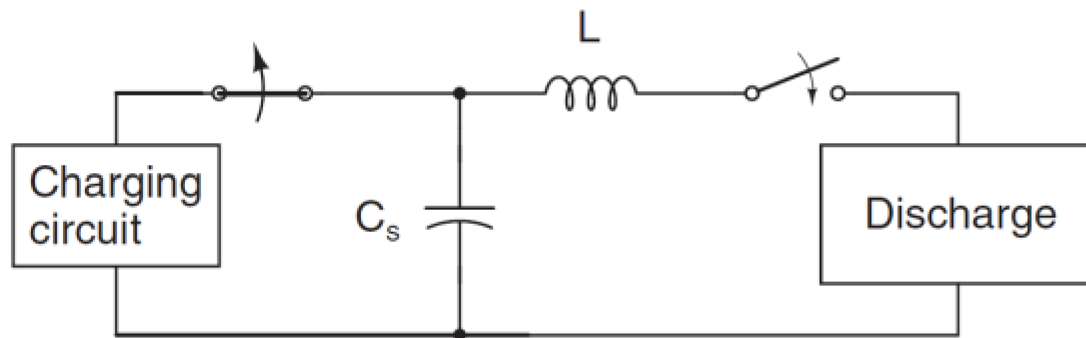

Figure 2.10. Simple LC circuit constituting the artificial network for creating HiPIMS pulses [53]

The HiPIMS generators, as shown in Figure 2.10, are essentially made up of an LC circuit that runs repeatedly. As a result, the generated pulses have power peaks that can approach megawatts or beyond and have an appearance similar to the charge-discharge of capacitors. With a repetition frequency, these high-power discharges are produced for only a brief period of time (20 to 200 s).

Researchers have been very interested in studying highly ionized plasmas produced by high-power pulsed current power supply over the past few years. It is now possible to produce an extremely dense plasma with a high level of sputtered species ionization. Kouznetsov et al. [53] were the first to achieve results in 1999.

They specifically note an increase in the uniformity of the thickness of the deposits in comparison to that achieved by conventional magnetron sputtering since the race track is larger than typically reported for planar circular magnetron sputtering with a stationary magnet assembly.

HiPIMS also makes it possible to get around this restriction by using a significant amount of power on the target for only a few tens of microseconds. On the other hand, because the frequencies rarely go above 1 to 2 kHz, the duty cycle is low. While maintaining an average power similar to that used by traditional magnetron sputtering, the power so created can quickly reach a few kilowatts per unit of the area without harming either the target material or the magnets.

A HiPIMS pulse can typically be divided into two parts. The cathode receives the voltage injection and the peak plasma intensity during the first phase of the pulse, which is known as the active phase and is specified as time ON.

The second is designated as the inactive phase since no voltage is applied to the cathode during the second phase, it is known as time OFF. As a result, the plasma is kept in place thanks to the density of energetic particles that were produced during the first phase. Nevertheless, because high powers are being used, it is vital to restrict cathode heating. The duty cycle is thus established and represents the proportion of ON time to total time. It is kept low, for this reason, allowing for the attainment of average powers comparable to DC discharges. A typical illustration of the voltage and current characteristics for a high-power impulsive magnetron discharge is shown in Figure 2.11 [54]. The applied voltage ranges from 500 to 1000 V most of the time, and the maximum discharge current density is only a few amps per square centimeter.

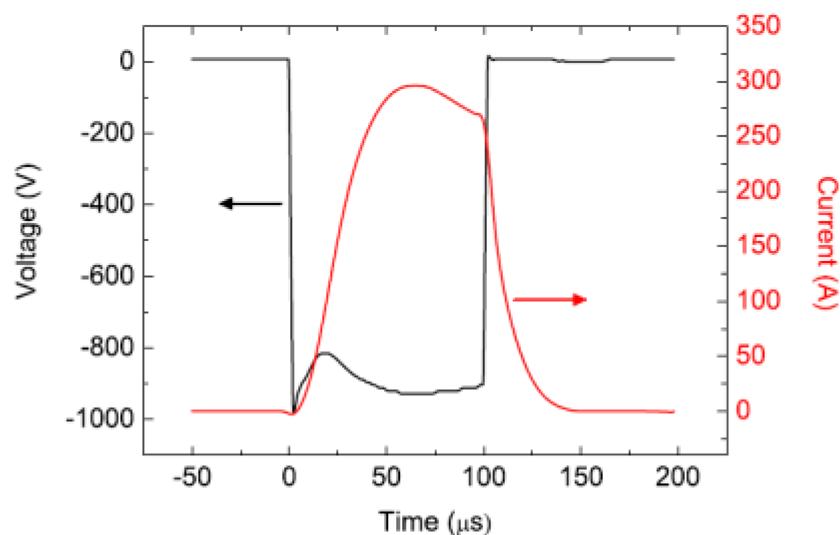

Figure 2.11. Characteristics of voltage and current for a typical HiPIMS discharge [54]

2.9.1 Advantages of HiPIMS

One of the most intriguing aspects of this technique is the ability to create a luminous discharge during brief pulse periods with noticeable power peaks. This method also makes it possible to produce highly ionized plasma.

Numerous studies on HiPIMS have demonstrated the value and benefits of this method. For example, Ehiasarian et al. [55] investigated how the HiPIMS discharges affected the makeup of a Ti/Ar plasma. To compare the outcomes of the two methods, they used a radio frequency (RF) coil and a conventional magnetron sputtering at an average power of 300 W each. The reported highest peak power for the HiPIMS discharge was 1.5 $kW.cm^{-2}$. They also observed the ratio between the spectral line of excited titanium and that of ionized titanium using optical emission spectroscopy (OES) (and for the case of chromium). The best metal ion content was obtained with the HiPIMS discharge, which had a value of 5. As a result, this ratio is negligible in DC with a value of 0.9.

Moreover, Bohlmark et al. analyzed the energy distribution of ionized metal species created during a HIPIMS discharge from a titanium target. They measured energies reaching 100 eV for Ti+ ions, and 50% of the metal ions have an energy greater than 20 eV. In addition, they observed that the ionic flux is composed of approximately 50% of Ti+, 24% of Ti2+, 23% of Ar+, and 3% of Ar2+ during the most intense peak of the discharge. These results are higher than the ones of a DC (direct current) discharge, about 35% of Ti+, 15% of Ti2+, 49% of Ar+, and 1% of Ar2+ . In all of these studies, we can see that HiPIMS offers the possibility of generating highly ionized plasmas with highly energetic species.

This technique will promote the control of ion bombardment by applying a bias voltage to the substrates. Thus, the efficiency of ion stripping and therefore the adhesion of thin films can be considerably improved [56].

2.9.2 Disadvantages of HiPIMS

The poor deposition rate compared to traditional magnetron sputtering is the drawback of the HiPIMS method. On average, for equivalent mean powers, a reduction in the deposition rate of 70–75% is seen. This decrease can be explained by different things.

The plasma is turned on approximately 90% of the time in DC discharges (pulse of about 5 µs over a period of 20 µs for F = 50 kHz), while in HIPIMS discharges, it is the reverse (pulse of 5 µs over a period of 2 ms for F = 500 Hz). There is also the self-sputtering process; the ions

produced by collision in the plasma are re-attracted by the strong negative voltage applied to the target. Therefore, they no longer reach the samples in sufficient quantity, and consequently the sputtering efficiency decreases [57]. Plus, the confinement of the plasma to the surface of the target has an influence. This deficiency can be obtained by optimizing the magnetic confinement.

2.10 The sputtering practical steps

In order to achieve better deposition, it is important to know all the steps of the reactor equipment process, considering what takes place inside the vacuum chamber during the disposition cycle.

A preparation process before the deposition is required, cleaning the substrate performs greater adhesion of the film, so the cleaning of substrates in an ultrasonic bath outside the vacuum chamber is also suggested before their placement [58], an important parameter share in the optimization is the deposition rate which can be regarded in terms of improving the plasma density and the available energy in the process. Therefore, it is necessary to consider all the steps and the parameters being studied to comply with the industry demands. [59]

To obtain a great sputtering, it is necessary to go through the steps shown on the following figure:

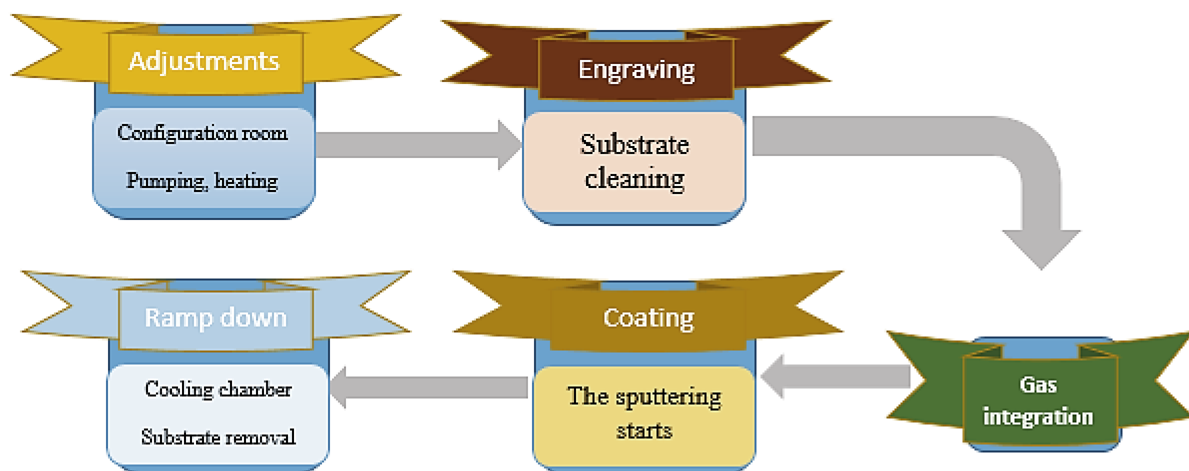

Figu 2.12. Treatment steps to follow in a classic sputtering

-First step (the adjustment): consists of the preparation of the vacuum chamber, which is composed of a gradual increase in temperature created by tubular heating and a modular control system. At the same time, the vacuum pumps are activated to reduce the pressure inside the

chamber, for that, two pumps are used, the first producing a pressure of up to 10^{-5} bar, and the second (high vacuum) producing a pressure of 10^{-7} bar.

-Second step (engraving): is characterized by cathode cleaning, where the substrate is bombarded with ions from plasma etching to clean up localized contamination on the substrate surface. This is an important step to do before starting sputtering because it helps to increase adherence.

-Third step (gas integration): before starting we have to integrate a gas that aims to bombard our target, several gas choices are available like argon xenon and so on, the choice of gas is very important as it contributes to the sputtering efficiency.

-In the fourth step (coating) takes place: the sputtering process can be started, and the material to be deposited is projected onto the substrate surface.

-final step (ramp down): corresponds to the cooling of the chamber, and the return of the vacuum chamber to room temperature and ambient pressure. To achieve this, a specific cooling system must be applied. [60, 61]

Chapter 3
Numerical simulations of the sputtering process

3.1 Introduction

Today, numerical simulations are frequently used to describe and forecast the discharge phenomena present in a process to improve it. As a result, it enables the determination of parameters for a magnetron sputtering discharge, such as the electric potential, the plasma density in non-reactive or in reactive gas, the charged particle densities, temperatures, and energy distributions with a magnetic field present. To simulate a magnetron discharge, various models have been created. The most popular approach to study the sputtering phenomena is Monte Carlo simulation, since the process is atomic, indeed the Monte Carlo simulation is a powerful tool that allows us to obtain the dynamics properties of a solid, liquid, or gas system and can give you a result of atomic deposition.

3.2 Numerical simulations of magnetron sputtering

Numerical simulations are now widely used thanks to improvements in computer performance. Researchers are using numerical simulations more and more to support and explain experimental findings. Characterizing discharges and predicting system behavior are two other benefits of employing numerical simulations. It enables process optimization and, as a result, lowers the cost of design experiments. It is interesting to simulate entirely due to the significant use of magnetron sputtering in businesses nowadays for the creation of thin films. [62]

The modeling of the magnetic field, magnetron discharge, particle-target interaction, and sputtering, transport of sputtered particles through the gas phase, deposition, and film growth at the substrate are all included in a complete simulation of magnetron sputtering, according to Bogaerts and coworkers. Finally, this results in models for the processes of sputtering erosion and deposition.

To understand the physical processes involved in the system, numerous models in 1D, 2D, and 3D have been developed [63]. The next subsections present the various techniques used to model the magnetron discharge and sputtering erosion.

3.2.1 Monte Carlo simulation Method

A Monte Carlo simulation is used to model the probability of various outcomes in a process that is difficult to predict because of the involvement of random variables. It is a method for understanding how risk and uncertainty will affect a situation.

History: Due to the importance of chance and random results in this modeling method, the Monte Carlo simulation was called after the famous gambling resort in Monaco.

The method was initially created by mathematician Stanislaw Ulam, who participated in the Manhattan Project, a covert endeavor to construct the first atomic weapon. He shared the idea to his Manhattan Project coworker John Von Neumann, and the two worked together to improve the Monte Carlo simulation. [64]

3.2.1.1 Understanding the Monte Carlo Simulation

Some techniques substitute the uncertain variable with a single average number when there is a large amount of uncertainty in the forecast or estimate. Instead, the Monte Carlo Simulation averages the findings from several values.

Numerous industries, including business and, investing, that deal with random variables can benefit from Monte Carlo simulations. They are employed to calculate the possibility of cost overruns in significant projects and the propensity for a particular asset price movement.

They are used by telecoms to evaluate network performance in various scenarios, which aids in network optimization. They are used by financial analysts to evaluate the likelihood that a firm would default and to examine derivatives like options. They are also used to assess risk by oil well drillers and insurers. In fields other than business and finance, such as meteorology, astronomy, and particle physics, Monte Carlo simulations are used extensively.

The problem with any simulation technique, as the Monte Carlo method admits, is that random variable interference makes it difficult to pinpoint the likelihood of different outcomes. Because of this, a Monte Carlo simulation concentrates on repeatedly repeating random samples.

The variable with uncertainty is given a random value through a Monte Carlo simulation. The model is then run, and a conclusion is given. While giving the variable in question a wide range of values, this process is repeatedly performed. After the simulation is finished, the outcomes are averaged to get an estimate. [65]

3.2.1.2 Benefits and Drawbacks of Monte Carlo Simulations

An investor can evaluate the probability of a gain or loss on a certain investment using the Monte Carlo approach. The goal is the same for other approaches.

The Monte Carlo simulation was developed to address a perceived drawback of earlier techniques for determining a likely course of action.

No simulation can predict a certain result. The probability that an outcome may deviate from a projection is better estimated using the Monte Carlo approach.

The distinction is that, as opposed to beginning with an average, the Monte Carlo method first evaluates a number of random variables before averaging them.

The Monte Carlo approach, like any financial simulation, bases its estimate of future price data on historical price data. The pattern is subsequently broken by the addition of illogical, numerical variables. The risk that the pattern will be broken in reality is then estimated by averaging these statistics.

3.2.2 The magnetron sputtering discharge

Numerous investigations into the magnetron sputtering discharge have been made in order to establish the fundamental plasma properties [66]. The study of the electric potential, the plasma density with non-reactive or reactive gas made of neutrals and charged particle densities, temperatures, and energy distributions in a magnetic field are all included in the simulation of magnetron discharge. The magnetron sputtering discharge was modeled using a variety of techniques, including fluid, kinetic, particle, and hybrid approaches.

3.2.3 Magnetic field

Based on the equation of magnetic flux conservation, analytical and numerical methods are utilized to predict the distribution of the magnetic field [67, 68]. According to Kondo and Nanbu's work, the magnetic field in permanent magnets is described by:

$$B = \mu_0 H + M \quad (3.1)$$

Where B is the magnetic flux density, H is the magnetic field, M is the magnetization and μ_0 is the permeability of free space.

Permanent magnets have the following governing equation:

$$\frac{1}{\mu_0} \nabla \times B = j_m \quad (3.2)$$

Where j_m is the magnetizing current.

$$\frac{1}{\mu_0} \nabla \times M = j_m \quad (3.3)$$

Since $\nabla . B = 0$, the vector potential A can be introduced as:

$$B = \nabla \times A \text{ (3.2)} \quad (3.4)$$

The governing equation can finally be expressed as:

$$\frac{1}{\mu_0} \nabla \times (\nabla \times A) = j_m \quad (3.5)$$

3.2.4 The Particle-In-Cell/Monte Carlo Collision (PIC/MCC)

The most typical method to model a magnetron discharge is the Particle-In-Cell/Monte Carlo Collision (PIC/MCC).

This particle method treats each individual particle as an ensemble of macro particles, which can be an electron, an ion, or a neutral. These macro particles' trajectories are computed using Newton's equations for the magnetic, electric, and Poisson's equation-solved fields. The Monte Carlo (MC) method is used to describe particle collisions [69].

The equation of motion of charged particles is given by [70, 71]:

$$m \frac{dv}{dt} = q(E + v \times B) \quad (3.6)$$

Where m is the mass, v is the velocity, t is the time, q is the charge, E, and B represent respectively the electric field and the magnetic field.

Poisson's equation is solved to obtain the electric field:

$$\nabla^2 \phi = -\frac{\rho}{\epsilon_0} \quad (3.7)$$

$$E = -\nabla \phi \quad (3.8)$$

Where ρ is the charge density and ϵ_0 is the permittivity of free space.

Whether or not a collision happens may affect the velocity and position. As a result, assuming argon as the background gas, the collisions between an electron and an argon atom (e^-- Ar), including ionizing, elastic, and exciting collisions, as well as the collisions between an argon ion and an argon atom (Ar^+ -Ar), including elastic collision and resonant charge exchange, are taken into account.

Then, the probability that the (e^- -Ar) collision occurs is given by:

$$P_e(k) = N_A \sigma_k(\varepsilon) \left(\frac{2\varepsilon}{m_e}\right)^{1/2} \Delta t_e \tag{3.9}$$

Where k is the number of the event, Δt_e is the electron time step, N_A is the number density of argon gas, σ_k is the (e^--Ar) collision cross-section, ε is the electron's energy and m_e is the electron mass.

The probability of Ar^+ -Ar collisions is given by:

$$P_i = 4\pi\beta_\infty^2 \left(\frac{a}{M_A}\right)^{1/2} N_A \Delta t_i \tag{3.10}$$

Where Δt_i is the ion time step, β_∞ is the cut-off of the dimensionless impact parameter, M_A is the ion mass and $a = \alpha_d e^2/(32\pi^2\epsilon_0^2)$ where α_d is the polarizability and is the electronic charge.

PIC/MCC has run numerous magnetron discharge models in 1D, 2D, and 3D. Van der Straaten and colleagues created a 1D model of a DC cylindrical post-cathode magnetron discharge, as is common practice. Nanbu and Kondo have researched the 3D and 2D axisymmetric models of a DC planar magnetron discharge In works by Shon and Lee [72], plasma density and potential distribution PIC/MCC simulations have also been integrated with kinetic simulations to obtain particle velocity information for erosion and deposition.

However, the statistical component of MC necessitates the treatment of many particles, which implies a substantial amount of calculation time and computer memory allocation.

3.2.5 Kinetic approach

The kinetic model is based on solving Boltzmann's equation to ascertain the particle distribution functions. [73, 74]

By resolving Boltzmann's equation for the Electron Energy Distribution Function (EEDF) in the magnetized portion of the discharge, Guimares and associates created a DC planar magnetron discharge, written as:

$$\frac{\partial n(\varepsilon,t)}{\partial t} = -\left[\frac{\partial J_{el}}{\partial \varepsilon}\right]_{e-A} + \left[\frac{\partial J_{el}}{\partial \varepsilon}\right]_{e-e} + J_{exc} + J_{ion} + S + L + P \tag{3.11}$$

Where $n(\varepsilon, t)d\varepsilon$ is the number density of electrons having an energy in the range $[\varepsilon, \varepsilon + d\varepsilon]$, t is the time, $\left[\frac{\partial J_{el}}{\partial \varepsilon}\right]_{e-A}$ and $\left[\frac{\partial J_{el}}{\partial \varepsilon}\right]_{e-e}$ correspond respectively to the elastic electron-atom (or electron-molecule) and electron-electron Coulomb collisions, J_{exc} and J_{ion} correspond

respectively to the inelastic and ionization collisions, S is the source term, L is the loss term and P takes account of Penning electrons. The term $S(\varepsilon)$ corresponds to the averaged density number of electrons, which leave the cathode and enter in the glow, over the magnetized volume

Plasma properties like the current, voltage and gas pressure affect the Electron Energy Distribution Function (EEDF). Calculating ionization and excitation frequencies is possible thanks to its solution. For an argon plasma, this kinetic model was additionally connected with a Collisional-Radiative (CR) by:

$$\frac{dn_i}{dt} = \sum_{j\neq i} n_e n_j C_{ji}^e + \sum_{j>i} n_j A_{ji} - n_i \left[n_e \sum_{j\neq i} C_{ij}^e + n_e C_i^e + \sum_{j<i} A_{ij} + k_p \sum_j n_j + \frac{D_i}{\Lambda^2} \right] \quad (3.12)$$

Where n_i is the density of state i , n_j is the density of state j , n_e is the electron density at time t , C_{ji}^e is the inelastic (or superelastic) electronic collision rate for transition $j \rightarrow i$ (also calculate at time t), C_i^e is the ionization rate for state i , A_{ij} is the transition probability from state i to state j , D_i is the diffusion coefficient for the state i and Λ is the characteristic diffusion length defined by:

$$\Lambda = \left[\frac{\pi^2}{h^2} + \left(\frac{2.405}{R} \right)^2 \right]^{-1/2} \quad (3.13)$$

Where the associate geometry of metastable is approximated to a disc of a radius R and a height h.

$$k_p = 6.4 \times 10^{-10} \times \left(T_g / T_0 \right)^2 \quad (3.14)$$

Where T_g and T_0 are the actual gas temperature and the ambient temperature of 300 K respectively.

3.2.6 The fluid model

Boltzmann's equation, continuity, momentum transfer, and mean energy transfer are all used in the fluid model to describe the transport of charged particles and neutrals [75]:

$$\frac{\partial n_s}{\partial t} + \nabla \cdot \overrightarrow{\Gamma_s} = S_s \quad (3.15)$$

$$m_s n_s \left[\frac{\partial \overrightarrow{v_s}}{\partial t} + (\overrightarrow{v_s} \cdot \nabla) \overrightarrow{v_s} \right] = q_s n_s \left(\vec{E} + \overrightarrow{v_s} \times \vec{B} \right) - \nabla \overrightarrow{P_0} - m_s n_s f_{ms} \overrightarrow{v_s} \left(1 + \frac{S_s}{n_s f_{ms}} \right) \quad (3.16)$$

$$\frac{\partial (n_s \varepsilon_s)}{\partial t} + \nabla \cdot \overrightarrow{\Gamma_{\varepsilon s}} = -\overrightarrow{\Gamma_s} \cdot \vec{E} - \theta_s n_s \quad (3.17)$$

$$\Delta V = -\frac{e}{\varepsilon_0}(n_i - n_e) \tag{3.18}$$

Where s is the type of particle ($s = e$ for electron and ion), n_s is the density, t is time, $\overrightarrow{\Gamma_s}$ is the particles flux, $\overrightarrow{v_s}$ is the velocity, s_s is the source term, m_s is the mass, q_s is the particle charge, $\vec{E}$ is the electric field, $\vec{B}$ is the magnetic field, $\overrightarrow{P_0}$ is the pressure tensor, f_{ms} is the total momentum transfer frequency for specie s-neutral collisions, ε_s is the mean energy, $\overrightarrow{\Gamma_{\varepsilon s}}$ is the energy flux, θ_s is the energy loss rate for s-neutral collisions, V is the electric potential, e is the constants of elementary charge and ε_0 is the permittivity of free space.

In contrast to the particle approach, this method requires less calculation time because electrons and ions are treated as two fluids. Bradley and Lister's fluid technique was used in studies to treat the magnetron discharge in 1D. Costin and colleagues also created a 2D axisymmetric model of a DC planar magnetron discharge [76]. However, researchers do not typically use Computational Fluid Dynamics (CFD) to simulate a magnetron discharge. This can be explained by the impact of charged particles on an inhomogeneous and powerful magnetic field. Due to an assumption that must be taken into consideration for fluid application, it is also restricted for low-pressure magnetron sputtering discharge modeling. When the discharge characteristic length is surpassed by the mean free path of charged particles at low pressures, the fluid model is invalid [77]. Even though the magnetron discharge operates at low pressures, the introduction of a magnetic field minimizes the effective distance that electrons must travel between two collisions and, in some circumstances, permits the hydrodynamic hypothesis to be fulfilled.

3.2.7 The hybrid model

The hybrid model, which is created by combining particle and fluid techniques, generates numerous models. Naturally, the primary motivation for using a hybrid model to simulate a magnetron sputtering discharge is to minimize the computation time limitations associated with the PIC/MCC technique. In fact, because PIC/MCC is frequently used to describe non-equilibrium processes, hybrid models are carried out by treating fast electrons in one part of the model using particle theory in order to obtain individual movement of highly non-equilibrium electron expression, and ions and bulk electrons in the other part of the model to calculate the spatial distribution of charged particles. This approach has been described in the hybrid models of Kolev and Bogaerts [87], Shidoji and coworkers, and others. Another approach is to use a hybrid model of a magnetron discharge, such as the one studied by Shidoji and Makabe,

followed by Jimenez, Kageyama, and their associates [78, 79], in which all the electrons are addressed by the particle model and all the ions by the fluid model.

3.3 The Sputtering Phenomena

The sputtering phenomena depend on the target's chemical and physical composition, as well as the discharge parameters. Depending on the nature of the materials in question, particles such as energetic ions, recoil atoms, electrons, and photons can erode the surfaces of materials (metal, ceramic, polymers, ...). In order to explore factors including ion energy, ion dose, ion-target combination, target temperature, and target structure, sputtering studies have been carried out with various geometries. The majority of them were based on various sputtering yield measurement techniques. The ratio of the number of sputtered atoms from the target surface to the number of incident particles, in this case, the ions, is known as the sputtering yield.

Sputtering was described by Stark as a series of binary collision events caused by one sputtering ion at a time, which was one of many explanations regarding the cause of sputter erosion [80, 81]. Sputtering was thus defined as an elastic collision process involving a single collision followed by a series of collisions that result in a cascade of moving target atoms. A linear cascade or a spike are two possible outcomes for the many collisions cascade. Finally, as shown by Sigmund and depicted in Figure (3.1), this results in various situations of sputtering occurrences. The single-knock-on regime, the low-density linear cascade, and the high-density spike cascade are the three sputtering scenarios in this setting [82, 83]. Target atoms that get enough energy from sputtering ions to overcome the surface binding forces are ejected under the single-knock-on regime. The recoil atoms receive enough energy during a cascade of

collisions to produce secondary and higher-generation recoils. When a recoiling atom's energy approaches the lattice binding energy, the remaining kinetic energy is converted into heat, which is what distinguishes the linear cascade. The spike cascade establishes when, in contrast, the cascade is so dense that the chance of striking a moving target atom is low.

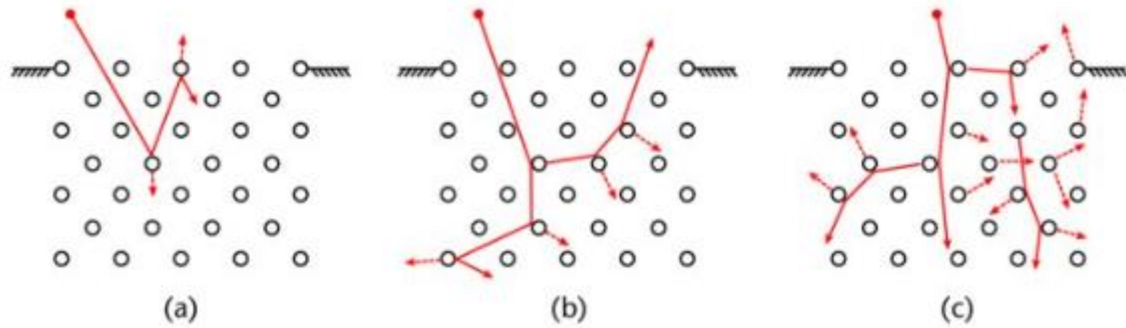

Figure 3.1. Three regimes of sputtering induced by elastic collisions [84].

From the figure (3.1), (a) is the Single knock-on: Recoil atoms receive sufficient energy to be sputtered, but not enough to induce collision cascades. (b) Linear cascade: Sufficient energy is gained by the recoil atoms for a linear collision cascade to occur. The density of recoil atoms is low enough for binary collisions to dominate, and collisions between moving atoms are infrequent. (c) Spike: The density of recoil atoms is so high that the majority of atoms within a local volume (the spike volume) are in motion.

The explanation of the sputtering process is based on the theory of collision cascades in nonlinear and linear regimes. A linear cascade sputtering transport theory was made possible by the works of Sigmund and Thompson [84].

The sputtering yield estimate is the primary factor that distinguishes the sputtering erosion of a surface material [85]. Additionally, this parameter can be estimated with reasonable precision using the linear collision cascade. In order to simulate the two sputtering regimes and determine yields within the context of the linear collision cascade theory, numerical models of the Binary Collision Approximation (BCA) and Molecular Dynamics (MD) models have been constructed.

3.3.1 Binary collision approximation

The BCA approach involves simulating an atomic collision that occurs during a sputtering cascade in a solid material. This radiation damage is simulated by a sequence of separate binary collisions between two particles—an incident ion and a target atom that is at rest. In BCA, the conservation of energy and momentum is used to calculate the energy lost by the moving ion and the energy transferred to the recoil atom, and the conservation of angular momentum is used to calculate the scattering angles of the moving ion and the recoil atom [86]. Eckstein and Urbassek's formula for the scattering angle in the center-of-mass system is as follows:

$$\theta = \pi - 2p \int_R^{\infty} \left[r^2 / \sqrt{1 - \frac{V(r)}{E} - \frac{p^2}{r^2}} \right] dr \tag{3.19}$$

Where p is the impact parameter, $V(r)$ is the interaction potential, E is the kinetic energy of the moving atom, r is the distance between the two colliding atoms and R is the apsis (closest distance) of the collision calculated from [87]:

$$1 - \frac{V(R)}{E_C} - \left(\frac{p}{R}\right)^2 = 0$$

With E_C is the center-of-mass energy given by:

$$E_c = \frac{m_b}{m_a + m_b} E$$

Where m_a and m_b are respectively the incident ion and the target atom masses, E is the moving atom kinetic energy.

The energy transmitted to the recoil atom is determined by the ion's scattering by:

$$T = 4 \frac{m_a m_b E}{(m_a + m_b)^2} \sin^2 \frac{\theta}{2} \tag{3.20}$$

Utilizing the simple MC technique, various algorithms based on the binary collision approximation have been created, including MARLOWE, ACAT (Atomic Collisions in Amorphous Targets), and TRIM (Transport of Ions in Matter).

Both a random target and a crystalline target can simulate atomic collisions in a linear cascade thanks to MARLOWE. ACAT can handle atomic collisions in an amorphous target. Atomic collision in random targets is treated in TRIM simulations [88, 89]. The potential many-body effects that could happen in the cascade were disregarded in these algorithms. Then, using dynamical Monte Carlo, programs were altered to better the simulation of the sputtering collision cascade and subsequently to account for the effects caused by collisions. ACOCT is one of them, which studies atomic collisions in monocrystalline targets and is a variation of the ACAT code that differs only in the collision procedure. DYACAT, which uses a nonlinear MC code comparable to ACAT in a dynamical mode, is the DYnamical Simulation of Atomic Collisions in a Crystalline Target [90]. The dynamic mode in this code takes into account many-body collisions between a moving particle and a number of the target atoms. TRIM.SP, which treats atomic collision in amorphous targets and permits the following of recoil atoms and ions, is also the sputtering variant of TRIM. The TRIDYN code, which is a dynamic adaptation of

TRIM, considers the impact of collisions and target modifications. Additionally, SDTrimSP, which stands for StaticDynamic, was created to enhance TRIDYN [91].

These Monte Carlo programs, which are based on the binary collision approximation, are well recognized for being quick and enabling simulations of the sputtering cascade in large spaces and timescales.

3.3.2 The molecular dynamics

For describing plasma-surface interactions, molecular dynamics is an effective method. As a result, it enables the simulation of both linear and nonlinear sputtering collision cascades. The collisions between incident particles and a system of particles are handled in time evolution using classical mechanics, in contrast to the MC technique in the binary collision approximation. The system can be examined at time scales ranging from femtoseconds to nanoseconds, and occasionally even microseconds.

In order to simulate the dynamics of a system of particles, the molecular dynamics approach involves solving Newton's equations of motion for each particle [92, 93]:

$$\vec{F_l} = m_i \vec{a_l} = m_i \frac{d\vec{v_l}}{dt} = m_i \frac{d^2\vec{r_l}}{dt^2} \tag{3.21}$$

Where $\vec{F_l}$ is the force applied on atom i exerted by some external agent, m_i is the mass of the atom, $\vec{a_l}$ is the acceleration, $\vec{v_l}$ is the velocity and $\vec{r_l}$ is the position.

In sputtering, ions are released toward the target surface with a velocity corresponding to the energy obtained from the target bias voltage and impact the target. Then, the velocities and accelerations of the particles are obtained from forces applied on atoms and give new particle positions. These forces are specified from interatomic potential [94].

3.3.3 The sputtering yield

A material's erosion by ions bombardment can be calculated from the sputtering yield stated in the literature by S or Y. The quantity of sputtered atoms from the target surface to incident ions, expressed as a ratio, is the sputtering yield. Therefore, the yield is expressed here by Behrisch and Eckstein as:

$$Y = \frac{number\ of\ atoms\ ejected}{number\ of\ incident\ ions} \tag{3.22}$$

Sputtering measurement can be done according to three categories, as presented by Thompson [95], such as the yield S, the distribution in direction of the sputtered atoms $\frac{dS}{d\Omega}$ and the distribution of energy and direction $\frac{d^2S}{d\Omega dE}$ described by the differentials of sputtering yield. These parameters allow us to obtain information on the deposition velocity and the growing film [96].

The change in the yield is then influenced by the energy, angle of incidence, and ion atomic number. Sigmund created a sputtering yield formula from the theory of collision cascade by resolving the linearized Boltzmann equation. Sigmund, therefore, describes the sputtering yield as a series of steps that include figuring out how much energy is deposited by the particles close to the surface, converting that energy into a number of low-energy recoil atoms, figuring out how many of these recoil atoms reach the surface and then choosing atoms with enough energy to overcome the surface's binding forces. The parameters of the cross sections for high-energy ions and atoms, as well as atoms with low energy scattering and surface binding forces, can be used to describe these many processes in the formulation of sputtering yield.

3.3.4 Sigmund formula

Sigmund thus provides the sputtering yield at perpendicular incidence:

$$S(E) = 0.0420\alpha S_n(E)/U_0 \text{Å}^2 \tag{3.23}$$

Where the factor α is a function of mass ratio in the elastic collision region, U_0 is the height of the surface potential, $S_n(E)$is the elastic stopping power.

$S_n(E)$ is expressed from Lindhard and calculated by assuming the Thomas-Fermi interaction:

$$S_n(E) = 4\pi Z_1 Z_2 e^2 a_{12}[M_1/(M_1 + M_2)]s_n(\epsilon)$$

Where ϵ is the reduced energy:

$$\epsilon = \frac{M_2 E/(M_1+M_2)}{Z_1 Z_2 e^2/a_{12}},$$

Z_1 and Z_2 are atomic number of incident particle and target atom respectively, M_1 and M_2 are atomic masses of the incident particle and target atom respectively, a_{12} is the Thomas-Fermi screening radii:

$$a_{12} = 0.8853a_0\left(Z_1^{2/3} + Z_2^{2/3}\right)^{-1/2},$$

$s_n(\epsilon)$ is the universal function of reduced nuclear stopping cross-section and a_0 is the Bohr radius.

Sputtering yield formulas of energy dependence at perpendicular incidence have been expressed based on the original formula from Sigmund.

3.3.5 Bohdansky formula

With MARLOWE and TRIM calculations, Bohdansky presented the following formula for total sputtering yield at normal incidence for light and heavy ions above the threshold regime [120]:

$$Y(E) = \frac{0.042}{U_0}\left(R_p/R\right)\alpha S_n(E)\left[1-(E_{th}/E)^{2/3}\right] \times \left[1-(E_{th}/E)\right]^2 \tag{3.24}$$

where E is the energy of the primary particle, U_0 is the surface binding energy, R is the average path length, R_p is the projected range, α is the energy-independent function of the mass ratio between the target atom and the incident particle, S_n is the nuclear stopping cross-section and E_{th} is the threshold energy [97].

The determination of the threshold energy must follow the condition $E_{th} + E_{sp} > E_{sb}/\gamma$ with E_{sp} the binding energy of the incident particle to the target surface, E_{sb} the surface binding energy and $\gamma = 4M_1M_2/(M_1+M_2)^2$ the binary collision energy transfer factor.

3.3.6 Yamamura formula

Matsunami and colleagues came up with a simple empirical formula:

$$Y(E) = 0.042\frac{\alpha(M_2/M_1)}{U_s}S_n(E)\left[1-(E_{th}/E)^{1/2}\right] \tag{3.25}$$

Where E is the incident particle energy, E_{th} is the threshold energy, α is the function of the mass ratio between the target atom and the incident particle, U_s is the surface binding energy and $S_n(E)$ is the nuclear stopping cross-section.

From this formula, Yamamura developed an expression which describes the angular distribution of sputtered atoms by taking into account an anisotropic velocity distribution given by:

$$S(E,\theta,E_0,\theta_0) = 0.042\frac{\alpha(M_2/M_1,\theta)S_n(E)}{U_s} \times \left[1-\frac{1}{2}(E_{th}/E)^{1/2} \times \left\{\cos\theta\gamma(\theta_1) + \frac{3}{4}\pi\sin\theta\sin\theta_1\cos\phi\right\}\right] \tag{3.26}$$

Where

$$\gamma(\theta_1) = \frac{3\sin^2\theta_1 - 1}{\sin^2\theta_1} + \frac{\cos^2\theta_1(3\sin^2\theta_1 + 1)}{2\sin^3\theta_1} \times \ln\left(\frac{1+\sin\theta_1}{1-\sin\theta_1}\right),$$

θ and θ_1 are angles of incidence, and is a scattering angles. The threshold energy E_{th} is determined by:

$$E_{th} = \frac{4U_s}{\gamma} \ ,$$

The angle distributions estimated by Yamamura for Ni sputtered atoms by Hg ions impacting at normal incidence for various energies are shown in (Figure 3.2) below. The results were compared with experimental findings from Wehner [98].

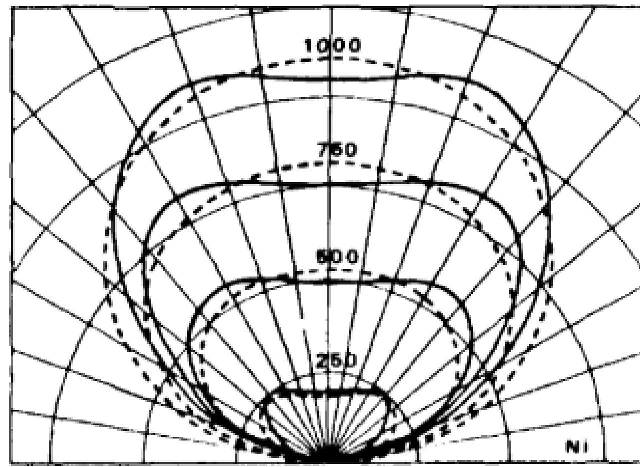

Figure 3.2. Angular distributions of sputtered atoms from Ni by normally incident Hg+ ions, calculated results from last Eq [98]

Then, Yamamura developed a new empirical formula:

$$Y(E) = 0.042\frac{Q(Z_2)\alpha^*(M_2/M_1)}{U_s}\frac{S_n(E)}{1+\Gamma k_e \epsilon^{0.3}} \times \left[1 - \sqrt{\frac{E_{th}}{E}}\right]^S \tag{3.27}$$

Where Q is a fit parameter that includes the effect of the electronic stopping, Z_2 is the atomic number of the target atom, α^* is the function of the mass ratio M_2/M_1 :

$$\alpha^* = 0.249(M_2/M_1)^{0.56} + 0.0035(M_2/M_1)^{1.5} \qquad M_1 \leq M_2$$

$$= 0.0875(M_2/M_1)^{-015} + 0.165(M_2/M_1) \qquad M_1 \geq M_2,$$

k_e is the Lindhard electronic stopping coefficient, ϵ is the reduced energy:

$$\epsilon = E\frac{M_1}{M_1+M_2}\frac{a_L}{Z_1 Z_2 e^2} \ ,$$

Γ is a factor:

$$\Gamma = \frac{W(Z_2)}{1+(M_1/7)^3} \ ,$$

$Q(Z_2)$ and $W(Z_2)$ are parameters defined by using the Ziegler-Biersack-Littmark (ZBL) repulsive potential in Yamamura and Tawara [99] and S is the power equal to 2.8 by using the power approximation of $m = 1$ which corresponds to Rutherford scattering.

3.3.7 Eckstein formula

Additionally, Eckstein and Preuss presented the following fit formula for the sputtering yield at normal incidence with TRIM.SP is given by [100]:

$$Y(E_0) = q s_n^{KrC}(\varepsilon_L) \frac{\left(\frac{E_0}{E_{th}}-1\right)^{\mu}}{\lambda/w(\varepsilon_L)+\left(\frac{E_0}{E_{th}}-1\right)^{\mu}} \tag{3.28}$$

Where $s_n^{KrC}(\varepsilon_L)$ is the nuclear stopping power for KrC Wilson-Haggmark-Biersack (WHB) potential given by:

$$s_n^{KrC}(\varepsilon_L) = \frac{0.5\ln(1+1.2288\varepsilon_L)}{w(\varepsilon_L)},$$

$$w(\varepsilon_L) = \varepsilon_L + 0.1728\sqrt{\varepsilon_L} + 0.008\varepsilon_L^{0.1504} \ ,$$

ε_L is the reduced energy given by:

$$\varepsilon_L = E_0 \frac{M_2}{M_1+M_2} \frac{a_L}{Z_1 Z_2 e^2} = \frac{E_0}{\varepsilon} \ ,$$

a_L is the Lindhard screening length given by:

$$a_L = \left(\frac{9\pi^2}{128}\right)^{1/3} a_B \left(Z_1^{2/3} + Z_2^{2/3}\right)^{-1/2},$$

a_B is the Bohr radius, Z_1 Z_2 and M_1 M_2 are the atomic numbers and atomic masses of the incident particle and target atom, E_{th} is the threshold energy which is a fitting parameter as well as q for the absolute yield, λ for the decrease of the yield at low energies towards the threshold, and μ for the strength of this decrease.

3.3.8 Sputtering interactions

The ions acquire energy when they are accelerated across the cathode sheath in the direction of the target. $E = eV_{\mathrm{T}}$, Target potential drop (V_{T}), which is about equivalent to the applied voltage. Several interactions, including implantation, sputtering, or secondary electron emission, may take place when the ions reach the target. The number of sputtered atoms per incident ion is indicated by the sputter yield Y, which is given by:

$$Y = \frac{3}{4\pi^2} \alpha_{\mathrm{MR}} \frac{\eta E}{U_{\mathrm{S}}} \tag{3.29}$$

According to this equation, α_{MR} represent the mass ratio of the incident particle and the target atom, E is the ion energy, and U_{S} is the surface binding energy [101]. The energy transfer factor for an elastic collision η depends on the masses of the involved particles m_1 and $m_2$and is given by:

$$\eta = \frac{4m_1 m_2}{(m_1+m_2)^2} \tag{3.30}$$

Sputtering is only achievable above specific threshold energy because the material's surface binding energy needs to be overcome. The threshold energy is given by:

$$E_{\mathrm{th}} = \frac{U_{\mathrm{S}}}{\eta(1-\eta)} \tag{3.31}$$

The threshold energy normally is between 20 and 40 eV. The equations above demonstrate that the sputter yield rises linearly with incident ion energy. This is true for the energy ranges (100–1000 V) that are frequently utilized in sputtering. Since the ions can penetrate the material more deeply at higher energies and surface atoms are less impacted, the sputter yield begins to drop.

The energy distribution of the atoms sputtered from the target $f(E)$can be described by the Thompson distribution:

$$f(E) \propto \frac{E}{(E+U_S)^3} \tag{3.32}$$

With E the energy of the sputtered atoms [102].

Additionally, the impacting ions cause secondary electron emission, which can maintain the plasma's life. The secondary electron yield γ_{SE} , which is referred to as the ratio of emitted electrons to received ions, is what distinguishes the emission of secondary electrons. The two mechanisms that cause secondary electron emission are kinetic emission and potential emission [103]. The main mechanism in the case of metal targets is potential emission, which is

comparable to an Auger reaction in that an electron from the target neutralizes the incoming ion. The excess energy of this process leads to the emission of a secondary electron. The yield of this mechanism depends on the work function of the target material W and the ionization energy of the incoming ion E_i . Several empirical expressions have been proposed to describe the secondary electron yield γ_SE in the case of potential emission [104]:

$$\gamma_\mathrm{SE} = 0.032(0.78E_\mathrm{i} - 2W) \quad (3.33)$$

$$\gamma_\mathrm{SE} = 0.016(E_\mathrm{i} - 2W) \quad (3.34)$$

$$\gamma_\mathrm{SE} = \frac{0.2(0.8E_\mathrm{i} - 2W)}{E_\mathrm{F}} \quad (3.35)$$

The kinetic energy of the impinging ions causes electrons to be released in the case of kinetic emission. When the energy levels are higher than those typical in sputtering processes, this emission process becomes dominant [105]. The sputtering of insulating materials, such as broadband gap oxides or nitrides, can involve kinetic emission.

The ionization of Argon atoms by the secondary electrons keeps the plasma alive, the minimum voltage required for maintaining the discharge V_d is therefore closely related to the secondary electron yield γ_SE and is given by

$$V_\mathrm{d} = \frac{U_\mathrm{i}}{e\gamma_\mathrm{SE}\epsilon_\mathrm{i}\epsilon_\mathrm{e}f_\mathrm{m}f_\mathrm{eff}} \quad (3.36)$$

With U_i the average energy loss per ionization which is around 30 eV for an Ar discharge. The other coefficients in this Equation correspond to different loss or multiplication mechanisms. The coefficient ϵ_i describes the loss due to ions that are created far from the target and the coefficient $\epsilon_\mathrm{e}$is due to electrons being lost at the anode. The coefficient f_m is a multiplication parameter due to electrons that are created in the cathode sheath and gain enough energy to produce more ions. The coefficient f_eff describes the effective ionization probability that takes the recapture of electrons by the target into account. The effective ionization probability depends on the pressure. At low pressure, fewer ionization events are expected, which leads to a higher discharge voltage.

3.4 Conclusion

It is crucial to comprehend the various numerical simulations techniques of the sputtering process, because doing so will enable you to comprehend this phenomenon's mechanics on a deeper level.

Chapter 4

Results and discussions

4.1 Introduction:

this chapter represents the work carried out using Monte Carlo simulation and will be divided into two parts, the first part introduces the software used to simulate this phenomenon and provides results about the sputtering yield found by using semiconductor and metals materials, and the second and final part deals with the transport of the atoms sputtered towards the substrate by implementing all the factor which can impact the deposition.

4.2 Part 1 Introducing the model SRIM for sputtering simulations

SRIM2013 (Stopping and Range of Ions in the Matter), developed by Ziegler et al, was used as modeling software to determine the energy distribution of the sputtered atoms and reflected ions, it was also frequently used to calculate the sputtering yield [106]. The TRIM (Transport of Ions in the Matter) module, which allows for the consideration of complicated targets such as alloys or targets made up of eight separate films, was employed as one of the modules in this software that can compute the path of ions in the material. It takes into account every kinetic phenomenon connected to the ion's energy loss, including sputtering, ionization, and phonon production. Additionally, it can identify the cascades of collisions that occur in the target and show which atoms arrive at the surface with the appropriate energy. [107]

The calculation technique relies on a Monte Carlo code that simulates the movement and interaction of an ion beam on the surface of a target material and also makes it possible to calculate the sputtering yield. This model applies more for energy far greater than the sputtering threshold because it requires binary collisions.

The model has many input factors, such as displacement energy, surface energy, and so on, but the binding energy of the target material is crucial for the sputtering portion because it has a greater impact on the outcomes than the other components.

4.2.1 SRIM on sputtering calculations

Secondary electrons are released by the ions bombarding the cathode, which are required for the discharge to self-maintain. Sputtering is a result of these incident ions as well. Atoms of the cathode material can be ejected if their energy exceeds the sputtering threshold energy. The energy of the incident ions at the cathode, in particular, plays a key role in the sputtering's yield, which is dependent on several factors.

The TRIM module was set up for this work in the "Surface Sputtering/Monolayer Collision stages" mode, which accurately processes a target's sputtering. Our simulation study with

SRIM2013 is divided into two parts. The first part is to find the best angle of incidence and the bombardment energy that can give the best sputtering result using the following materials (CZTS, Si). We varied the bombardment energy and angle with 1000 ions (it's the number of

Argon ions that bombard the target), and SRIM2013 automatically selected the density of the semiconductors. The simulation gives the sputtering yield sum of the semiconductor elements; the second part of our work is to analyze each semiconductor element that was selected. To make the simulation, we chose the best angle and energy of sputtering (found in the first part) and we apply for this time the semiconducting compounds Copper zinc tin sulfide (CZTS) and copper indium gallium selenide (CIGS) as target materials, the number of ions that will bombard the target was increased into 5000 ions to receive good results. Of course, SRIM always chooses the density automatically. After simulation, we will obtain the sputtering yield of each semiconductor component. The statistical algorithm (Figure 4.1) is efficient to calculate the sputtering yield via the Monte Carlo method:

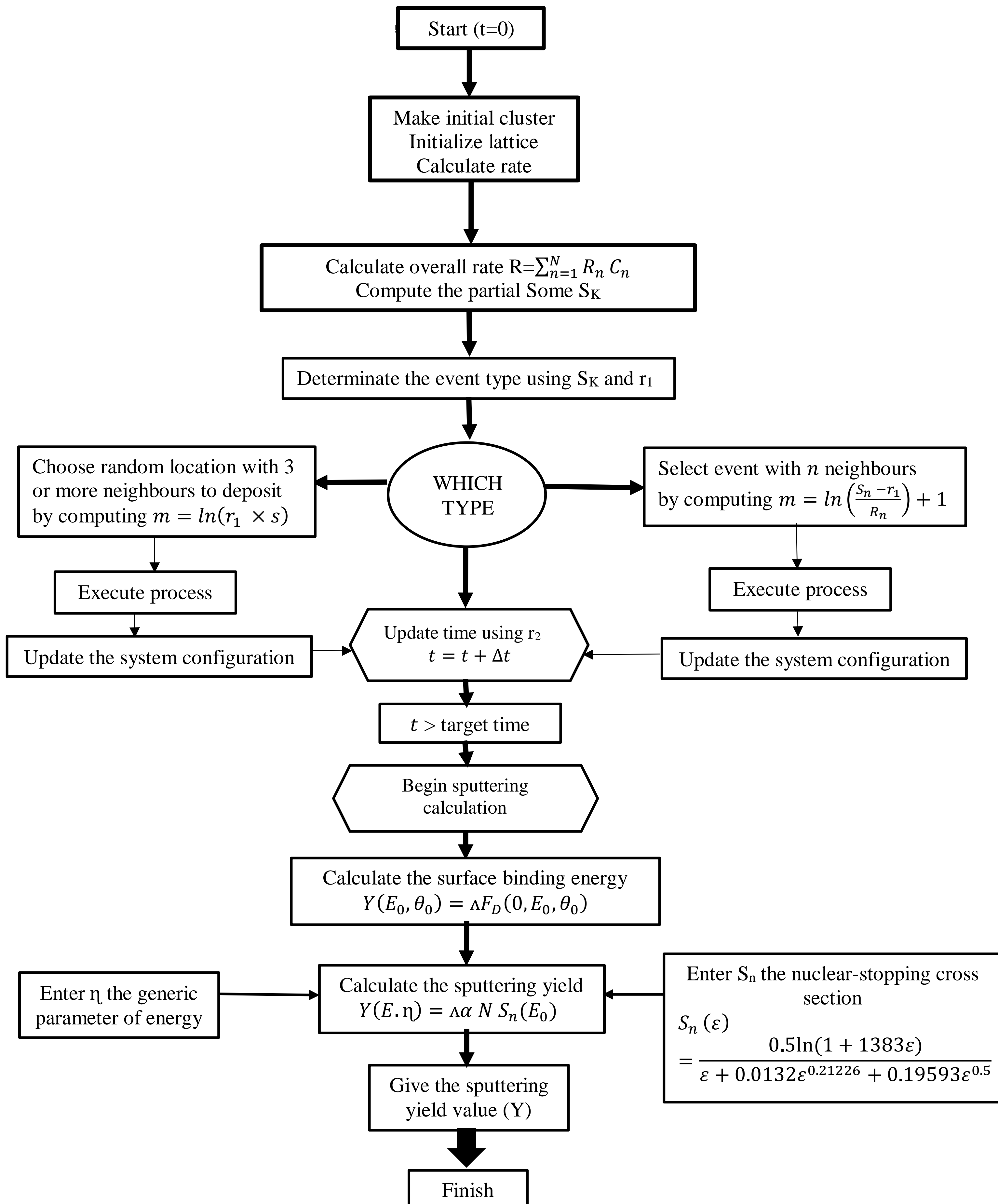

Figure 4.1. Monte Carlo simulation flowchart

4.2.2 Sputtering yield depending on the energy of bombardment and fixed angles of incidence

In the figures below, we present three-dimensional curve results of the sputtering yield calculations obtained by Monte Carlo simulations, three different angles of incidence are used $\theta = [40°, 60°, 85°]$, on each angle the sputtering yield is varied according to the energy, the target is being bombarded by Argon ions using the following materials (CZTS, Si).

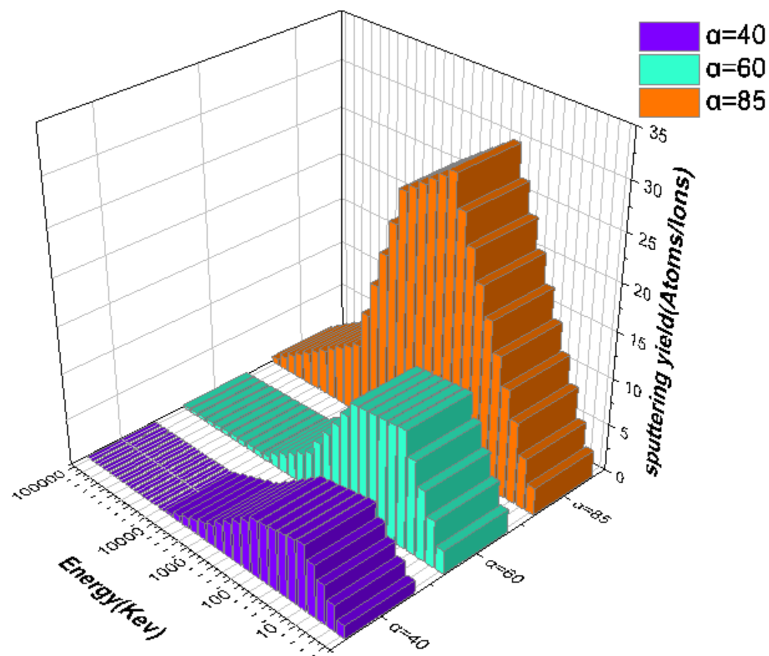

Fig 4.2. Sputtering yield as a function of the energy of the bombardment ions

(Ar) on three incidence angles θ= [40°, 60°, 85°] calculated by MC method for (Cu_2ZnSnS_4)

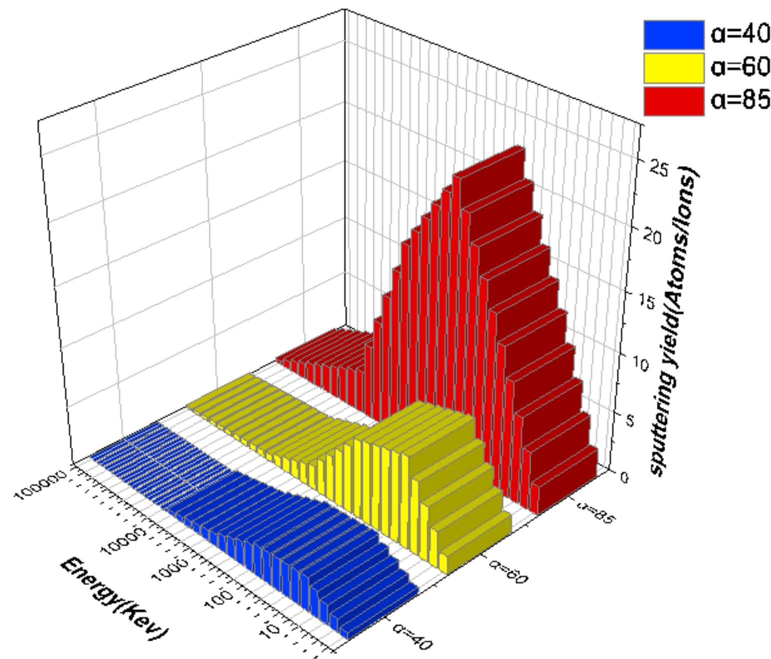

Fig 4.3. Sputtering yield as a function of the energy of the bombardment ions (Ar) on three incidence angles θ= [40°, 60°, 85°] calculated by MC method for (Si)

As shown in the figures above, on each semiconductor used, the angle with a value of 85 degrees gives the highest sputtering yield, we also notice that the increase of the bombardment energy will create a peak named E_{max} if we exceed this value of the sputtering yield will drop.

In order to find the best sputtering yield, the incidence angle and the bombardment energy must be taken into consideration.

The preceding curves can be devised in three zones:

Zone 1: the bombardment energy is too low for the sputtering process to begin, the argon ions have low energy to reach the target.

Zone 2: when the bombardment energy reaches the threshold the sputtering process starts, and the argon ions bombard the target which will start the ejection of atoms from the target, we can increase the bombardment energy up to a limit called (E_{max}).

Zone 3: the sputtering process reaches its limit, if we add more energy the yield decreases in this case the ions have very high energy the incident particles penetrate so deeply into the target that the recoil atoms cannot escape.

4.2.3 Sputtering yield depending on incidence angles and fixed energies of bombardment

For this time, we took the energies E (kev) = [10, 100, 1000] and on each energy, we vary the sputtering yield according to the incidence angle, the same gas and materials will be used to bombard the target, the results are presented on the following figures:

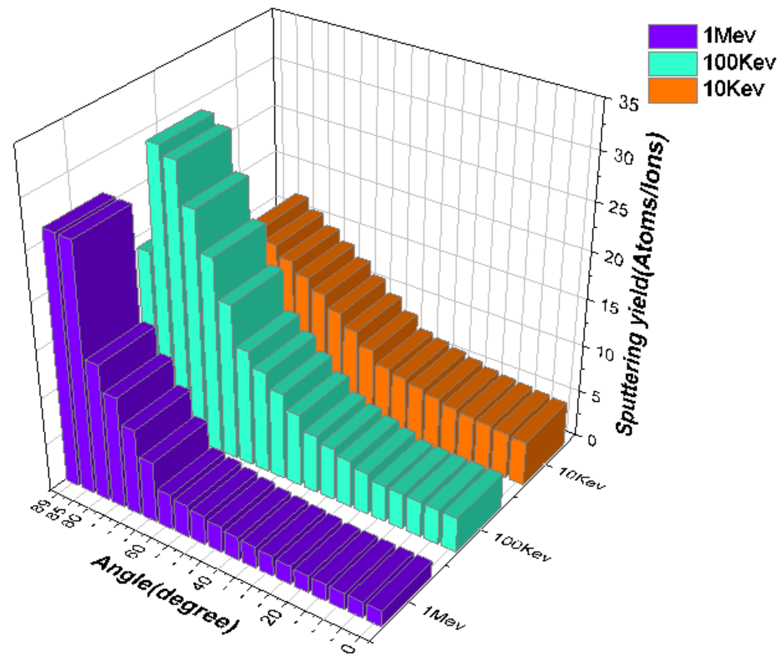

Fig 4.4. Sputtering yield as a function of incidence angles on three energies E= [10(kev), 100(kev), 1(Mev)] calculated by MC method for (Cu_2ZnSnS_4).

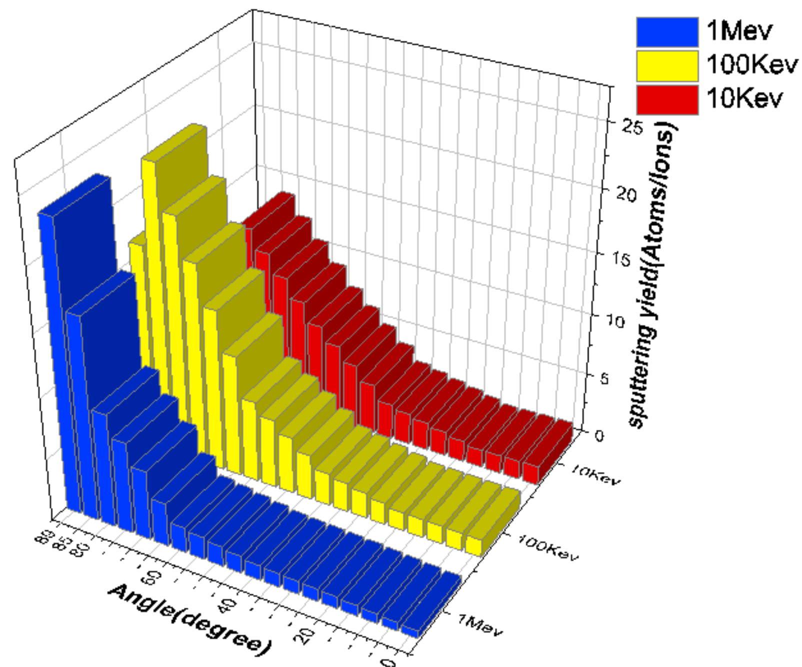

Fig 4.5. Sputtering yield as a function of incidence angles on three energies E= [10(kev), 100(kev), 1(Mev)] calculated by MC method for (Si).

The application of bombardment energy with a value of 100kev will give us the best performance, by increasing the angle of incidence the sputtering yield will also grow to a peak value named(α_{max}), exceeding this value will make the sputtering yield decline.

Choosing low bombardment energy will give fewer atoms ejected from the target, which will result in a bad sputtering yield.

4.2.4 Comparison between the two semiconductors CZTS and Silicon

In the figures below, we present the three-dimension curve results of the comparison between the two semiconductors (Cu_2ZnSnS_4) and (Si) to find out which one performs better.

We used the previous result obtained for each semiconductor; results are shown on the following curves:

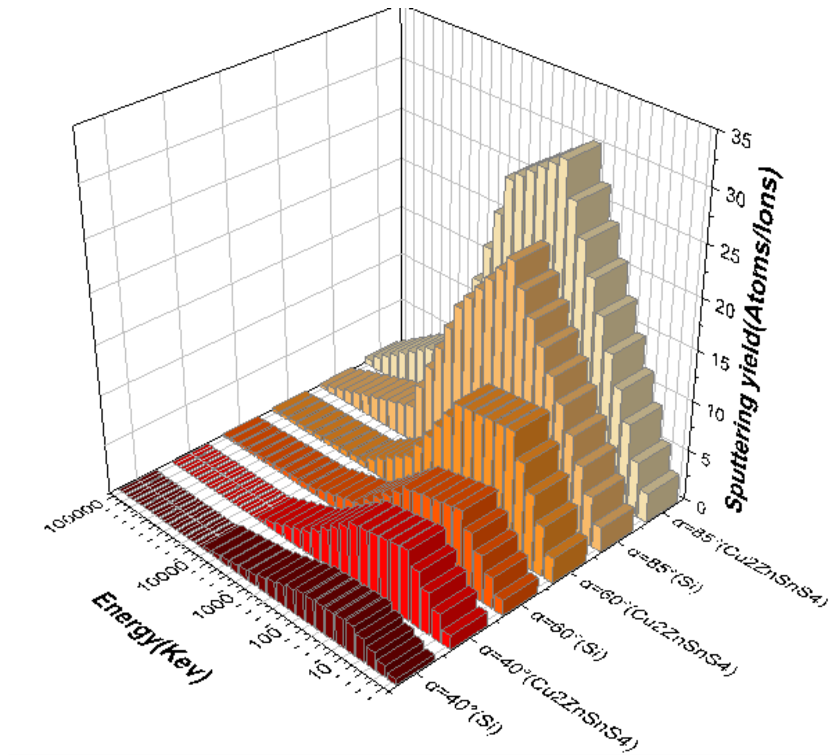

Fig 4.6. Comparison of Sputtering yield as a function of the energy of the bombardment ions (Ar) on three incidence angles θ= [40°, 60°, 85°] calculated by MC method between (Cu_2ZnSnS_4) and (Si)

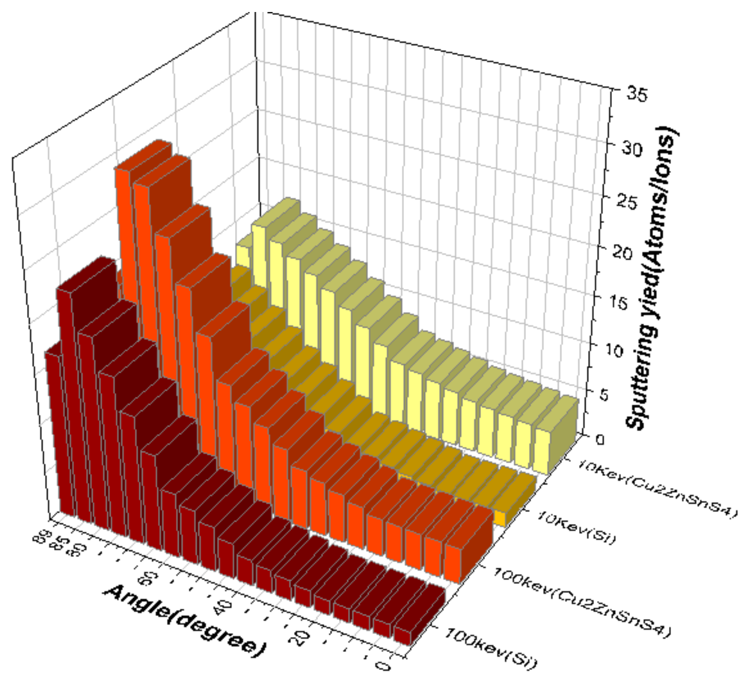

Fig 4.7. Comparison of Sputtering yield as a function of incidence angles on three energies E= [10(kev), 100(kev), 1(Mev)] calculated by MC method between (Cu_2ZnSnS_4) and (Si)

The figures above show us the following information: when we use the angle of 85 degrees the semiconductors CZTS and silicon give their best sputtering performance they reach an efficiency value of 30% and 23% respectively, from these results we can deduce that the formation of a thin layer based on CZTS using the sputtering process is better than silicon, using an energy value of 100Kev we obtain the best sputtering yield for both semiconductors CZTS and silicon with values of 30% and 23% respectively, so we deduce the same result that CZTS is more effective than Si, In conclusion, to obtain the best sputtering performances we have to take an incidence angle of 85 degrees with a bombardment energy value of 100kev.

4.2.5 The atoms ejected from each element of the compounds CZTS and CIGS

In this case, we're going to study the atoms ejected from each element of the semiconducting compounds Copper zinc tin sulfide (CZTS) and for the copper indium gallium selenide (CIGS) $CuIn_xGa_{(1-x)}Se_2$, where the value of x can vary from 1 (pure copper indium selenide) to 0. For both semiconductors, we use an angle of 85° and a bombardment energy value of 100kev.

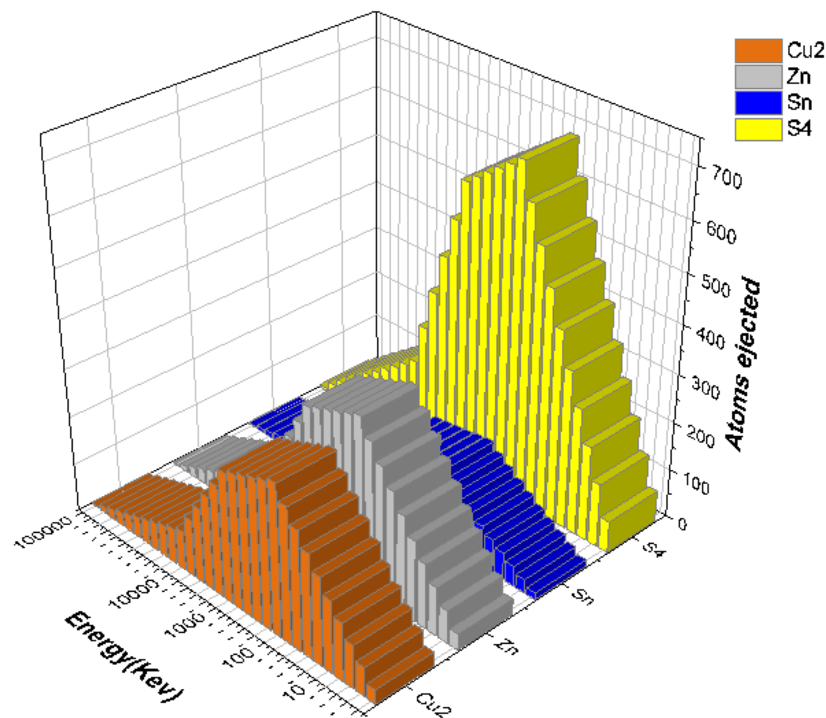

Fig 4.8. Atoms ejected as a function of the energy of the bombardment ions (Ar) on the incidence angles θ= [85°] calculated by MC method for each element of the compound (Cu_2ZnSnS_4)

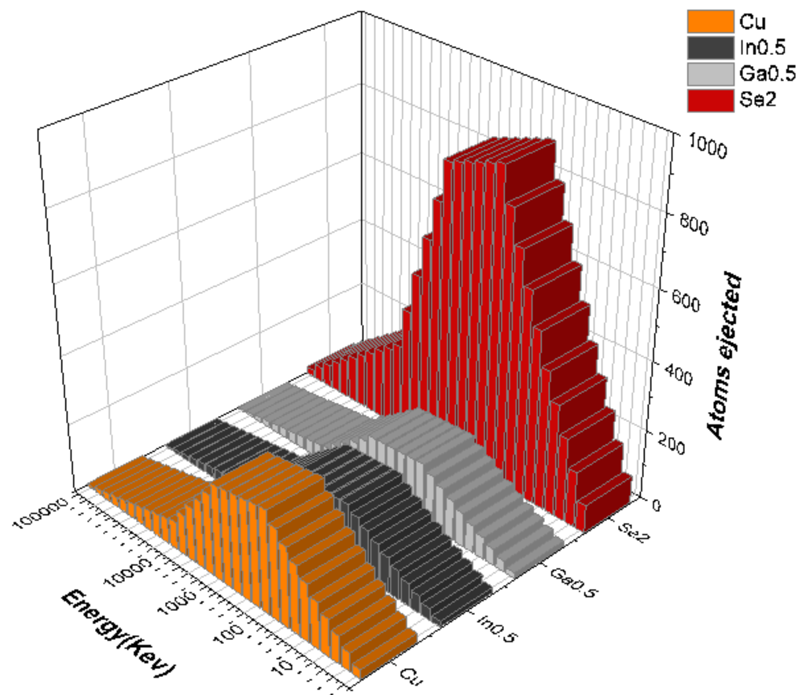

Fig 4.9. Atoms ejected as a function of the energy of the bombardment ions (Ar) on the incidence angles θ= [85°] calculated by MC method for each element of the compound ($CuIn_{0.5}Ga_{0.5}Se_2$)

On the CZTS semiconductor, the element which gives the most ejected atoms is the sulfur (S) called sulfide (S_4) followed by copper (Cu) and zinc (Zn) which have almost the same number of ejected atoms, and we finish with tin (Sn) giving a very low ejection number compared to the other materials.

On the semiconductor CIGS the element that gives the most atoms ejected and exceeds the other elements with a large gap is selenium (Se) named selenide (Se_2) followed by copper (Cu) and we end up with indium (In) and gallium (Ga) which both have a very small number of atoms ejected compared to other materials.

The following table shows the percentage of atoms ejected from the semiconductors CZTS and CIGS:

Semiconductors	CZTS				CIGS			
Materials	Cu_2	Zn	Sn	S_4	Cu	$In_{0.5}$	$Ga_{0.5}$	Se_2
Number of atoms ejected	314	352	152	684	299	184	173	888
Total number of atoms ejected	1502				1544			
the percentage of atoms ejected	20.90%	23.43%	10.11%	45.53%	19.36%	11.91%	11.20%	57.51%

Table 4.1. The percentage of atoms ejected on an argon bombardment energy of 100Kev for each material

From the table, we notice that the presence of sulfide (S_4) is very important for the CZTS semiconductor it gives a percentage value of 45.53% from the total number of ejected atoms, and for the semi-conductor CIGS we perceive that the selenide (Se_2) gives a percentage value of 57.51%, so it outperforms other equipment by far, and it plays a major role in achieving good sputtering performance.

4.2.6 Comparison between the two compounds CZTS and CIGS

The figure below represents a comparison of atoms ejected between the semiconducting compounds CZTS and CIGS

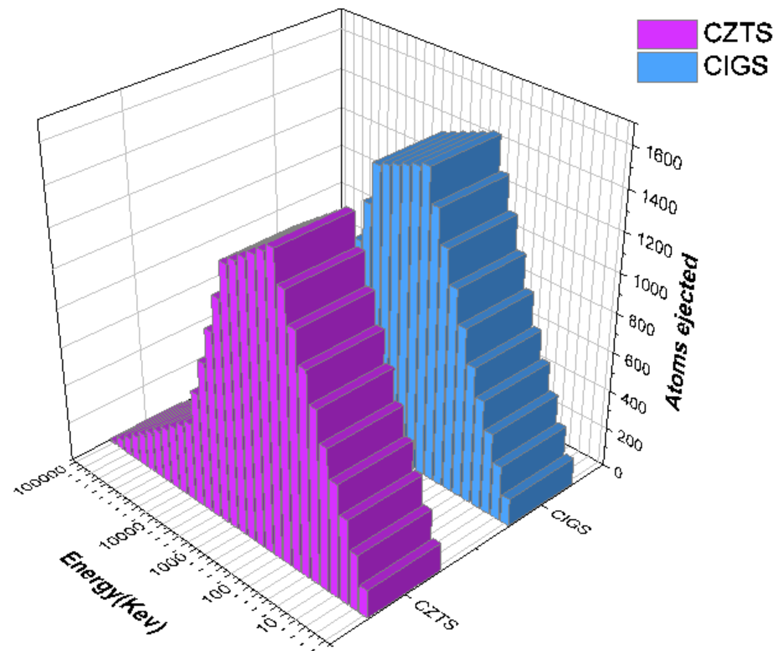

Fig 4.10. Comparison of Atoms ejected as a function of the energy of the bombardment ions (Ar) on the incidence angles θ= [85°] calculated by MC method between the semiconducting compounds (CZTS) and (CIGS)

According to the figure above, after adding up the atoms ejected for each material of both semiconductors, we have found almost the same result, but we can say that each material can act differently and create a thin layer with different quality and performance.

4.3 Part 2: the transport of the atoms sputtered toward the substrate

As they travel to the substrate, the sputtered particles expelled from the target may come into contact with gas atoms in the vacuum chamber. The film deposition depends on collisional transport, which represents the pathways of sputtered atoms from the target through the gas to the substrate.

Particle collisions during transport with specific gas atoms depend on the mean free path, with each collision event being considered an elastic/inelastic event that modifies the particle's velocity vector. Calculating a collision's energy loss, velocity, and angle between the pre-collision and post-collision trajectories is possible. The particles' energy, direction, and momentum will all be altered by the impact, which will also affect their momentum and microstructure as the film grows [108, 109]. The most crucial factors that can affect the

deposition of the atoms ejected into the substrate are: pressure, the temperature inside the vacuum chamber, and the target-substrate distance, in order to study the impact of all these factors and the transport of the atoms ejected from the target towards the substrate we will use a numerical model called SIMTRA (Simulation of Metal Transport).

4.3.1 Simulation method

The kinetic energy and the number of atoms that arrived at the substrate location are calculated by SRIM and SIMTRA, first, the energy and the direction of the particles that are sputtered far away from the target are calculated by using SRIM software.

In this work, we started with SRIM so we injected around 10^4 argon and xenon ions to bombard with 100kev of energy and 85 degrees as an incidence angular the three deferent targets (Si, Ge, Cu) respectively, the best choice of bombardment gas is also important that’s why we applied inside the vacuum chamber this knowing values. The transport of the obtained sputtered atoms from the target to the substrate is then covered by the SIMTRA code by taking into account all collisions occurring in the gas phase.

We created a magnetron sputtering system, first, a vacuum chamber is designed with 30cm×30cm×50cm in dimension, 15cm in distance between target and substrate, a circle shape with 2cm in the radius of the magnetron target, and also 7cm in the substrate radius were chosen as shown in (Fig4.11). we did a gas temperature and pressure variation with the objective to deduce their impact on the number of atoms deposition and with which energy they reach the substrate that extrapolates directly the thickness of the thin films built, after all these configurations, we can start the simulation of this model to calculate the total number of particles arriving on the substrate, their position, and energy. The results will be saved on data files and will be represented by 3D curves.

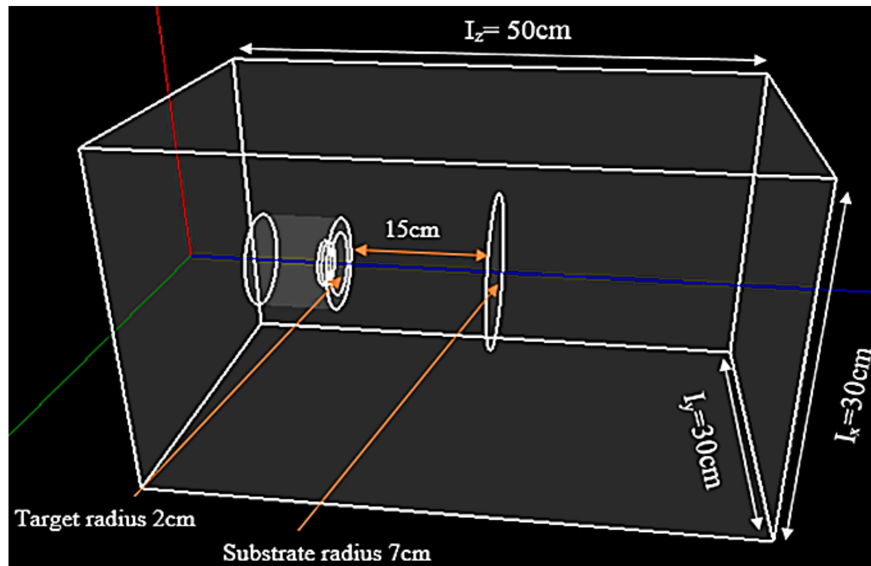

Fig 4.11. The model used in the simulation

4.3.2 Influence of temperature and high pressure on the sputtered atoms arriving on the substrate using Argon and xenon gas

4.3.2.1 Variation of temperature with a fixed pressure for Argon ions:

On the vacuum chamber, the target which contained materials (Si, Ge, and Cu) is being bombarded by Argon gas ions with a fixed pressure of 0.5 Pa and three different temperature values (100K, 300K, and 600K).

The following set of figures represents the number of atoms that sputtered and arrived on the substrate for each temperature.

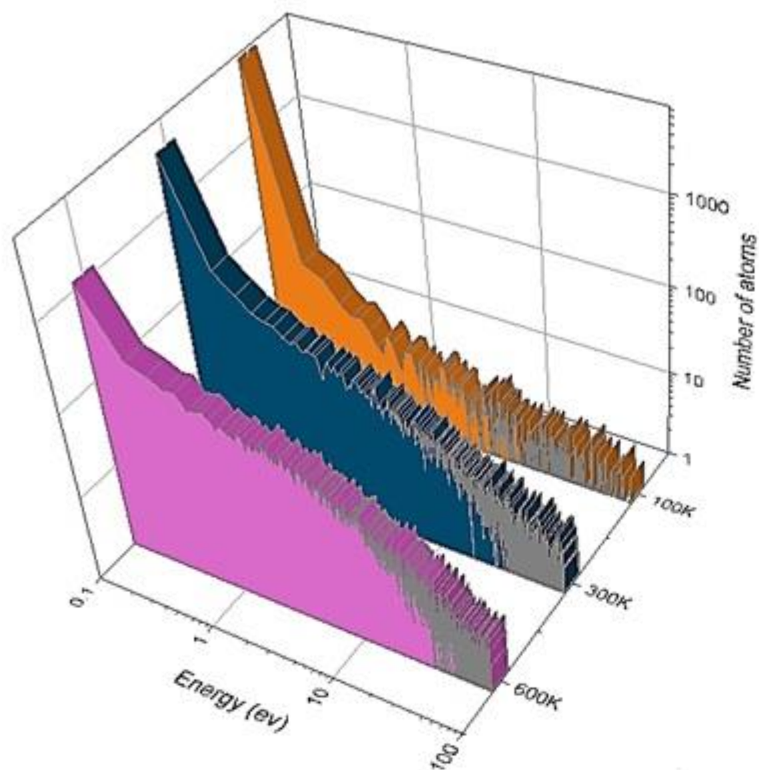

Figure 4.12. Number of arriving Si atoms as a function of the energy distribution using three different temperatures T= [100K, 300K, 600K]

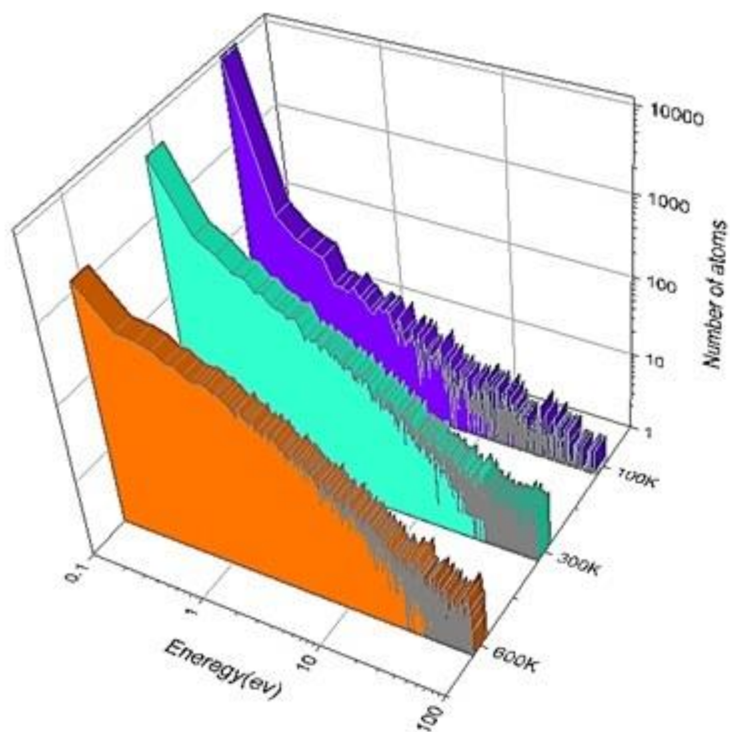

Figure 4.13. Number of arriving Ge atoms as a function of the energy distribution using three different temperatures T= [100K, 300K, 600K]

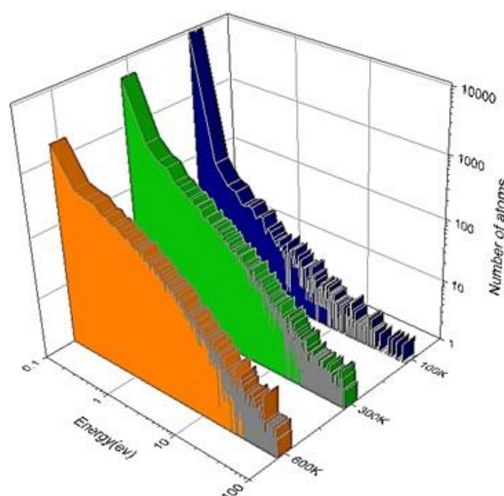

Figure. 4.14. Number of arriving Cu atoms as a function of the energy distribution using three different temperatures T= [100K, 300K, 400K]

As shown in the figures above, the numbers of atoms that reached the substrate are different on each adjusted temperature, we notice that when 100k is applied, for example, the Ge and the Cu are around the 13 and 11k respectively while in Si is 9K atoms. The increase in temperature will create heat inside the vacuum chamber that will rise the mobility and the energy of the Argon gas particles which will bombard the target with great energy and lead to the expand of the number of ejected atoms. Applying 300k and then 600k grows the particle number that arrives at the substrate (see table 4.2).

materials	temperature	Total number of atoms
Si		9183
Ge	100K	13732
Cu		11901
Si		12922
Ge	300K	16286
cu		15219
Si		14301
Ge	600k	16393
cu		15225

Table 4.2 Total number of metals atoms arrived at the substrate depending on temperatures

4.3.2.2 Variation of pressure with a fixed temperature for Argon ions:

Now, we will use three different pressure P= [0.5Pa, 2PA, 5Pa], and with a fixed temperature value of 300k applied inside the vacuum chamber, the same gas and materials will be used to bombard our target, the results are presented on the following figures:

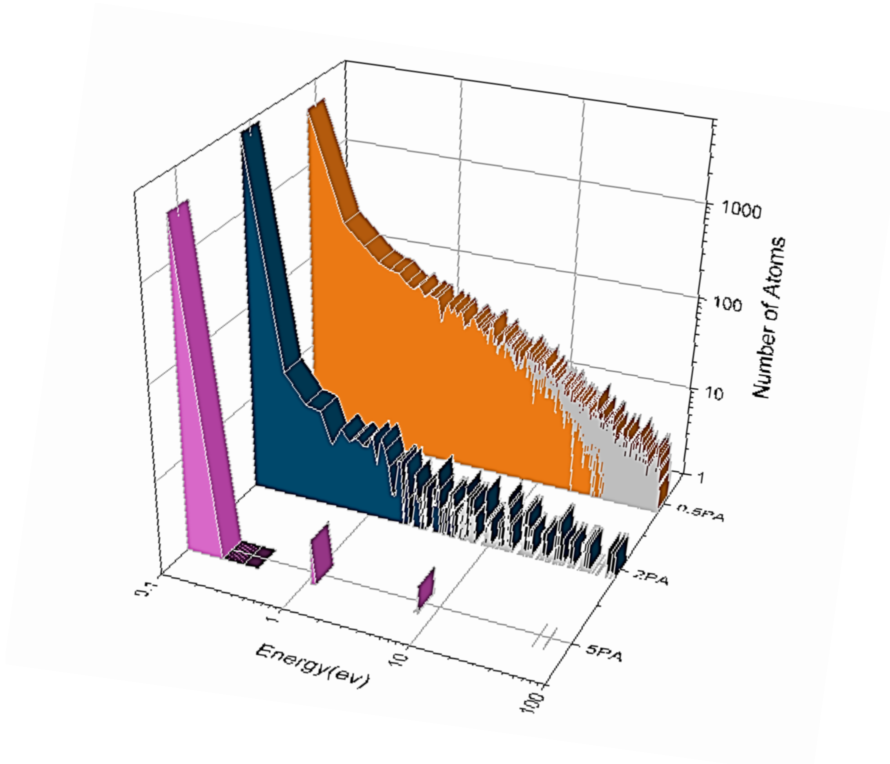

Figure 4.15. Number of arriving Si atoms as a function of the energy distribution using three different pressures P= [0.5Pa, 2Pa, 5Pa]

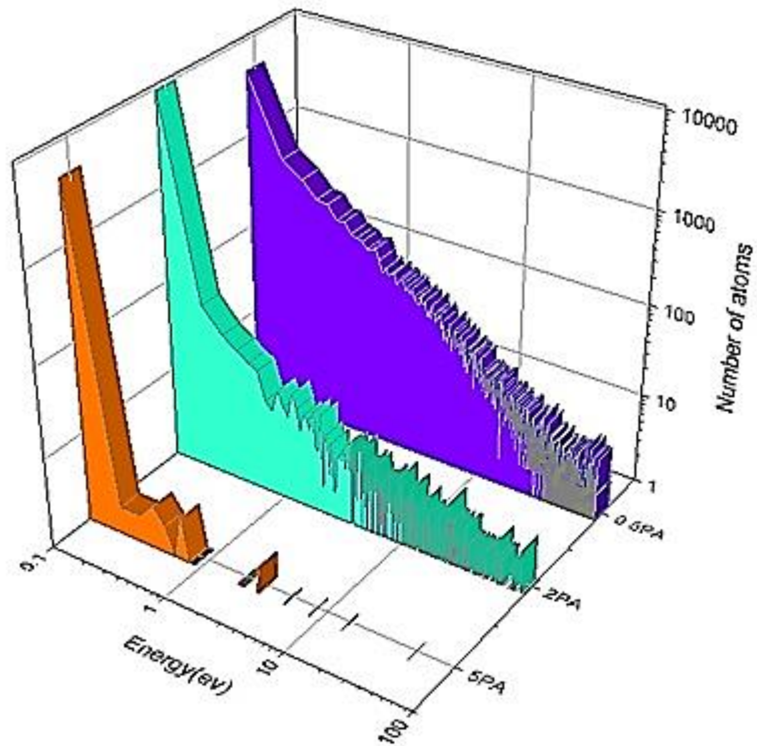

Figure 4.16. Number of arriving Ge atoms as a function of the energy distribution using three different pressures P= [0.5Pa, 2Pa, 5Pa]

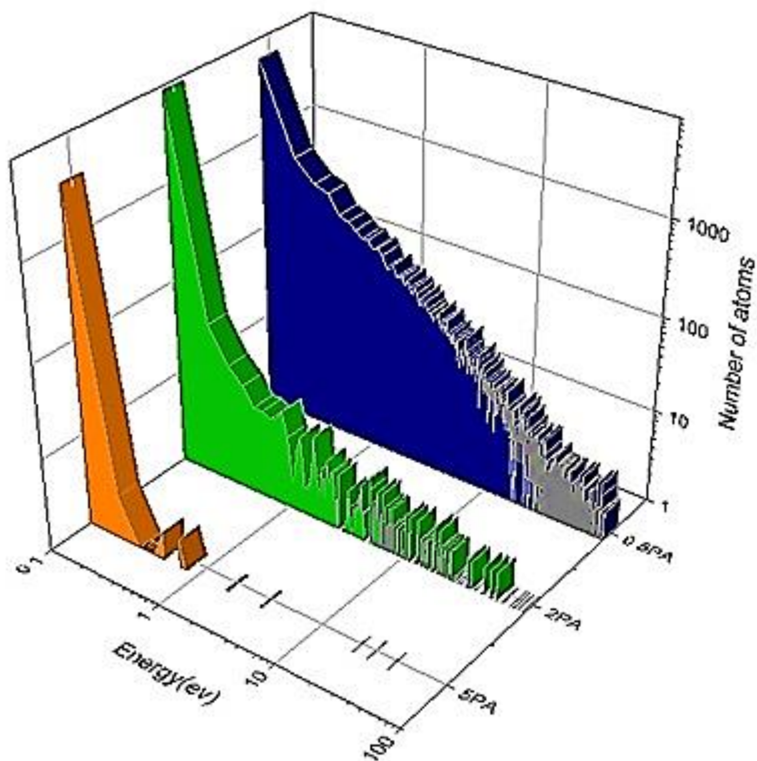

Figure 4.17. Number of arriving Cu atoms as a function of the energy distribution using three different pressures P= [0.5Pa, 2Pa, 5Pa]

According to the previous graphs (Fig.6, 7, and 8), the pressure has a colossal influence on the number of atoms in general (ejected from the target or arrived at the substrate), they are showing that when 0. 5Pa is applied, and around 16K, 15K, and 12K arriving atoms for Ge, Cu, and Si severally were obtained. Enlarging the vacuum chamber pressure to higher values produces a very large number of collisions and a huge drop in particle mobility, the ejected atoms collide then with the Argon ions which will decrease their kinetic energy and will face a difficult path to reach the substrate. After applying a pressure of 2Pa and 5Pa, there is a very large decrease in the number of atoms reaching the substrate with an important fall-off in their energies (see table 4.3).

Materials	Pressure	Total number of atoms
Si	0.5Pa	12922
Ge		16286
Cu		15219
Si	2Pa	7666
Ge		11353
cu		9134
Si	5Pa	3453
Ge		4940
cu		3604

Table 4.3 Total number of metals atoms arrived at the substrate depending on pressures with argon gas ions bombardment

Applying a low pressure inside the vacuum chamber will cause less collision between the particles so the ejected atoms will have a free path to reach the substrate.

4.3.2.3 Variation of temperature with a fixed pressure for Xenon ions:

The same procedure will be carried out, temperatures range T= [100K, 300K, 600K] and 0.5Pa as a fixed vacuum chamber pressure, the only difference is that this time we will use xenon instead Argon as bombardment gas.

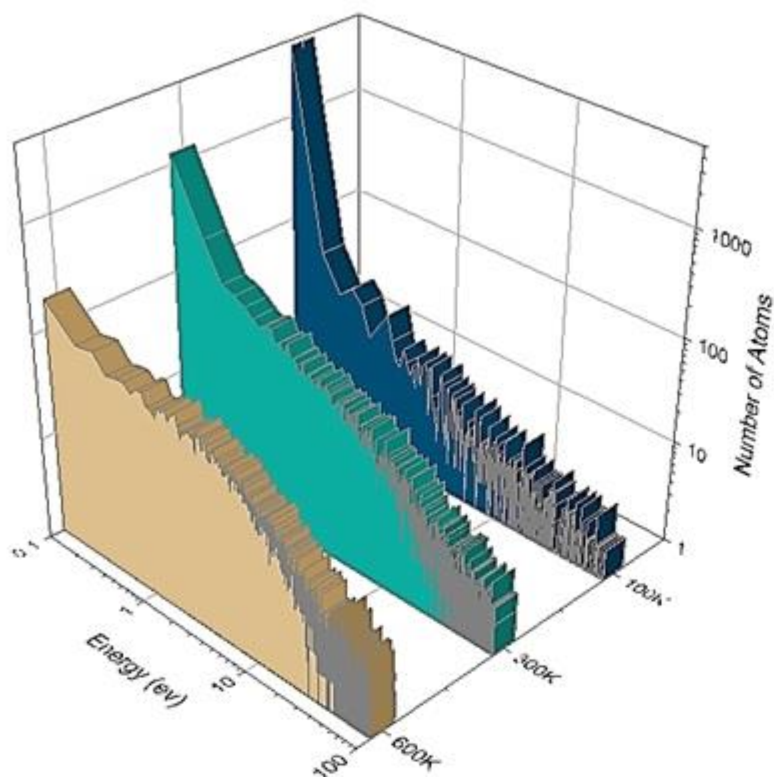

Figure 4.18. Number of arriving Si atoms as a function of the energy distribution using three different temperatures T= [100K, 300K, 600K] with Xenon gas

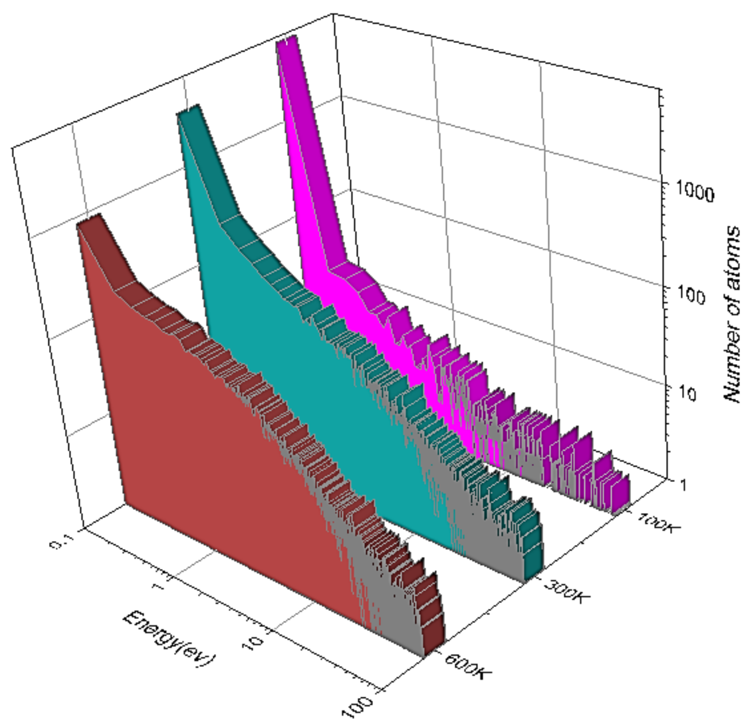

Figure 4.19. Number of arriving Ge atoms as a function of the energy distribution using three different temperatures T= [100K, 300K, 600K] with Xenon gas

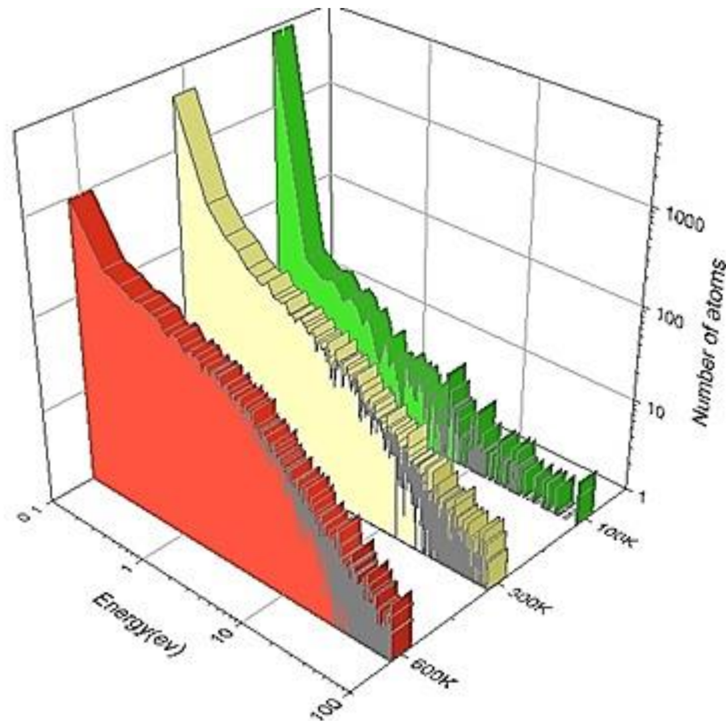

Figure 4.20. Number of arriving Cu atoms as a function of the energy distribution using three different temperatures T= [100K, 300K, 600K] with Xenon gas

Replacing the Argon with Xenon as vacuum chamber gas and with the application of the same procedures described above, the results obtained indicate a very large decrease in the number of atoms arriving on the substrate, an applied temperature of 100k gives around 8K of atoms for the Ge comparing to 13k with Argon, almost the same thing take place to other materials (Cu and Si) from about 7K atoms to 10K. Xenon ions are known for their high bombardment energies which gives a very large number of atom ejected and a good sputtering yield but this energy can damage some of the ejected atoms so they won't be able to travel to the substrate, that's why we must always choose a target compatible with the chosen gas.

Increasing temperature will increase the total number of particles arriving at the final destination (substrate) (as shown in table 4.4).

materials	temperature	Total number of atoms
Si	100K	7249
Ge		8061
Cu		6895
Si	300K	10273
Ge		11603
cu		10684
Si	600k	12421
Ge		13021
cu		11976

Table 4.4 Total number of metals atoms arrived at the substrate depending on temperatures with Xenon gas ions bombardment

4.3.2.4 Variation of pressure with a fixed temperature for Xenon ions:

Now we apply the xenon gas on three different pressure P= [0.5Pa, 2Pa, 5Pa] and 300K as a fixed vacuum chamber temperature. Argon gas used in the vacuum will be replaced by Xenon.

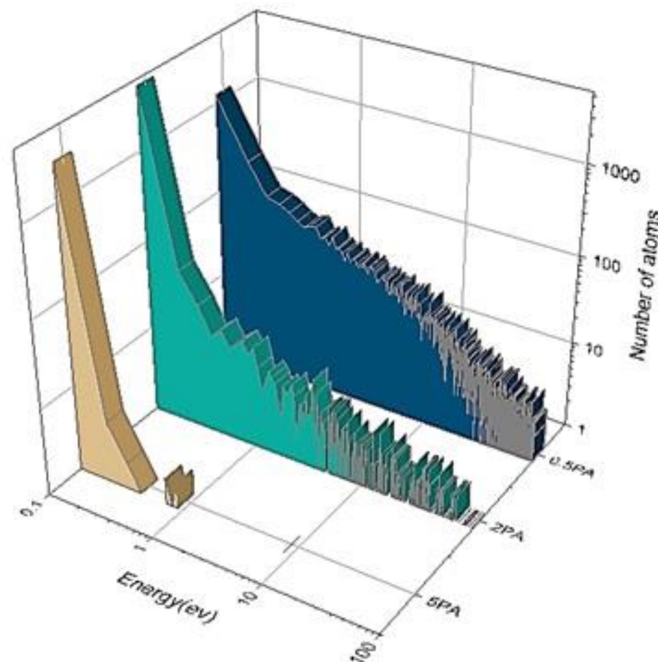

Figure 4.21. Number of arriving Si atoms as a function of the energy distribution using three different pressures P= [0.5Pa, 2Pa, 5Pa] with Xenon gas

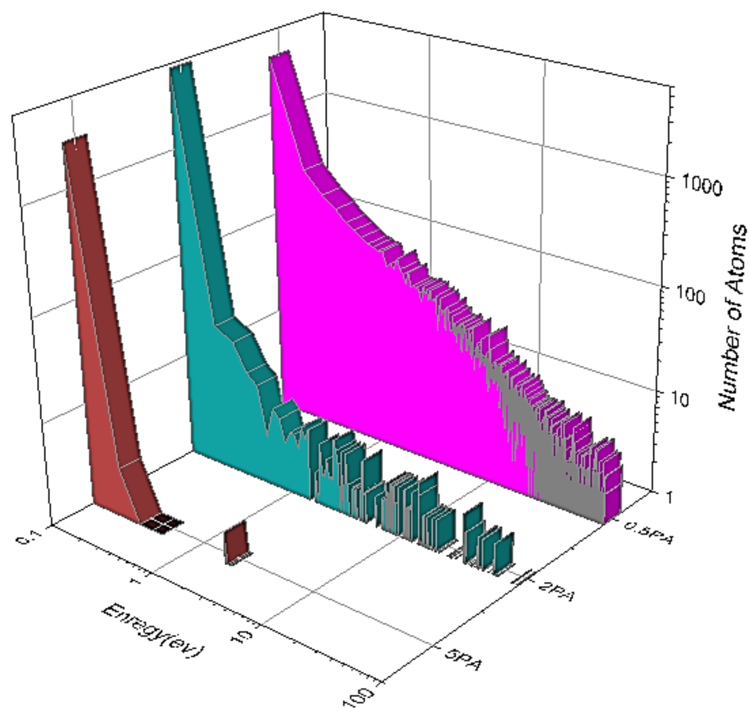

Figure 4.22. Number of arriving Ge atoms as a function of the energy distribution using three different pressures P= [0.5Pa, 2Pa, 5Pa] with Xenon gas

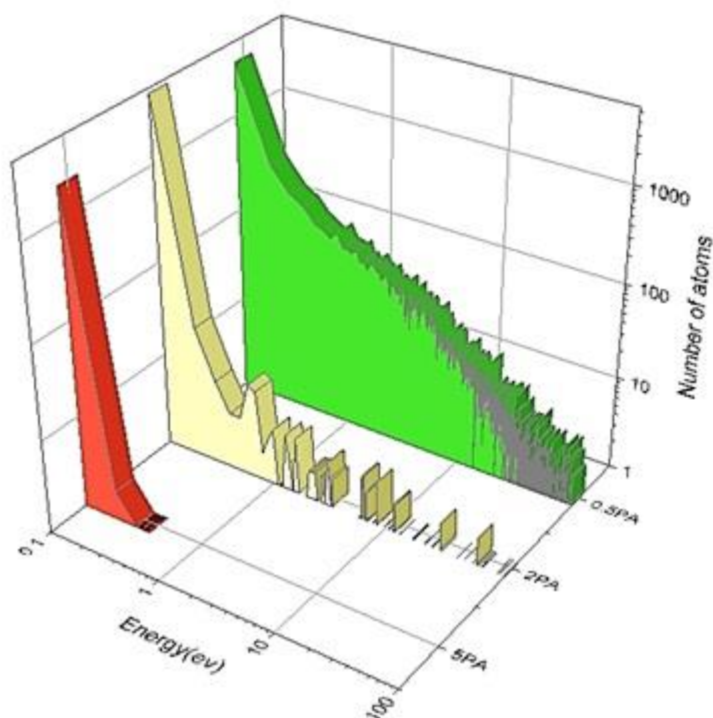

Figure 4.23. Number of arriving Cu atoms as a function of the energy distribution using three different pressures P= [0.5Pa, 2Pa, 5Pa] with Xenon gas

We can visualize in the above figures that the application of xenon gas gives the same result as Argon except that the number of atoms that arrived in the substrate has greatly diminished as we can see (in table 4.5) below, for 0.5Pa as the pressure applied, for example, 11K comparing to 16K for Ge and there about 10K compared to 15K and 12K for Cu and Si respectively. This will affect considerably the morphology of the formed thin films with less thickness and quality.

Materials	Pressure	Total number of atoms
Si	0.5Pa	10273
Ge		11603
Cu		10684
Si	2Pa	6595
Ge		6555
cu		5564
Si	5Pa	3020
Ge		2790
cu		2170

Table 4.5. The total number of metals atoms arrived at the substrate depending on pressures with Xenon gas ions bombardment

4.3.3 Comparison between materials

In order to contribute to the definition of the best parameters which helps by the end to the improvement of the thin films made and their qualities, we will compare the used materials (Si, Ge, and Cu) for each influencing parameter.

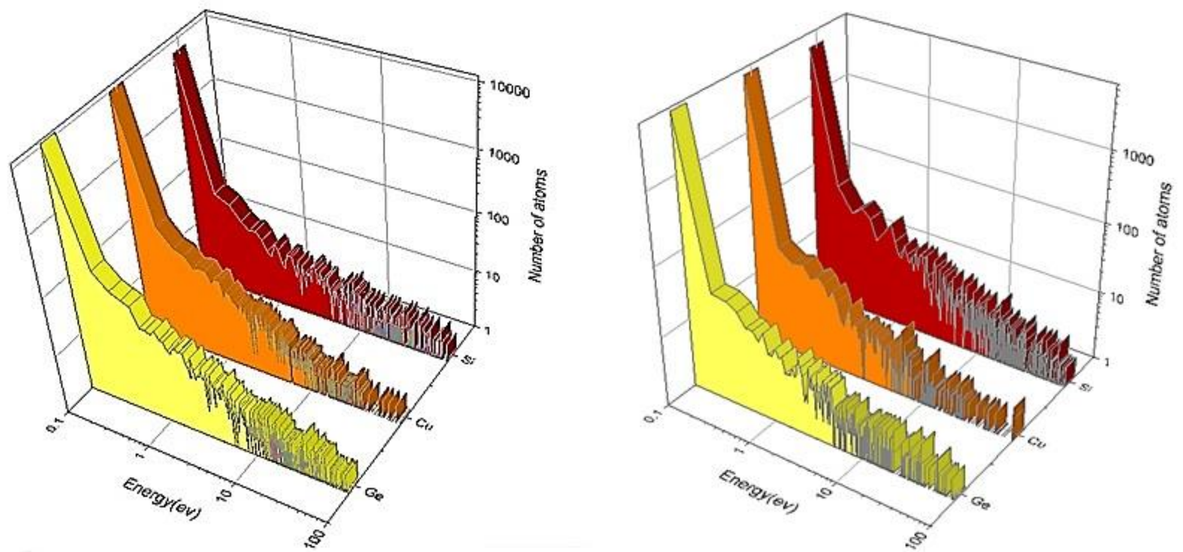

Figure 4.24. Comparison between arriving Si, Ge and Cu atoms as a function of the energy distribution for 0.5 Pa and 100K for a) Argon b) xenon

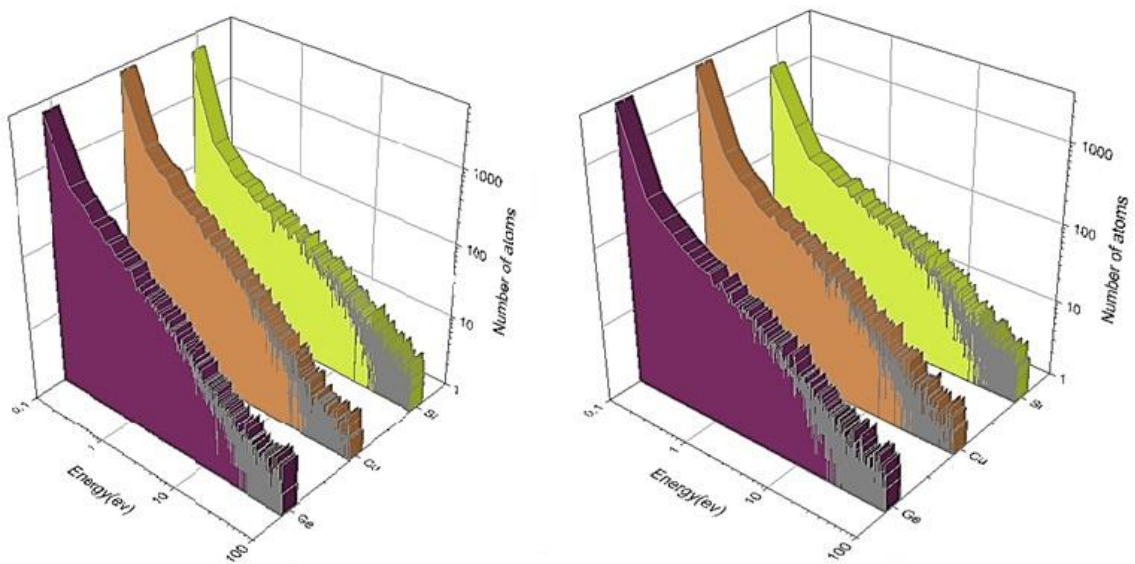

Figure 4.25. Comparison between arriving Si, Ge and Cu atoms as a function of the energy distribution for 0.5 Pa and 300K for a) Argon b) xenon

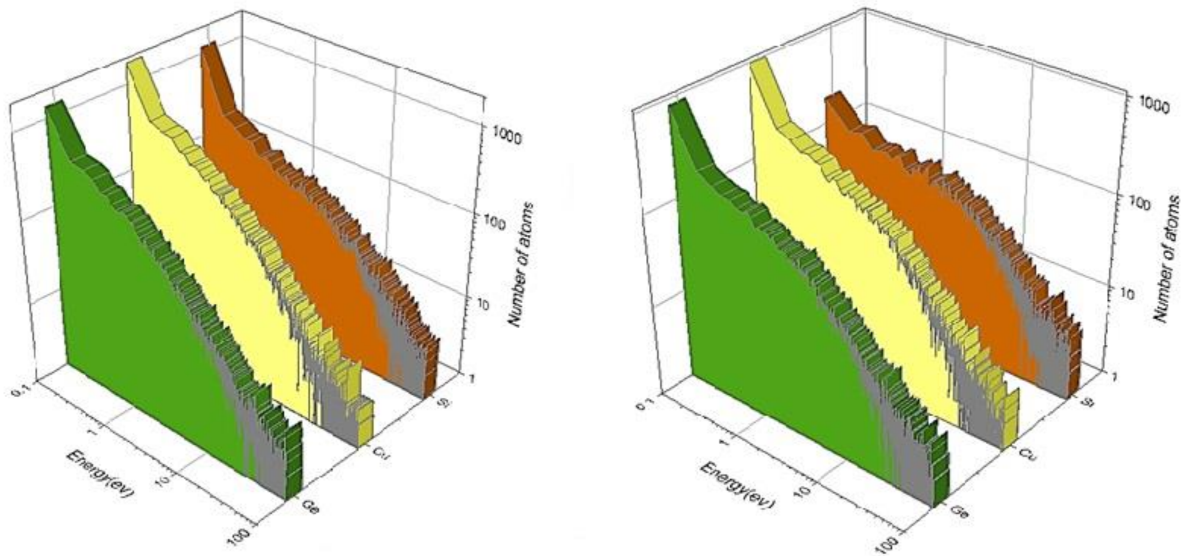

Figure 4.26. Comparison between arriving Si, Ge and Cu atoms as a function of the energy distribution for 0.5 Pa and 600K for a) Argon b) xenon

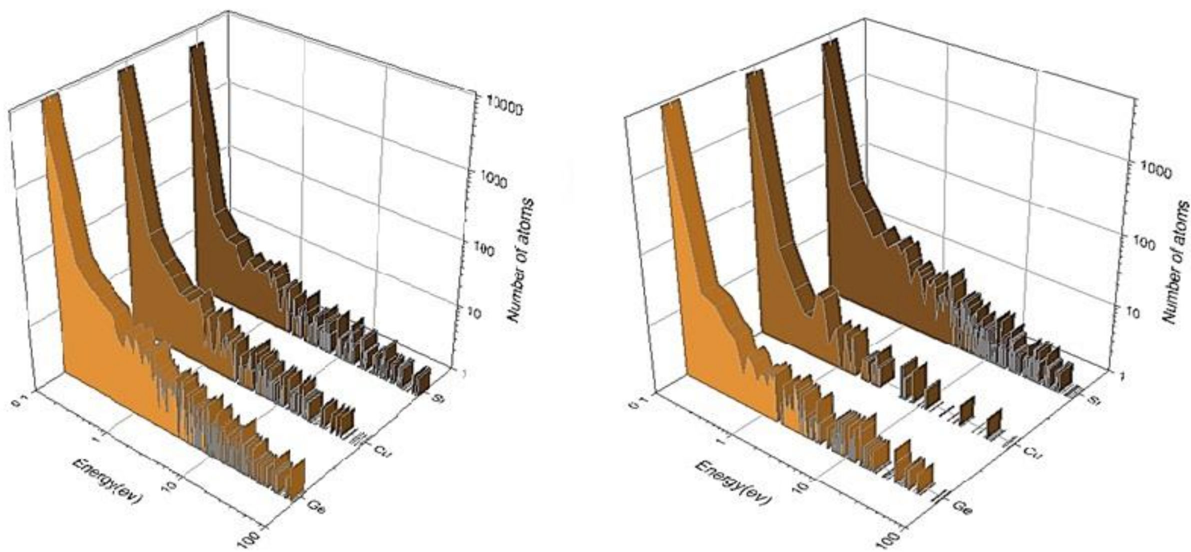

Figure 4.27. Comparison between arriving Si, Ge and Cu atoms as a function of the energy distribution for 2Pa and 300K for a) Argon b) xenon

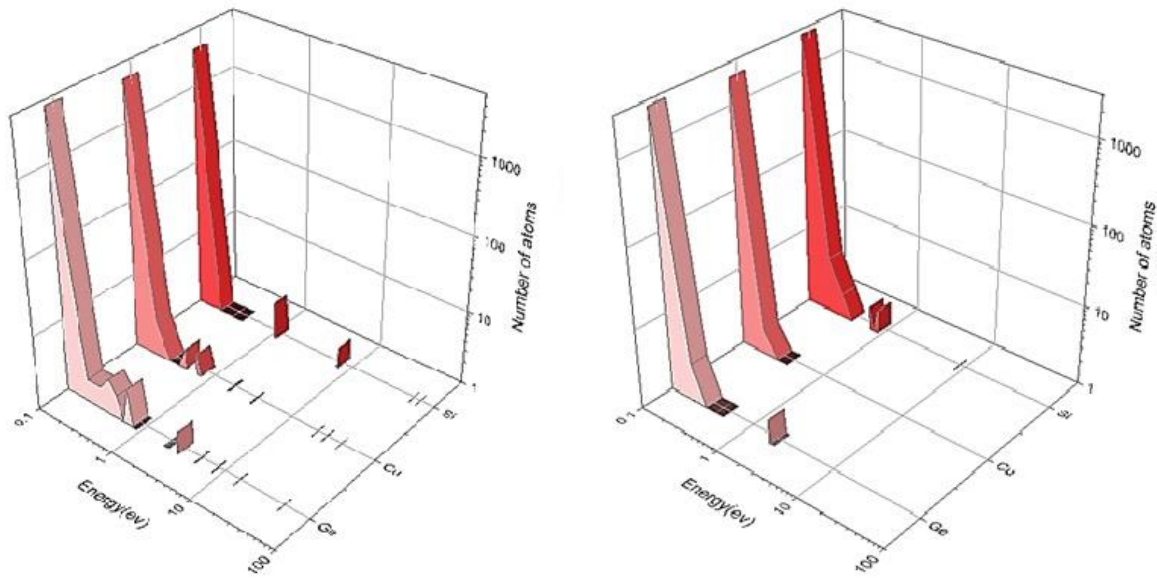

Figure 4.28. Comparison between arriving Si, Ge and Cu atoms as a function of the energy distribution for 5Pa and 300K for a) Argon b) xenon

According to the figures above, a very clear and satisficed results showed that:

1- Ge material gives the best result for arriving at the substrate atoms values followed by Cu and Si in the last position, this means that the Ge semiconductor has better sputtering efficiency than the other materials, in fact, each material can act differently and create a thin layer with different quality and performance.
2- Low pressures (around 0.5 Pa) are successful outcome parameters whenever pressures inside the vacuum chamber decrease the desired thin films will be obtained.
3- oppositely, as much as we go toward the application of higher temperature we will earn the finest thin films morphology.

4.3.4 Analysis of the thin layer created by the deposition of the atoms ejected

The same procedure will be carried out, but this time the vacuum chamber configuration was changed to a dimension of 25cm×25cm×40cm, three different distance (5cm, 8cm, and 14cm) between the target and substrate was taken, the magnetron used has now a circle shape target with a radius of 4cm and the substrate has a 10cmx10cm rectangle shape, we applied a constant temperature, pressure inside the vacuum chamber and 10^4 ions of argon bombarding the semiconductors (Si and Ge) and the metals (Cu and Ag)with an energy value of 1.5kev and an angular incidence of 75 degrees, the objective is to deduce the

influence of the distance on the atoms arriving on the substrate and to see also the thickness of the thin-films built, after all this configuration we can start the simulation.

For this time, we will analyze the deposition of the atoms ejected into the substrate using the materials as targets (Si, Ge, Cu, and Ag).

These figures illustrate the formation of the thin film for each sputtered material at three different distances (5cm, 8cm, and 14cm).

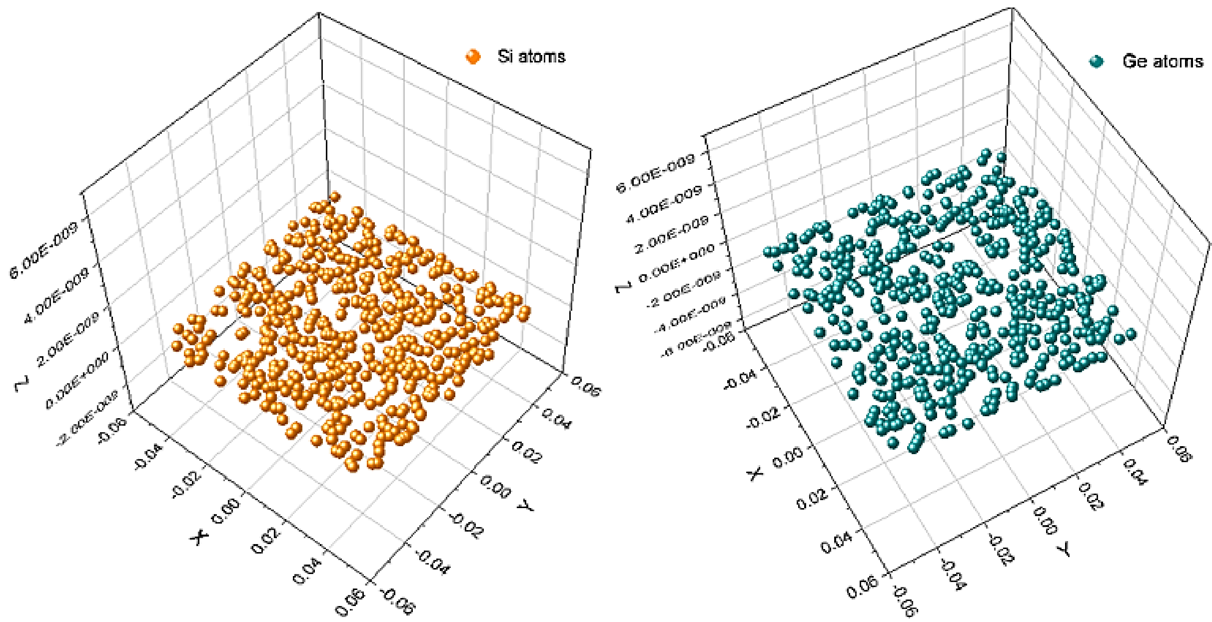

Figure 4.29. Deposition of the atoms ejected on the substrate for the semiconductors (Si and Ge) using 14cm distance

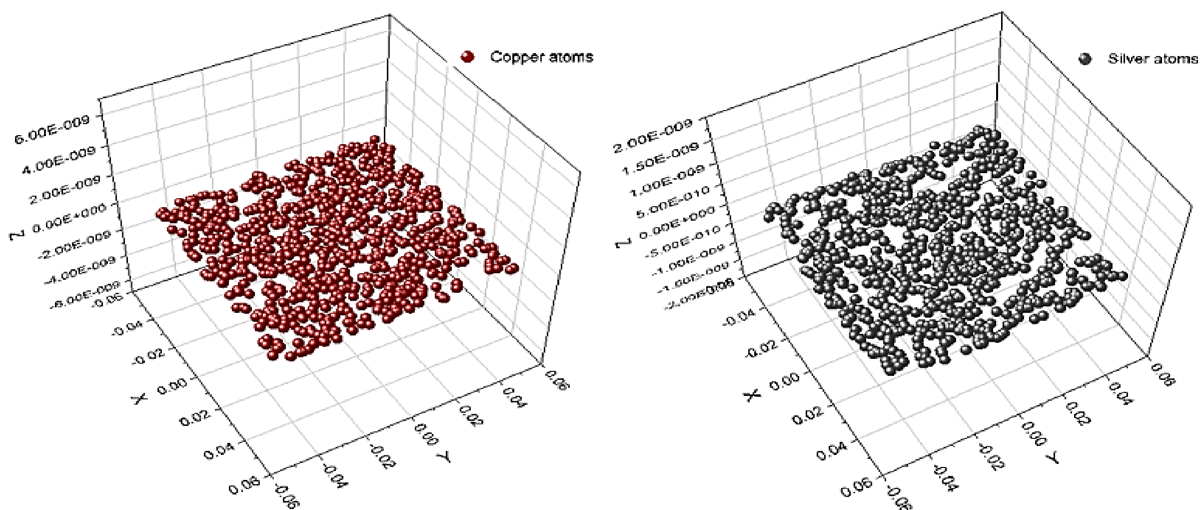

Figure 4.30. Deposition of the atoms ejected on the substrate for the metals (Cu and Ag) using 14cm distance

For each material used we can distinguish an emptiness between the atoms deposited on the substrate, this means that the formed thin layer is not well coated, using a 14cm distance between the target and substrate will lead to a bad coating, a lot of atoms ejected will not reach the substrate due to the high number of collisions that they will face.

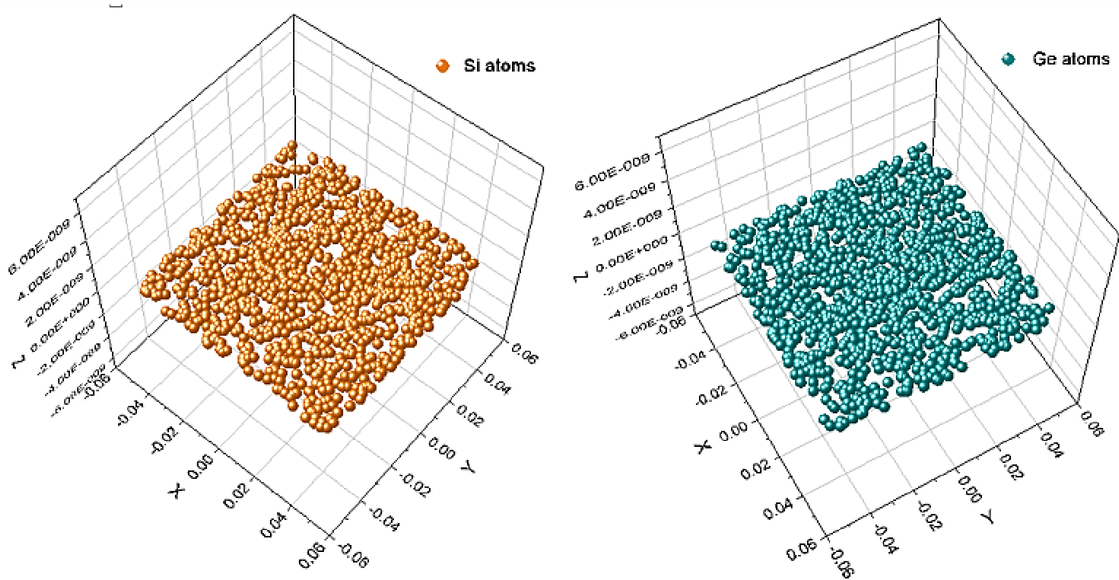

Figure 4.31. Deposition of the atoms ejected on the substrate for the semiconductors (Si and Ge) using 8cm distance

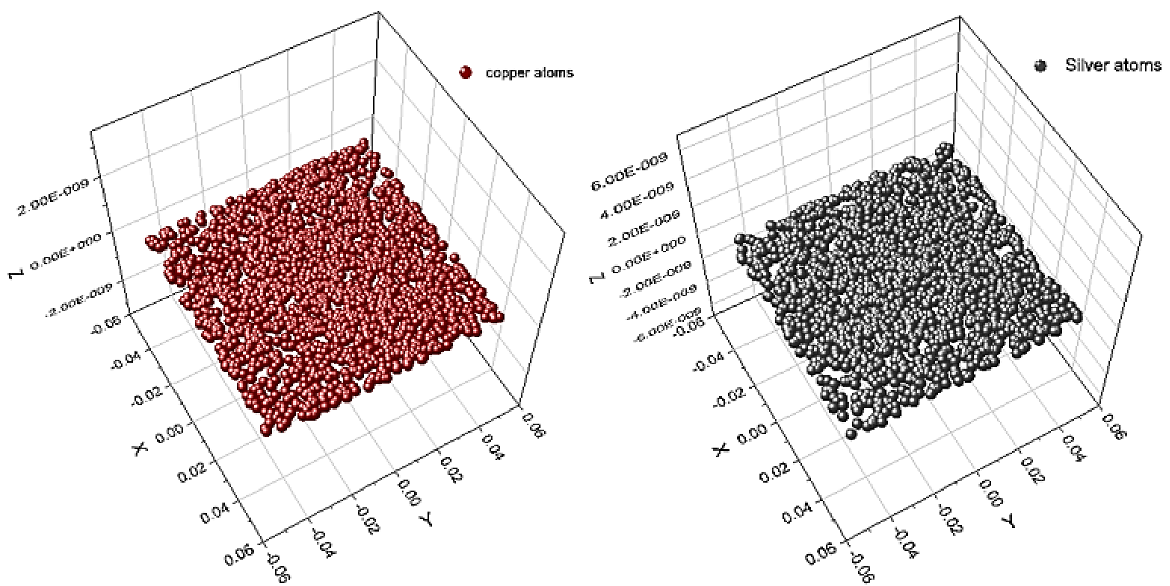

Figure 4.32. Deposition of the atoms ejected on the substrate for the metals (Cu and Ag) using 8cm distance

For this time, we can perceive that by applying a distance of 8cm between the target and the substrate the gap between the atoms begins to fill, we can observe that the coating is better, the thin layer formed may be usable but it still needs more atoms to be deposited to reach the perfect coating.

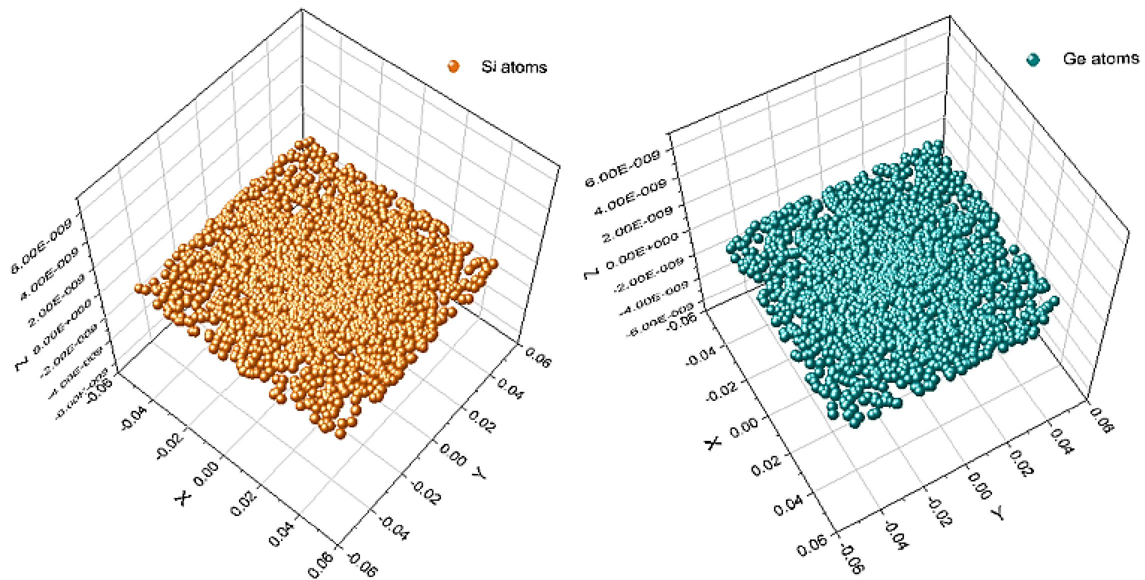

Figure 4.33. Deposition of the atoms ejected on the substrate for the semiconductors (Si and Ge) using 5cm distance

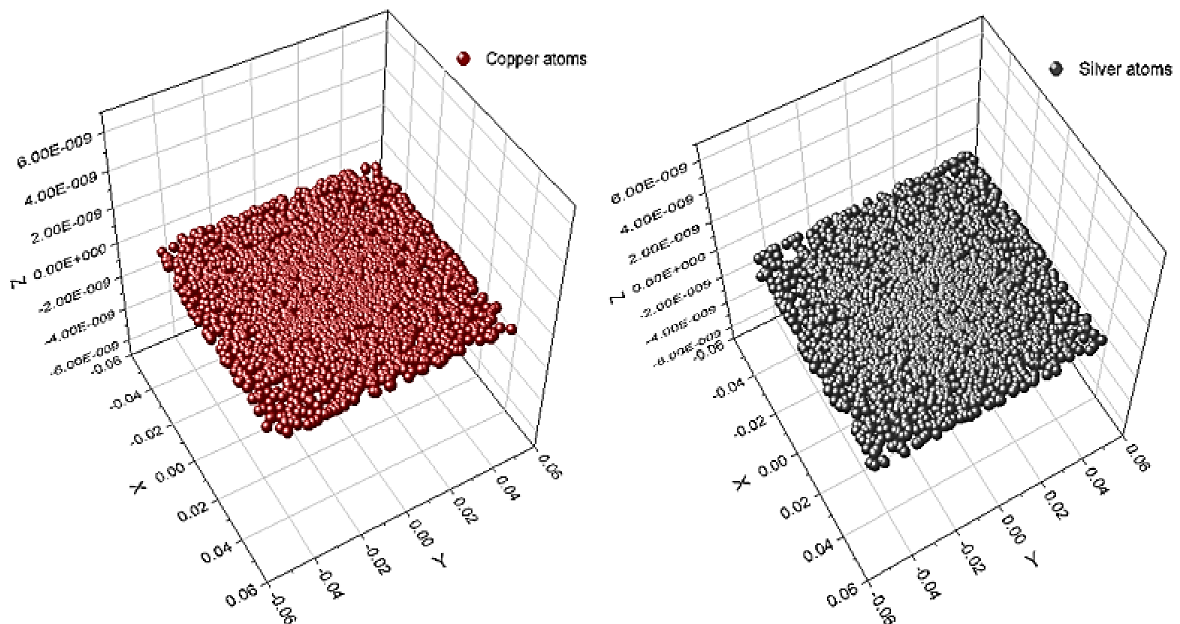

Figure 4.34. Deposition of the atoms ejected on the substrate for the metals (Cu and Ag) using 5cm distance

Now, we can see the thickness on the formed thin layer, there is no void between the atoms, with the use of a 5cm distance between the target and substrate a huge number of atoms ejected will be deposited on the substrate, and the atoms ejected will face less collision which will make them reach the substrate easily, therefor the coating is perfectly done.

Materials	Total number of atoms deposited on the substrate		
	The distance used between target and substrate		
	d= 5cm	d= 8cm	d= 14cm
Si	2417	1197	533
Ge	2118	1213	505
Cu	3324	2003	793
Ag	3072	1762	791

Table 4.6. Total number of atoms deposited on the substrate on each material

From the table, we deduce that the use of the metals as the target gives a better deposition of the sputtered atoms than the semiconductors, with the metal Cu we have obtained more than 3000 atoms deposited on the surface of the substrate which is the best deposition comparing to the other materials.

Widening the distance will cause several problems, a large number of atoms ejected will not survive and won't reach the substrate.

General conclusion

General conclusion

Today, industries use magnetron sputtering extensively to create thin films and coatings for a variety of application areas. It enables the synthesis of dense coatings and an increase in deposition velocity since the magnetic field zone has a greater ionization rate. Thus, this is the method chosen to research developing films due to the many benefits it provides and the potential improvements. Understanding the mechanism of this process is necessary for the study of growing films and in particular for the synthesis of more complex materials. To accomplish this, numerical simulations like SRIM and SIMTRA are among the best models to study this process and support experimental findings.

In order to complete our thesis, we studied the magnetron sputtering method for the deposition of thin films of metals and semiconductors. First, the sputtering yield was calculated using simulations with Monte Carlo codes (SRIM) to study the phenomenon from the beginning. Then, the number of sputtered particles that arrived at the substrate and their energies as a function of the target-substrate distance, temperature, and pressure are calculated by using the second numerical model called (SIMTRA), the study of these previous factors is very important for optimizing the coating of the thin film created.

The outcomes of the first simulation (SRIM) demonstrate that:

- From the obtained results and the first simulation, we observed that the incidence angle (θ_{max}) of 85◦ and the bombardment energy (E_{max}) of 100Kev gives the best sputtering yield which is represented by the amount of ejected atoms for the CZTS and Si semiconductors. If this value of energy or angle is exceeded the sputtering decrease; finally, we found that CZTS gives better results compared to Silicon.
- We deduce from the second simulation that, for the CZTS semiconductor, the presence of sulfide (S4) is very important because it gives a percentage of 45.53% of the total number of the ejected atoms, so it is more efficient than the other elements. For CIGS, we notice that the selenide (Se2) gives a percentage of 57.51% so it outperforms other equipment by far and it plays a major role in achieving good sputtering performance.

These variables θ_{max} and E_{max}, which correspond to the highest number of sputtered particles, are used in the second simulation (SIMTRA), which deals with the transport of these particles from the target to the substrate, so we created a magnetron sputtering system to study the influence of the temperature, pressure and the target-substrate distance.

Results from the second simulation (SIMTRA) show that:

- The growth of temperature values (100, 300, and 600K) offers more kinetic energy to the particles which increase their mobility inside the vacuum chamber and helps an important number of the ejected atoms to arrive on the substrate, so a good temperature adjustment before sputtering is required.
- Conversely, expanding the pressure (0.5, 2, and 5Pa) will diminish the kinetic energy of the particles and hinder their movement by creating more collisions and building a hard path for a significant number of the ejected particles to reach the substrate.
- Eventually, the plasma gas injected inside the vacuum chamber is also considered as a harmful factor, the bad choice of this gas (in our case Xenon ions) will decrease the number of arriving atoms on the substrate so his substitution by the Argon is the best solution.
- applying a long distance will grow the possibility of atoms colliding with each other or between ions which will make a lot of atoms ejected not reaching the substrate.

These results found in our thesis will help to understand the influence of these factors on the deposition of thin films, additionally, our work has now conclusively demonstrated its value and its contribution to the growth of the numerous industries using thin films to create a variety of instruments that are crucial to our everyday lives.

We also hope that our research will contribute to the advancement of the study in this area.

References

References

[1] BOUAZZA Abdelkader, Etude et simulation de l'influence de divers paramètres sur le processus de pulvérisation d'atomes dans un plasma, thèse doctorat, Université des Sciences et de la Technologie d'Oran, 2017.

[2] A. Bouazza and A. Settaouti, "Understanding the contribution of energy and angular distribution in the morphology of thin films using Monte Carlo simulation," Monte Carlo Methods Appl, vol. 24, no. 3, pp. 215-224, (2018), https://doi.org/10.1515/mcma-2018-0019

[3] A. Bouazza and A. Settaouti, "Monte Carlo simulation of the influence of pressure and target-substrate distance on the sputtering process for metal and semiconductor layers," Mod. Phys. Lett. B, vol. 30, no. 20, pp. 1–18, (2016), https://doi.org/10.1142/S0217984916502535

[4] 9. A. Bouazza and A. Settaouti, "Study and simulation of the sputtering process of material layers in plasma," Monte Carlo Methods Appl., vol. 22, no. 2, pp. 149–159, (2016), https://doi.org/10.1515/mcma-2016-0106

[5] 6. S. E. C. Refas, A. Bouazza, and Y. Belhadji, "3D sputtering simulations of the CZTS, Si and CIGS thin films using Monte-Carlo method," Monte Carlo Methods Appl., vol. 27, no. 4, pp. 373–382, (2021), https://doi.org/10.1515/mcma-2021-2094

[6] 5. A. Bouazza, "Sputtering of semiconductors, conductors, and dielectrics for the realization of electronics components thin-films", International Journal of Thin Film Science and Technology, vol. 11, no. 2, pp. 225-232. (2022), https://doi.org/10.18576/ijtfst/110210

[7] L. Sun et al., "Chemical vapour deposition," Nat. Rev. Methods Prim., vol. 1, no. 1, 2021, https://doi.org/10.1038/s43586-020-00005-y

[8] N. Kumari Jangid, S. Jadoun, and N. Kaur, "A review on high-throughput synthesis, deposition of thin films and properties of polyaniline," Eur. Polym. J., vol. 125, no. August 2019, p. 109485, 2020, https://doi.org/10.1016/j.eurpolymj.2020.109485

[9] A. Baptista, F. Silva, J. Porteiro, J. Míguez, and G. Pinto, "Sputtering physical vapour deposition (PVD) coatings: A critical review on process improvement andmarket trend demands," *Coatings*, vol. 8, no. 11, 2018, https://doi.org/10.3390/COATINGS8110402

[10] J. Shi *et al.*, "Chemical Vapor Deposition Grown Large-Scale Atomically Thin Platinum Diselenide with Semimetal-Semiconductor Transition," *ACS Nano*, vol. 13, no. 7, pp. 8442–8451, 2019, https://doi.org/10.1021/acsnano.9b04312

[11] A. Bouazza, "Deposition of Thin Films Materials used in Modern Photovoltaic Cells", International Journal of Thin Film Science and Technology, vol. 11, no. 3, pp. 313-320. (2022), https://doi.org/10.18576/ijtfst/110308

[12] A. Bouazza, "Simulation of the Deposition of Thin-Film Materials Used in the Manufacturing of Devices with Miniaturized Circuits". J. Surf. Investig. vol. 16, no. 6, 1221–1230 (2022). https://doi.org/10.1134/S1027451022060283

[13] B. Liu, M. Fathi, L. Chen, A. Abbas, Y. Ma, and C. Zhou, "Chemical Vapor Deposition Growth of Monolayer WSe2 with Tunable Device Characteristics and Growth

Mechanism Study," ACS Nano, vol. 9, no. 6, pp. 6119–6127, 2015, https://doi.org/10.1021/acsnano.5b01301

[14] A. Baptista, F. J. G. Silva, J. Porteiro, J. L. Míguez, G. Pinto, and L. Fernandes, "On the Physical Vapour Deposition (PVD): Evolution of Magnetron Sputtering Processes for Industrial Applications," Procedia Manuf., vol. 17, pp. 746–757, 2018, https://doi.org/10.1016/j.promfg.2018.10.125

[15] E. Reinhold and J. Faber, "Large area electron beam physical vapor deposition (EB-PVD) and plasma activated electron beam (EB) evaporation - Status and prospects," Surf. Coatings Technol., vol. 206, no. 7, pp. 1653–1659, 2011, https://doi.org/10.1016/j.surfcoat.2011.09.022

[16] P. Panjan, M. Čekada, M. Panjan, and D. Kek-Merl, "Growth defects in PVD hard coatings," *Vacuum*, vol. 84, no. 1, pp. 209–214, 2009, https://doi.org/10.1016/j.vacuum.2009.05.018.

[17] S. Tricot, Comparaison des procédés d'ablation par faisceau laser et par faisceau d'électrons pour la croissance de couches minces, Thèse de doctorat, Université d'Orléans, (2008)

[18] E. Martinez -Guerrero, Elaboration en Epitaxie par Jets Moléculaires des Nitrures d'éléments III en Phase Cubique, Thèse de doctorat, l'institut national des sciences appliquees de lyon, (2002)

[19] H. Morkoç, U. Ozgur, Zinc Oxide : fundamental, Materials and Device Thechnology, WILEY-VCH Verlag GmbH & Co. KGaA, Weinheim, (2009)

[20] M.A.L. Johnson, S. Fujita, W. H. Rowland, W. C. Hughes, J. W. Cook, J. F. Schetzina, MBE growth and properties of ZnO on sapphire and SiC substrates, Journal Of ElectronicMaterials, vol 25, page 855, (1996).

[21] J. P. Bade, E. A. Baker, A. i. Kingon, R. F. Davis, and K. J. Bach mann, Deposition of oxide films by metal-organic molecular-beam epitaxy, Journal of Vacuum Science &Technology B, vol 8, page 327, (1990)

[22] Y. Gui, Mise au point par pulvérisation cathodique magnétron en condition réactive et caractérisations mécaniques et tribologiques de revêtements de phases Magnéli de titane (TinO2n -1) », Thèse de doctorat, Université de Technologie de Belfort-Montbéliard en Matériaux, (2014).

[23] A. Bouazza, "Investigation using Monte-Carlo codes simulations for the impact of temperatures and high pressures on thin films quality". Rev. Mex. Fís., vol. 69, no. 2, 021501 1-12 (2023). https://doi.org/10.1134/S1027451022060283

[24] J. S. Logan, "R.F. diode sputtering," Thin Solid Films, vol. 188, no. 2, pp. 307–321, 1990, https://doi.org/10.1016/0040-6090(90)90293-M

[25] J. H. Ingold, « Anatomy of the discharge », New York, p. 19-64, 1978. [En ligne]. https://ui.adsabs.harvard.edu/abs/1978gael.conf...19I

[26] G. Francis, « The Glow Discharge at Low Pressure », Handbuch der Physik, Berlin–Heidelberg, p. 53-208, 1956. https://ui.adsabs.harvard.edu/abs/1956HDP....22...53F

[27] Plasma-universe.com "Electric glow discharge 2007-2023 https://www.plasma-universe.com/electric-glow-discharge/?title=Torr&action=edit&redlink=1#cite_note-2

[28] J. T. Gudmundsson and D. Lundin, *Introduction to magnetron sputtering*. 2019.

[29] A. Bouazza, " 3D Visualization of the Effect of Plasma Temperature on Thin-Film Morphology". Bull. Lebedev Phys. Inst., vol. 50, no. 1, 7-13 (2023). https://doi.org/10.1134/S1027451022060283

[30] K. Seshan, Handbook of thin film deposition processes and techniques, William Andrew Publishing, Norwich, EUA, 2002; .

[31] N. K. Jain, M. Sawant, and S. H. Nikam, "Metal Deposition: Plasma-Based Processes," Encycl. Plasma Technol., no. September 2020, pp. 722–740, 2017, doi: 10.1081/e-eplt-120053919;

[32] M. Ohring, The Materials Science of Thin Films, Academic Press Inc., San Diego, 1992;

[33] Van de Pol, F. C. M.; Blom, F.R.; Popma, J.A. R.F. planar magnetron sputtered ZnO films I: structural properties. Thin Solid Films, v. 204, p. 349-364, 1991;

[34] C. A. Bishop, Vacuum Deposition onto Webs, Films and Foils (Second Edition), 20 - Magnetron Sputtering Source Design and Operation, 2011;

[35] Fardeheb-Mammeri Amina-Zahia, dépôt par pulverisation magnetron de couches minces de nitrure d'aluminium a axe c incline en vue de la realisation des dispositifs a ondes acoustiques vibrant en mode de cisaillement, Thèse de doctorat, Université abou bekr belkaid tlemcen et l'Universite Henri Poinca re Nancy-i, (2009).

[36] J. A. Thornton. Influence of apparatus geometry and deposition conditions on structure and topography of thick sputtered coatings. Journal of Vacuum Science & Technology 11 (1974) 666-670;

[37] O. Kluth et al. Modified Thornton model for magnetron sputtered zinc oxide: film structure and etching behavior. Thin Solid Films 442 (2003) 80-85;

[38] I. Langmuir, « The Effect of Space Charge and Initial Velocities on the Potential Distribution and Thermionic Current between Parallel Plane Electrodes », Phys. Rev., vol. 21, no 4, p. 419-435, avr. 1923, https://doi.org/10.1103/PhysRev.21.419

[39] J. T. Gudmundsson, « Ionized physical vapor deposition (IPVD): magnetron sputtering discharges », J. Phys. Conf. Ser., vol. 100, no 8, p. 082002, mars 2008, https://doi.org/10.1088/1742-6596/100/8/082002

[40] I. A. Abroyan, M. A. Eremeev, et N. N. Petrov, « EXCITATION OF ELECTRONS IN SOLIDS BY RELATIVELY SLOW ATOMIC PARTICLES », Sov. Phys. Uspekhi, vol. 10, no 3, p. 332-367, mars 1967, https://doi.org/10.1070/pu1967v010n03abeh003250

[41] Hasselkamp D., Rothard H., Groeneveld KO., Kemmler J., Varga P., Winter H., « Kinetic electron emission from solid surfaces under ion bombardment. », in Particle Induced Electron Emission II. Springer Tracts in Modern Physics, Springer., 123 vol., Berlin: Heidelberg, 2006.

[42] Baragiola, R.A., Alonso, E.V., Ferron, J., et Oliva-Florio, A., « Ion-induced electron emission from clean metals », Surface Science, Netherlands, p. 240-255, 1979. [En ligne].

[43] A. Anders, J. Andersson, et A. Ehiasarian, « High power impulse magnetron sputtering: Current-voltage-time characteristics indicate the onset of sustained selfsputtering », J. Appl. Phys., vol. 102, no 11, p. 113303, déc. 2007, https://doi.org/10.1063/1.2817812

[44] M. A. Lieberman and A. J. Lichtenberg, Principles of Plasma Discharges and Materials Processing, John Wiley&Sons Inc., New Jersey. 2005.

[45] J. E. Allen, « The plasma–sheath boundary: its history and Langmuir's definition of the sheath edge », Plasma Sources Sci. Technol., vol. 18, no 1, p. 014004, nov. 2008, https://doi.org/10.1088/0963-0252/18/1/014004

[46] R. N. Franklin, « The plasma–sheath boundary region », J. Phys. Appl. Phys., vol. 36, no 22, p. R309-R320, oct. 2003, https://doi.org/10.1088/0022-3727/36/22/r01

[47] A. Anders, J. Andersson, D. Horwat, et A. Ehiasarian, « Physics of high power impulse magnetron sputtering », janv. 2007.

[48] D.M. Mattox, "Physical vapor deposition (PVD) processes", Metal Finishing 97 (1999) 417-430.

[49] P.J. Kelly, R.D. Arnell, "Magnetron sputtering: a review of recent developments and applications", Vacuum 56 (2000) 159-172.

[50] D.S. Veselov, Y.A. Voronov, K.D. Vanyukhin, "Researching of dielectric membrane films obtained by reactive magnetron sputtering", Physics Procedis 72 (2015) 495-499.

[51] P.J. Kelly, P.S. Henderson, R.D. Arnell, G.A. Roche, D. Carter, "Reactive pulsed magnetron sputtering process for alumina films", Journal of Vacuum Science and Technology A 18 (2000) 2890-2896.

[52] A. Billard, F. Perry, "Pulvérisation cathodique magnétron", Techniques de l'Ingénieur, M 1 654 1-17

[53] V. Kouznetsov, K. Macák, J. M. Schneider, U. Helmersson, et I. Petrov, « A novel pulsed magnetron sputter technique utilizing very high target power densities », Surf. Coat. Technol., vol. 122, no 2-3, p. 290-293, déc. 1999, https://doi.org/10.1016/S0257-8972(99)00292-3

[54] D. Lundin et K. Sarakinos, « An introduction to thin film processing using high-power impulse magnetron sputtering », J. Mater. Res., vol. 27, mars 2012, https://doi.org/10.1557/jmr.2012.8

[55] A. P. Ehiasarian, R. New, W.-D. Münz, L. Hultman, U. Helmersson, et V. Kouznetsov, « Influence of high power densities on the composition of pulsed magnetron plasmas », IUVSTA Highlights Semin., vol. 65, no 2, p. 147-154, avr. 2002, https://doi.org/10.1016/S0042-207X(01)00475-4

[56] A. P. Ehiasarian, W.-D. Münz, L. Hultman, U. Helmersson, et I. Petrov, « High power pulsed magnetron sputtered CrNx films », Proc. 29th Int. Conf. Metall. Coat. Thin Films, vol. 163-164, p. 267-272, janv. 2003, https://doi.org/10.1016/S0257-8972(02)00479-6

[57] S. Konstantinidis, J. P. Dauchot, M. Ganciu, A. Ricard, et M. Hecq, « Influence of pulse duration on the plasma characteristics in high-power pulsed magnetron discharges », J. Appl. Phys., vol. 99, no 1, p. 013307, janv. 2006, https://doi.org/10.1063/1.2159555

[58] V. S. Voitsenya *et al.*, "Effect of sputtering on self-damaged recrystallized W mirror specimens," *J. Nucl. Mater.*, vol. 434, no. 1–3, pp. 375–381, 2013, https://doi.org/10.1016/j.jnucmat.2012.12.007

[59] H. van Lente and J. I. van Til, "Articulation of sustainability in the emerging field of nanocoatings," *J. Clean. Prod.*, vol. 16, no. 8–9, pp. 967–976, 2008,

https://doi.org/10.1016/j.jclepro.2007.04.020

[60] G. Hobler, R. M. Bradley, and H. M. Urbassek, “Probing the limitations of Sigmund’s model of spatially resolved sputtering using Monte Carlo simulations,” *Phys. Rev. B*, vol. 93, no. 20, pp. 1–17, 2016, https://doi.org/10.1103/PhysRevB.93.205443

[61] H. Hofsäss and O. Bobes, “Prediction of ion-induced nanopattern formation using Monte Carlo simulations and comparison to experiments,” *Appl. Phys. Rev.*, vol. 6, no. 2, 2019, https://doi.org/10.1063/1.5043188.

[62] U. H. Kwon, S. H. Choi, Y. H. Park, and W. J. Lee, ‘Multi-scale simulation of plasma generation and film deposition in a circular type DC magnetron sputtering system’, Thin Solid Films, vol. 475, no. 1–2, pp. 17–23, Mar. 2005.

[63] J. Kageyama, M. Yoshimoto, A. Matsuda, Y. Akao, and E. Shidoji, ‘Numerical simulation of plasma confinement in DC magnetron sputtering under different magnetic fields and anode structures’, Jpn. J. Appl. Phys., vol. 53, no. 8, p. 088001, Jul. 2014.

[64] Virginia Polytechnic Institute. "Monte Carlo Simulation.

" https://sites.google.com/a/vt.edu/monte-carlo-simulation/history".

[65] S. Rubenthaler, “Syllabus: Méthodes de Monte-Carlo,” pp. 2018–2019, 2019.

[66] E. Bultinck and A. Bogaerts, ‘Characterization of an Ar/O 2 magnetron plasma by a multi-species Monte Carlo model’, Plasma Sources Sci. Technol., vol. 20, no. 4, p. 045013, 2011.

[67] S. Kondo and K. Nanbu, ‘A self-consistent numerical analysis of a planar dc magnetron discharge by the particle-in-cell/Monte Carlo method’, J. Phys. Appl. Phys., vol. 32, no. 10, pp. 1142–1152, Jan. 1999.

[68] C. Costin, L. Marques, G. Popa, and G. Gousset, ‘Two-dimensional fluid approach to the dc magnetron discharge’, Plasma Sources Sci. Technol., vol. 14, no. 1, p. 168, 2005.

[69] C. K. Birdsall, ‘Particle-in-cell charged-particle simulations, plus Monte Carlo collisions with neutral atoms, PIC-MCC’, IEEE Trans. Plasma Sci., vol. 19, no. 2, pp. 65–85, Apr. 1991.

[70] K. Nanbu, S. Segawa, and S. Kondo, ‘Self-consistent particle simulation of three-dimensional dc magnetron discharge’, Vacuum, vol. 47, no. 6, pp. 1013–1016, Jun. 1996.

[71] K. Nanbu and S. Kondo, ‘Analysis of three-dimensional DC magnetron discharge by Particle-inCell/Monte Carlo Method’, Jpn. J. Appl. Phys., vol. 36, pp. 4808–4814, 1997.

[72] C. H. Shon and J. K. Lee, ‘Modeling of magnetron sputtering plasmas’, Appl. Surf. Sci., vol. 192, no. 1– 4, pp. 258–269, May 2002.

[73] F. Guimaraes and J. Bretagne, ‘Study of an argon magnetron discharge used for molybdenum sputtering. I. Collisional radiative model’, Plasma Sources Sci. Technol., vol. 2, no. 3, pp. 127–137, Aug. 1993.

[74] W. Trennepohl, J. Bretagne, G. Gousset, D. Pagnon, and M. Touzeau, ‘Modelling of an reactive magnetron discharge used for deposition of chromium oxide’, Plasma Sources Sci. Technol., vol. 5, no. 4, pp. 607–621, Nov. 1996.

[75] C. Costin, Modélisation d’une décharge magnétron DC dans l’argon et en mélanges argon-oxygène par un modèle fluide. Paris 11, 2005.

[76] C. Costin, G. Gousset, and G. Popa, ‘Modélisation d’une décharge magnétron dc dans l’Argon par un modèle fluide’, Le Vide, vol. 57, no. 304, pp. 308–315, 2002.

[77] I. Kolev and A. Bogaerts, ‘Numerical Models of the Planar Magnetron Glow Discharges’, Contrib. Plasma Phys., vol. 44, no. 7–8, pp. 582–588, 2004.

[78] E. Shidoji, K. Ness, and T. Makabe, ‘Influence of gas pressure and magnetic field upon dc magnetron discharge’, Vacuum, vol. 60, no. 3, pp. 299–306, Mar. 2001.

[79] Jimenez, F., Ekpe, S. D., and Dew, S. K., ‘Modeling of Low Pressure Magnetron Plasma Discharge’, Excerpt Proc. COMSOL Conf. 2007 Boston.

[80] W. Eckstein, ‘Sputtering Yields’, in Sputtering by Particle Bombardment: Experiments and Computer Calculations from Threshold to MeV Energies, Berlin, Heidelberg: Springer Berlin Heidelberg, 2007, pp. 33–187.

[81] J. Stark, Die elektrizität in gasen. J.A. Barth, 1902.

[82] P. Sigmund, ‘Mechanisms and theory of physical sputtering by particle impact’, Nucl. Instrum. Methods Phys. Res. Sect. B Beam Interact. Mater. At., vol. 27, no. 1, pp. 1–20, Jun. 1987.

[83] R. Behrisch and W. Eckstein, Sputtering by Particle Bombardment: Experiments and Computer Calculations from Threshold to MeV Energies. Springer Science & Business Media, 2007.

[84] G. Falcone, ‘Theory of collisional sputtering’, Surf. Sci., vol. 187, no. 1, pp. 212–222, Aug. 1987.

[85] P. Sigmund, ‘Theory of Sputtering. I. Sputtering Yield of Amorphous and Polycrystalline Targets’, Phys. Rev., vol. 184, no. 2, pp. 383–416, Aug. 1969.

[86] W. Eckstein and H. M. Urbassek, ‘Computer Simulation of the Sputtering Process’, in Sputtering by Particle Bonbardment, vol. 110, Springer, Berlin, Heidelberg, 2007, pp. 22–31.

[87] W. Möller, W. Eckstein, and J. P. Biersack, ‘Tridyn-binary collision simulation of atomic collisions and dynamic composition changes in solids’, Comput. Phys. Commun., vol. 51, no. 3, pp. 355–368, Nov. 1988.

[88] L. Bukonte, F. Djurabekova, J. Samela, K. Nordlund, S. A. Norris, and M. J. Aziz, ‘Comparison of molecular dynamics and binary collision approximation simulations for atom displacement analysis’, Nucl. Instrum. Methods Phys. Res. Sect. B Beam Interact. Mater. At., vol. 297, pp. 23–28, Feb. 2013.

[89] Y. Yamamura and W. Takeuchi, ‘Monocrystal sputtering by the computer simulation code acoct’, Nucl. Instrum. Methods Phys. Res. Sect. B Beam Interact. Mater. At., vol. 29, no. 3, pp. 461–470, Dec. 1987.

[90] Y. Yamamura, ‘Sputtering by cluster ions’, Nucl. Instrum. Methods Phys. Res. Sect. B Beam Interact. Mater. At., vol. 33, no. 1, pp. 493–496, Jun. 1988.

[91] A. Mutzke, W. Eckstein, R. Schneider, and R. Dohmen, ‘SDTrimSP: Version 5.00’, IPP Rep., 2011.

[92] S. Plimpton, ‘Fast Parallel Algorithms for Short-Range Molecular Dynamics’, J. Comput. Phys., vol. 117, no. 1, pp. 1–19, Mar. 1995.

[93] P. Brault, S. Chuon, and J.-M. Bauchire, 'Molecular Dynamics Simulations of Platinum Plasma Sputtering: A Comparative Case Study', Plasma Phys., p. 20, 2016.

[94] E. C. Neyts and P. Brault, 'Molecular Dynamics Simulations for Plasma-Surface Interactions', Plasma Process. Polym., vol. 14, no. 1–2, p. 1600145, 2017.

[95] M. W. Thompson, 'Physical mechanisms of sputtering', Phys. Rep., vol. 69, no. 4, pp. 335–371, Mar. 1981.

[96] A. Billard and F. Perry, Pulverisation cathodique magnetron. Ed. Techniques Ingénieur.

[97] Y. Yamamura and J. Bohdansky, 'Few collisions approach for threshold sputtering', Vacuum, vol. 35, no. 12, pp. 561–571, Dec. 1985

[98] Y. Yamamura, 'Theory of sputtering and comparison to experimental data', Nucl. Instrum. Methods Phys. Res., vol. 194, no. 1–3, pp. 515–522, Mar. 1982.

[99] Y. Yamamura and H. Tawara, 'Energy dependence of ion-induced sputtering yields from monatomic solids at normal incidence', At. Data Nucl. Data Tables, vol. 62, no. 2, pp. 149–253, Mar. 1996.

[100] W. Eckstein and R. Preuss, 'New fit formulae for the sputtering yield', J. Nucl. Mater., vol. 320, no. 3, pp. 209–213, Aug. 2003.

[101] D. Depla, Magnetrons, reactive gases and sputtering (2014).

[102] M. W. Thompson, "II. The energy spectrum of ejected atoms during the high energy sputtering of gold", Philosophical Magazine 18, 377–414 (1968).

[103] R. A. Baragiola, E. V. Alonso, J. Ferron and A. Oliva-Florio, "Ion-induced electron emission from clean metals", Surface Science 90, 240–255 (1979).

[104] D. Depla, S. Mahieu and R. De Gryse, "Magnetron sputter deposition: Linking discharge voltage with target properties", Thin Solid Films 517, 2825–2839 (2009).

[105] A. Anders, J. Andersson and A. Ehiasarian, "High power impulse magnetron sputtering: Current-voltage-time characteristics indicate the onset of sustained self-sputtering", Journal of Applied Physics 102, 113303 (2007)

[106] U. Saha, K. Devan, and S. Ganesan, "A study to compute integrated dpa for neutron and ion irradiation environments using SRIM-2013," *J. Nucl. Mater.*, vol. 503, pp. 30–41, 2018, https://doi.org/10.1016/j.jnucmat.2018.02.039

[107] M. El Marsi, R. Moultif, S. Lahlou, S. Rochd, and A. Dezairi, "Monte Carlo simulations of MgO and Mg(OH)2 thin films sputtering yields by noble-gas ion bombardment in plasma display panel PDP," *Nucl. Instruments Methods Phys. Res. Sect. B Beam Interact. with Mater. Atoms*, vol. 430, no. May, pp. 72–78, 2018, https://doi.org/10.1016/j.nimb.2018.05.046

[108] J. O. Achenbach, S. Mráz, D. Primetzhofer, and J. M. Schneider, "Correlative experimental and theoretical investigation of the angle-resolved composition evolution of thin films sputtered from a compound Mo2BC target," *Coatings*, vol. 9, no. 3, 2019, https://doi.org/10.3390/COATINGS9030206

[109] D. Depla, "SIMTRA - User Manual," no. February, pp. 1–19, 2016.

Annex

Annex

the choice of materials used

Our aim is to apply this model to materials widely used in industry today, such as the manufacture of modern photovoltaic cells, in order to deduce the best parameters which will then give us the best yield, the highest quantity of particles sputtered.

In the second part of our work, we use the second software package (SIMTRA) to simulate the transport of sputtered particles to the substrate. As this software is somewhat limited (it does not take composite materials into account), and as the main objective of this thesis is to deduce the effect of different parameters on the deposition of particles at the substrate, we have applied the model to different materials such as semiconductors and metals, also widely used in modern industry.

The main objective of this work to contribute to research in the field of sputtering deposition with the provision of optimal parameters is achieved, the choice of materials is based just on diversity and novelty.

Software legitimation

SRIM and SIMTRA are widely used in the field of thin-film manufacturing, and more specifically in the application of the sputtering process. As a result, many researchers have been attracted to this field of research, and numerous works have been published. These include the work of

H. Hofsäss et al [1], A. Bouazza et al [2], M. P. Seah [3] and the most recently published (in 2022) by N. Mahne et al [4]. These groups of researchers have published benchmark works for the application of SRIM and comparison with modeling through the equations of Sigmund, Yamamura and Thomson, proving the effectiveness of this software in calculating the sputtering rate. Similarly, works based on simulations by the SIMTRA code, such as those by D. Depla et al [5,6], R. De Gryse [7], A. Bouazza [8], are considered as reference works, as they show the efficiency of this software through comparisons with theoretical and experimental studies

Potential contributions that this research work can make in relation to these earlier works using SRIM and SIMTRA could include:

Use of new materials: study the interaction of ions with materials that have not previously been studied with these software packages (materials used in modern industry), thus providing new information on the properties and distribution of ions in these materials.

Further analysis of the results: present a more detailed analysis of the simulation results obtained using SRIM and SIMTRA, examining specific aspects such as the influence of various parameters such as energy, angle of incidence, nature of the gas, nature of the materials used, pressure and temperature on the structure of the material at substrate level.

Visualization of results in the form of 3D graphs: this makes it easier to understand the models, with graphs that are very clear compared with previous results.

[1] https://doi.org/10.3390/coatings12101541

[2] https://doi.org/10.1515/mcma-2016-0106

[3] https://doi.org/10.1088/0022-3727/43/25/253001

[4] https://doi.org/10.3390/coatings12101541

[5] https://doi.org/10.1016/j.tsf.2012.06.032

[6] https://doi.org/10.1016/j.tsf.2019.05.045

[7] https://doi.org/10.1016/j.tsf.2012.04.065

[8] https://doi.org/10.1142/S0217984916502535

Mathematical description of the transport of sputtered atoms to the substrate

To simulate the entire trajectory of an atom, we need the emission conditions (coordinates of the emission point, direction of ejection, initial energy, etc.) as well as the transfer through the chamber (series of free trajectories and collisions leading to a change in direction and energy). It is assumed that ejected particles collide only with argon atoms (and not with other ejected particles). This assumption is justified because the concentration of ejected particles is low compared with the concentration of the ambient gas under the conditions used. The gas density is uniform in the space between the targets and the substrate. The energy and angle distribution of the ejected atoms (emission from the targets) is assumed to obey the theoretical Sigmund-Thompson distribution [1].

$$f(E,\beta)=\frac{2UE}{(E+U)^3}\frac{\cos(\beta)}{\pi}$$

where U is the surface binding energy of the target material, mostly taken equal to the sublimation energy, and β is the angle of the velocity vector with respect to the axial direction. The specific angle and energy of a sputtered atom starting at the target are calculated from the above equation using two random numbers (R1, R2) uniformly distributed between 0 and 1.[2]

Simulation of atom transport in a sputtering system.

$$R_1(\beta)=\int_0^{\infty}\int_0^{\beta}2\pi\cdot\sin(\beta)\cdot f(E,\beta)\cdot dE\cdot d\beta$$
$$R_2(E)=\int_0^{E}\int_0^{\pi/2}2\pi\cdot\sin(\beta)\cdot f(E,\beta)\cdot dE\cdot d\beta$$

which leads to

$$\beta=(1/2)\arccos(1\text{-}2R_1)$$
$$E^2(R_2\text{-}1)+E(2UR_2)+U^2R_2=0$$

where the positive roots give E. The azimuthal ejection angle φ (angle of the projection of the velocity vector in the xy plane, with respect to the x axis) is generated uniformly between 0 and 2π by a random number R3 between 0 and 1,

$$\phi=2\pi\cdot R_3.$$

No correlation has been made between the ejection angle and energy. The x and y coordinates of the starting position are also determined by random number R4 such that

$$x=R_4\sin(\phi)$$
$$y=R_4\cos(\phi)$$

To calculate the gas-phase transport processes of an ejected particle, the Monte-Carlo method was used. For each atom, we simulated its trajectory by calculating the free path between the ejection point and the first collision point, then between two successive collisions using the collision parameters (impact parameter, deflection of the ejected atom, energy loss). The motion of ambient gas atoms is neglected in relation to the high kinetic energies of the ejected particles. Therefore, the mean free path λ_m of the sputtered atom is obtained by [3]:

$$\lambda_m=\frac{k_BT}{r_{sg}^2\pi\cdot p}$$

where k_B is the Boltzmann constant, T the temperature of the sputtering gas taken as 350 K, p the pressure of the sputtering gas, and r_{sg} is the interatomic separation of the sputtered atom and working gas atom (sum of atomic radii). In the Monte Carlo approach, the distance λ a particle travels between two successive collisions correlates with the mean free path λ_m by

$$\lambda = -\lambda_m \ln(R_5)$$

where R5 is a random number of the interval {0,1}. After each λ_i, the metallic atom undergoes a collision with a background gas atom. The scattering process itself was modelled by a hard sphere collision approach with an energy-dependent value for r_{sg}. To evaluate r_{sg}, a Born-Mayer type interatomic potential has been used. Abrahamson calculated the repulsive part of the potential atom-atom potential, expressing the different potentials. Within these limits, the diffusion potential has the Born-Mayer form [4].

$$V(r) \approx (A_s A_g)^{0.5} \exp\left| -\left(\frac{b_s + b_g}{2}\right) . r \right|$$

where As, bs, Ag, and bg are the Born-Mayer parameters for the sputtered and the background gas atoms

Neglecting the thermal motion of the background gas atoms, the minimal interatomic separation r_{sg} of the sputtered atom and the colliding gas atom for a central collision with the Es kinetic energy of the sputtered atom

$$r_{sg} = r_s + r_g \approx -\frac{2}{b_s + b_g} \ln \frac{E_s}{(A_s A_g)^{1/2}}$$

has been used for the calculation of the mean free path. As the pressure increases, the mean free path decreases, leading to collision of the ejected particle with the gas molecules. Each collision results in a change in the direction of the ejected particle and loss of energy. According to the hard sphere collision model that is used to study the trajectory of the ejected particle, the scattering angle χ with respect to the laboratory frame of reference and the energy loss rate κ is given by,

$$\tan\chi = \frac{\sin\chi_{com}}{m_1/m_2 + \cos\chi_{com}},$$

$$\kappa = \frac{(m_1 - m_2)^2 \cos^2\theta + (m_1 + m_2)^2 \sin^2\theta}{(m_1 + m_2)^2},$$

$$\chi_{com} = \pi - 2\theta,$$

where m_1 and m_2 are the masses of sputtered and the background gas atoms, respectively, and θ is the angle between the line that passes through the centers of a sputtered atom and the background gas atom on collision and the direction of velocity of the sputtered atom before collision. θ and the azimuthal angle of scattering ψ are determined by a random number R_6:

$$\theta = \arcsin(R_6)^{1/2}$$
$$\psi = 2\pi \cdot R_6.$$

The new direction in three-dimensional space, the new angles θ and φ, are calculated from the angles $\theta 0$ and $\varphi 0$ before scattering, as well as the scattering angle χ and the scattering azimuth angle ψ, by transformation of the coordinate reference system.

After the new energy and direction have been determined, the atom is tracked in the next step, and the procedure is repeated. The recurrent calculation is repeated until the ejected atom slows down to an energy less than or equal to the average thermal energy of the surrounding gas.

[1] P. Sigmund, Top. Appl. Phys. 47 9 (1981).

[2] Thompson, M. W., Philosophical Magazine, 18 152 (1968).

[3] Ronald A. Powell, Stephen M. Rossnagel, Thin Films, 26 241 (1999)

[4] A.A. Abrahamson, Phys. Rev. 178 (1969).

[5] G. J. Boyle et al., The Journal of Chemical Physics 142.15 (2015)

The structural properties of the Materials Si, CIGS and CZTS

a) the Silicon (Si):

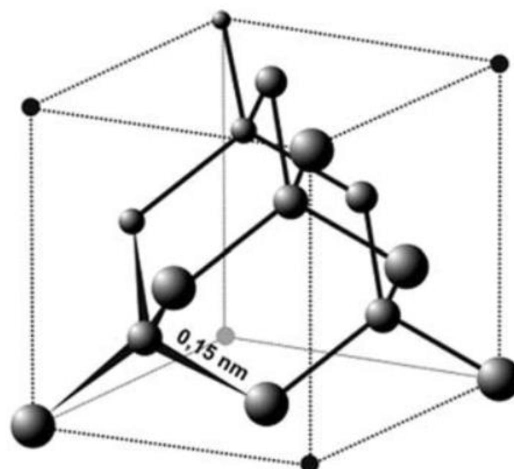

figure.1; Crystalline structure of silicon [1]

Silicon is a chemical element with the symbol Si and atomic number 14. It is a metalloid, meaning it has properties of both metals and non-metals. Here are some key properties of the silicon structure:

1. Crystal Structure: Silicon has a crystalline structure, specifically a diamond cubic crystal structure. Each silicon atom is bonded to four neighboring silicon atoms, forming a three-dimensional lattice.
2. Hardness: Silicon is a relatively hard material with a Mohs hardness of 7. This means it is harder than most minerals but softer than materials like diamond or corundum.
3. Melting Point: Silicon has a high melting point of 1,414 degrees Celsius (2,577 degrees Fahrenheit). This makes it suitable for applications in high-temperature environments.
4. Electrical Conductivity: Silicon is a semiconductor, which means it has intermediate electrical conductivity between conductors and insulators. Its conductivity can be modified by introducing impurities or "doping" the material.
5. Thermal Conductivity: Silicon has a relatively high thermal conductivity, allowing it to efficiently transfer heat. This property makes it useful in applications where heat dissipation is important, such as computer chips.
6. Optical Properties: Silicon has a wide transparency range in the infrared region, making it useful for infrared optics and detectors. However, it is opaque to visible light.
7. Chemical Reactivity: Silicon is generally stable and does not react with most acids, except for highly concentrated and hot hydrofluoric acid. It forms a protective oxide layer (silicon dioxide) on its surface when exposed to oxygen, which gives it corrosion resistance.
8. Abundance: Silicon is the second most abundant element in the Earth's crust after oxygen, making up about 28% of its composition by weight.

These are some of the fundamental properties of the silicon structure that contribute to its wide range of applications in electronics, solar cells, integrated circuits, and other technological fields.

b) **the CIGS composite material**

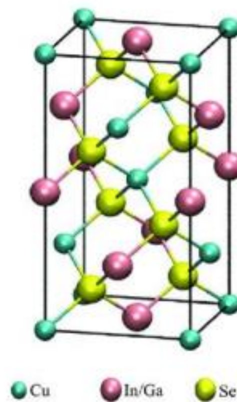

figure.2 crystalline structure of CIGS [2]

CIGS, or Copper Indium Gallium Selenide, is another compound semiconductor material that is widely used in thin-film solar cells. Here are the key structural properties of CIGS:

1. Crystal Structure: CIGS has a chalcopyrite crystal structure, which belongs to the tetragonal crystal system. The lattice parameters vary depending on the composition and synthesis conditions.
2. Composition: CIGS is composed of copper (Cu), indium (In), gallium (Ga), and selenium (Se) elements. The typical stoichiometry is Cu(In,Ga)Se2, where the ratio of Cu, In, Ga, and Se can vary to achieve different properties.
3. Band Gap: CIGS is a direct bandgap semiconductor material, with its bandgap energy typically ranging from 1.0 to 1.7 eV. The bandgap can be controlled by adjusting the ratio of indium and gallium within the material.
4. Electrical Conductivity: CIGS is a p-type semiconductor, meaning it has a predominance of positively charged holes as charge carriers. The electrical conductivity of CIGS is influenced by its composition, crystal structure, and dopant concentration.
5. Optical Properties: CIGS exhibits excellent light absorption properties, allowing it to efficiently convert sunlight into electricity. It has a high absorption coefficient, especially in the visible and near-infrared regions of the electromagnetic spectrum.
6. Defects and Dopants: CIGS crystals can contain various defects and impurities, which can affect the material's properties. The addition of dopants like sodium (Na) can improve the carrier concentration and enhance device performance.

7. Thin Film Deposition: CIGS thin films can be synthesized using various techniques, including co-evaporation, sputtering, or electrodeposition. The deposition process plays a crucial role in achieving high-quality CIGS films with the desired composition and structure.

CIGS has gained significant attention in the field of photovoltaics due to its high efficiency potential, light-absorbing properties, and suitability for large-scale production. Ongoing research focuses on improving its performance, stability, and cost-effectiveness for commercial solar cell applications.

C) The CZTS composite material

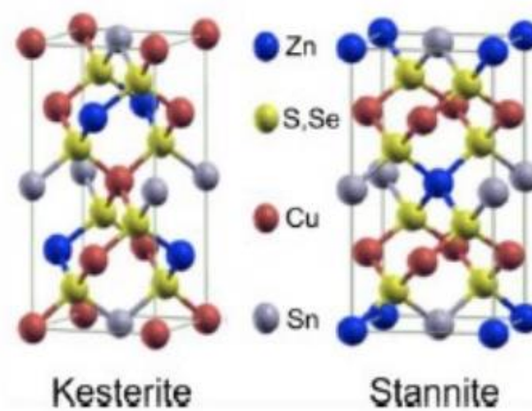

figure.3 crystalline structure of CZTS [3]

CZTS, or Copper Zinc Tin Sulfide, is a compound semiconductor material that has gained significant attention for its potential applications in thin-film solar cells. Here are some of the key structural properties of CZTS:

1. Crystal Structure: CZTS has a kesterite crystal structure, which belongs to the tetragonal crystal system. The lattice parameters vary depending on the composition and synthesis conditions.
2. Composition: CZTS is composed of copper (Cu), zinc (Zn), tin (Sn), and sulfur (S) elements. The typical stoichiometry is $Cu2ZnSnS4$, where the ratio of Cu, Zn, Sn, and S is 2:1:1:4, respectively. However, slight compositional variations are common.
3. Band Gap: CZTS is considered a direct bandgap semiconductor material, with its bandgap energy typically ranging from 1.0 to 1.5 eV. The bandgap can be tuned by adjusting the composition or by doping with other elements.

4. Electrical Conductivity: CZTS is a p-type semiconductor, meaning it has a predominance of positively charged holes as charge carriers. The electrical conductivity of CZTS is influenced by its composition, crystal structure, and defect states.
5. Optical Properties: CZTS exhibits interesting optical properties, including high absorption coefficients in the visible and near-infrared regions of the electromagnetic spectrum. This makes CZTS a potential candidate for photovoltaic applications.
6. Defects and Dopants: CZTS crystals can contain various defects and impurities, which can affect the material's properties. Doping with elements like sodium (Na) or indium (In) can improve the carrier concentration and overall device performance.
7. Thin Film Deposition: CZTS can be synthesized as a thin film through various techniques, such as sputtering, electrodeposition, or solution-based methods. Controlling the film growth and composition is crucial for achieving high-quality CZTS films.

It's worth noting that CZTS is an active area of research, and ongoing studies aim to improve its efficiency, stability, and scalability for solar cell applications.

[1] A. Gibaud and G. Vignaud, Specular reflectivity from smooth and rough surfaces, vol. 770, no. November. 2009. doi: 10.1007/978-3-540-88588-7_3.

[2] C. Roger, D. De, and D. Cigs, “CIGS sur substrats métalliques . To cite this version : HAL Id : tel-00965592 Développement de cellules photovoltaïques à base de CIGS sur substrats métalliques,” 2014.

[3] R. Fillon, “Etude des propriétés électroniques de couches minces de CZTSSe,” p. 134, 2017, [Online]. Available: https://tel.archives-ouvertes.fr/tel-01563500

Abstract: the magnetron sputtering method is a physical vapor deposition (PVD) method that uses low pressure plasmas and is currently widely employed in industry for the synthesis of thin films in fields of application like mechanics, optics, electronics, data storage, or even decorating. This technique involves creating a thin layer or film on the material surface, known as the "substrate," in order to give it the properties of the sputtered material.

In this thesis our work will focus on studying the factors that can impact the deposition process, based on the Monte Carlo simulation, we will use the SRIM model to calculate the sputtering yield of the metals and semiconductors used as the target material, considering the Argon as bombardment gas, we deduce firstly the best sputtering yield possible in order to identify the maximum bombardment energy and angle of incident which will help us to obtain the highest number of atoms ejected from each material used, then the sputtered atoms transport into the substrate will be calculated by using the second model SIMTRA, during the transport of these species, a variation in temperature (100, 300 and 600K) and pressure (0.5, 2 and 5Pa) is applied ,finally we will analyze the deposition of the atoms ejected by a target-substrate distance variation, the ultimate goal is to understand the effect of those parameters on the deposition of thin films and to deduce the finest adjustment for the magnetron sputtering that we should apply to acquire a maximum number of atoms arrived on the substrate.

Keywords: magnetron sputtering, physical vapor deposition, thin films, sputtered material, Monte Carlo simulation, sputtering yield, sputtered atoms transport

الخلاصة: طريقة الاخرق المغنطرون هي طريقة ترسيب بخار فيزيائي تستخدم بلازما الضغط المنخفض وتستخدم حاليا على نطاق واسع في الصناعة لتوليف الأغشية الرقيقة في مجالات التطبيق مثل الميكانيكا والبصريات والإلكترونيات وتخزين البيانات أو حتى الديكور. تتضمن هذه التقنية إنشاء طبقة رقيقة أو فيلم على سطح المادة ، والمعروفة باسم "الركيزة" ، من أجل إعطائها خصائص المادة المتناثرة.

في هذه الأطروحة ، سيركز عملنا على دراسة العوامل التي يمكن أن تؤثر على عملية الترسيب ، بناء على محاكاة مونت كارلو ، سنستخدم النموذج الأول لحساب عائد الاخرق للمعادن وأشباه الموصلات المستخدمة كمادة مستهدفة ، مع اعتبار الأرجون كغاز قصف ، نستنتج أولا أفضل عائد ممكن من الاخرق من أجل تحديد أقصى طاقة قصف وزاوية السقوط التي تساعدنا على الحصول على أكبر عدد من الذرات المقذوفة من كل مادة مستخدمة, ثم يتم حساب نقل الذرات المتناثرة إلى الركيزة باستخدام النموذج الثاني ، أثناء نقل هذه الأنواع ، يتم تطبيق اختلاف في درجة الحرارة (100 و 300 و 600 كلفن) والضغط (0.5 و 2 و 5 باسكال) ، وأخيرا سنقوم بتحليل ترسب الذرات المقذوفة بواسطة اختلاف مسافة الركيزة المستهدفة ، والهدف النهائي هو فهم تأثير تلك المعاملات على ترسب الأغشية الرقيقة واستنتاج أفضل تعديل للاخرق المغنطرون الذي يجب أن نطبقه للحصول على أكبر عدد ممكن من الذرات التي وصلت إلى الركيزة.

الكلمات المفتاحية: الاخرق المغنطرون ، ترسيب البخار المادي ، الأغشية الرقيقة ، المواد الاخرقة ، محاكاة مونت كارلو ، عائد الاخرق ، نقل الذرات الاخرقة

Résumé : La méthode de pulvérisation magnétron est une méthode de dépôt physique en phase vapeur (PVD) qui utilise des plasmas à basse pression et qui est actuellement largement employée dans l'industrie pour la synthèse de films minces dans des domaines d'application comme la mécanique, l'optique, l'électronique, le stockage de données, ou encore la décoration. Cette technique consiste à créer une couche ou un film mince à la surface d'un matériau, appelé " substrat ", afin de lui conférer les propriétés du matériau pulvérisé.

Dans cette thèse, notre travail se concentrera sur l'étude des facteurs qui peuvent avoir un impact sur le processus de dépôt. Basé sur la simulation de Monte Carlo, nous utiliserons le modèle SRIM pour calculer le rendement de pulvérisation des métaux et semi-conducteurs utilisés comme matériau cible, en considérant l'Argon comme gaz de bombardement, nous déduisons d'abord le meilleur rendement de pulvérisation possible afin d'identifier l'énergie maximale de bombardement et l'angle d'incidence qui nous aideront à obtenir le plus grand nombre d'atomes éjectés de chaque matériau utilisé, ensuite le transport des atomes pulvérisés dans le substrat sera calculé en utilisant le deuxième modèle SIMTRA, pendant le transport de ces espèces, une variation de la température (100, 300 et 600K) et de la pression (0. 5, 2 et 5Pa) est appliquée, enfin nous analyserons le dépôt des atomes éjectés par une variation de la distance cible-substrat, le but ultime est de comprendre l'effet de ces paramètres sur le dépôt de films minces et d'en déduire le réglage le plus fin de la pulvérisation magnétron que nous devrions appliquer pour acquérir un maximum d'atomes arrivés sur le substrat.

Mots clés : pulvérisation magnétron, dépôt physique en phase vapeur, films minces, matériau pulvérisé, simulation de Monte Carlo, rendement de pulvérisation, transport des atomes pulvérisés.